Theses and Dissertations

August 2017

Investigation of Catalytic Oxidation and Coupling Reactions on Gold, Palladium, and Gold-palladium Alloys

Theodore Douglas Thuening
University of Wisconsin-Milwaukee

INVESTIGATION OF CATALYTIC OXIDATION AND

COUPLING REACTIONS ON GOLD, PALLADIUM, AND

GOLD-PALLADIUM ALLOYS

by

Theodore Thuening

A Dissertation Submitted in

Partial Fulfillment of the

Requirements for the Degree of

Doctor of Philosophy

in Chemistry

at

The University of Wisconsin-Milwaukee

August 2017

ABSTRACT

INVESTIGATION OF CATALYTIC OXIDATION AND COUPLING REACTIONS ON GOLD, PALLADIUM, AND GOLD-PALLADIUM ALLOYS

by

Theodore Thuening

The University of Wisconsin-Milwaukee, 2017
Under the Supervision of Professor W. T. Tysoe

Polyvinyl acetate is a common adhesive and additive to emulsion-based paints produced in the millions of tons per year through the palladium catalyzed coupling of ethylene and acetic acid. Understanding the reaction mechanism and kinetics is integral to designing a more efficient catalyst through an increase in activity, selectivity, or both. It has been shown that selectivity for the vinyl acetate monomer (VAM) reaction increases to ~94% upon alloying palladium with gold compared to palladium alone (~80% selective).

The characterization of the VAM formation reaction on Pd(111) and Au/Pd(111) single crystal alloys has been extensively studied, but it has been shown that Pd(100) and particularly Au/Pd(100) alloys have an increased activity to Pd(111) and Au/Pd(111) catalysts. Competing reaction mechanisms have also been proposed for Pd(100) catalysts for the coupling of ethylene and acetic acid. To investigate the increased reaction rate on these surfaces and to elucidate the reaction pathway the behavior of the reactants, a detailed reaction mechanism, and the kinetics of the VAM formation reaction on Pd(100) and Au/Pd(100) alloys are presented here.

Another relevant catalytic process is the oxidation of carbon monoxide on gold (typically studied on supported gold nanoparticles). This reaction is of interest as CO is a common catalyst poison that binds strongly to many reactive transition metal catalysts. It is shown that by using ozone as an atomic oxygen source, CO oxidation occurs even on Au(111) single crystals. Two CO adsorption sites are observed after ozone exposure with CO oxidation occurring at as low as ~140 K.

The Au/Pd(100) alloy catalysts were also studied for their hydrogen adsorption behavior in an attempt to reconcile differences in previous work on hydrogen adsorption on Au/Pd alloys. Hydrogen is found to adsorb in two subsurface states as well as surface chemisorbed states, that, when further exposed to CO, become trapped in the subsurface of the alloy to elevated temperatures because of CO adsorption/blocking of palladium surface sites. Upon CO desorption, hydrogen desorption occurs through now-vacant palladium surface sites.

TABLE OF CONTENTS

vi

LIST OF FIGURES

xii

xiv

xvi

ACKNOWLEDGMENTS

I would first like to thank my advisor, Dr. W. T. Tysoe for his guidance and instruction during my tenure in his research group. Whether experiments were going well or poorly his constant push for the "next" experiment always kept me hopeful and focused on the work ahead.

Thank you to my committee members Dr. Dennis Bennett, Dr. Carol Hirschmugl, Dr. Jorg Woehl, and Dr. Alan Schwabacher for their guidance, and expertise. Every committee meeting resulted in fruitful discussions about my projects with actionable advice for me to take back into the lab.

Next I would like to thank my wife, Krista, for the love, support, and positive attitude she always has to spare, even throughout her own graduate education stresses. Her ability to help me put aside work and relax from time to time has been integral to my success in the lab.

I want to thank my family for their support through my academic career as well. I am appreciative of the push I received from my parents in my early education that fostered a work ethic and desire to excel that I continue to benefit from.

Finally, thank you to all of my current and former coworkers in the Tysoe group for your instruction and collaboration. The attitude of commiseration, support, and a willingness to lend a hand is key to being successful working in ultrahigh vacuum.

Chapter 1

Introduction

1.1 Background

The history of heterogeneous catalysis dates back around two centuries to Sir Humphrey Davy discovering that methane oxidation was catalyzed by platinum, but at that time the effect of the catalyst was not well understood. Since that discovery, numerous scientists have contributed to the understanding of heterogeneous catalysis such as Berzelius defining catalysis in 1836, Langmuir formulating a theory on surface adsorption of molecules in 1915, and Langmuir and Hinschelwood outlining the kinetics of reactions occurring on a surface. Heterogeneous catalytic reactions have been discovered, for example catalysts that facilitate the fixation of nitrogen to form ammonia (the Haber process), the conversion of carbon monoxide and hydrogen to hydrocarbons (the Fischer-Tropsch process), petroleum cracking, and the conversion of carbon monoxide in automobile exhaust. Along with these widely known processes, work continues to discover the next ground-breaking catalytic reaction as well as refining existing catalytic reactions to improve overall yield.

A recent significant discovery for the field of heterogeneous catalysis was the use of gold as an efficient catalyst, particularly in the form of nanoparticles on an oxide support initiated by Haruta [1-4]. Gold in the bulk is unreactive, leading to its use in jewelry as it does not oxidize. The discovery of its use as a nanoscale catalyst opened up a new class of catalysts to explore that

1

tend to show high selectivity. Among the reactions that gold has been found to effectively catalyze [5-8], carbon monoxide oxidation has been one of the most widely studied. CO is a poison for typical catalytic metals because it binds strongly to surface sites, and can be hard to displace or oxidize. As a consequence, it tends to poison the catalysts used in hydrogen fuel cells. Gold has been found to oxidize CO under mild conditions [1] leading to an interest in gold as a purification catalyst for CO specifically in hydrogen streams where carbon monoxide is a common impurity. Gold single crystal surfaces have been observed to restructure after adsorption of certain molecules providing active sites, similar to nanoparticle gold, that are then available for adsorption and reaction.

Another significant advance in heterogeneous catalysis was the discovery of the effects of alloying metals to form new materials with unique catalytic properties. Although alloy catalysts have been employed for some time, a rigorous understanding of the effects that control their activity and selectivity were not well understood until work beginning in the 1970s [9-11]. Two main effects have been found to control selectivity and activity of alloy catalysts: the ensemble and electronic (ligand) effects [12, 13].

The ensemble effect refers to the distribution of the bimetallic atoms and their spacing on the alloy surface. Alloying with gold often results in primarily ensemble effects, where the more catalytically active metal (Pt, Pd, etc.) are essentially "capped", or the surface concentration of ensembles is reduced by alloying to reduce the concentration of contiguous active metal sites. This effect can significantly reduce the frequency of undesirable side/decomposition reactions that can compete with the desired reaction. Some alloys, such as the Au/Pd(100) alloys show a long-range ordering of metal atoms dispersed on the surface leading to very reproducible, ordered alloys that allow for a detailed knowledge of available active sites as a function of the

2

surface coverages of each metal [14]. Other surfaces, such as Au/Pd(111), have been found to have a more random distribution with weak long-range ordering effects, and, as such, have a larger distribution in the size of ensembles on the surface at various coverages [15].

Alloying two metals can also locally change the electronic structure. This effect can occur due to charge transfer from one metal to another in the surface, changing the overall properties of the catalytic system. For vinyl acetate synthesis on Au/Pd(111) alloys, a combined effect of increased activity and selectivity were observed from both ensemble and electronic effects.

Recently, there has been a focus on alloys with very low concentrations (<5% coverage) of active metals have been studied for their ability to perform highly selective hydrogenation reactions [16, 17]. These so-called "single atom" alloys (SAAs) have also been observed to be resistant to CO poisoning [18], a problem that can plague catalysts with very few active sites.

1.2 Vinyl Acetate Monomer Synthesis

The production of vinyl acetate (as polyvinyl acetate) is an important industrial reaction where synthesis in the millions of tons a year is common for the use in adhesives and paints. The reaction to form the vinyl acetate monomer (VAM) consists of the coupling between ethylene and acetate species on a palladium catalyst in the presence of oxygen with a typical reaction selectivity of ~80%. On alloying with gold, the selectivity can reach ~94% [19-21]. VAM formation was previously shown to proceed via the so-called Samanos pathway where ethylene couples to surface bound acetate species via the O-Pd bond, forming an acetoxyethyl intermediate, and subsequently undergoes a β-hydride elimination, forming VAM [22-24].

3

On Pd(111) and Pd(100) surfaces, under UHV conditions, vinyl acetate is found to decompose when dosed directly to the surface [25, 26]. In the case of the VAM formation reaction on Pd(111), ethylene was found to form ethylidyne species (CH_3-$C\equiv_{(ads)}$), an unreactive, strongly bound species, which accumulates on the surface, inhibiting the decomposition of any VAM that was formed [27]. Ethylidyne does not form on the Pd(100) surface due to the lack of three-fold hollow sites. When alloyed with gold, the Au/Pd(111) surface showed enhanced reaction rates for the formation of VAM where, when gold coverage increased, it was found that reactants bound more weakly, leading to a decrease in activation energies and an increase in reaction rate [28].

The Pd(100) and Au/Pd(100) surfaces have been studied for the VAM reaction under high-pressure conditions, where it was found that Au/Pd(100) showed a significant larger turn-over frequency (TOF) (reaction rate) than Au/Pd(111) alloys, with a sharp increase in reaction rate for alloys with a ~90% gold surface coverage; an active site containing two non-contiguous, suitably spaced palladium atoms was proposed to be the source of the enhanced activity [21, 29]. Along with the Samanos pathway, an alternative VAM formation pathway has been proposed in which ethylene dehydrogenates directly to form vinyl species and subsequently couples directly to the surface-bound acetate species to form VAM [30, 31].

To compliment previous work on Au/Pd(111) alloys, a comprehensive analysis of the behavior of adsorbed reactants and products as well as a characterization of the overall VAM reaction pathway is necessary on Pd(100) and Au/Pd(100) alloy surfaces under controlled conditions to elucidate the reaction mechanism and understand the enhanced reaction rates observed under catalytic conditions. This is addressed in the work presented here.

4

1.3 Overview of Present Work

Chapter 2 introduces the experimental methods and techniques employed to monitor the experiments described in subsequent chapters. A brief description of the equipment and analytical methods is provided.

Chapter 3 describes the investigation of oxygen adsorption on alloy surfaces using ozone, where through TPD, DFT, and Monte Carlo simulations, the analysis of oxygen adsorption sites is described.

Chapter 4 studies the adsorption of ethylene on Au/Pd(100) alloy surfaces where di-σ bound ethylene is observed that has a sharply increasing desorption activation energy with increasing palladium coverage from 0 to 0.4 ML.

Chapter 5 summarizes the characterization of the mechanism and kinetics of the VAM formation pathway on a Pd(100) surface. The results are compared and contrasted with results for the VAM formation reaction on Pd(111).

Chapter 6 describes the VAM formation pathway on Au/Pd(100) alloy surfaces, where the kinetics and mechanism can be described in the same fashion as the bare Pd(100) surface. Enhanced reaction rates are observed with increasing gold coverage to 0.5 ML with an abrupt lack of reaction at higher gold coverages.

Chapter 7 shows results for the oxidation of carbon monoxide on a gold single crystal using ozone as an atomic oxygen source. Ozone dosing is found to create another distinct CO adsorption site. Stoichiometric oxidation of CO and oxygen is observed.

Chapter 8 highlights recent work exploring hydrogen adsorption (and absorption) on Au/Pd(100) alloys with the goal of rectifying differences in published hydrogen adsorption

effects. Carbon monoxide doses are shown to "cap" hydrogen contained in the subsurface region to elevated temperatures.

Chapter 9 summarizes the previous individual chapters in a cohesive discussion of the VAM formation reaction and other interesting reactions on gold, palladium, and gold-palladium alloys.

1.4 References

[1] M. Haruta, T. Kobayashi, H. Sano, N. Yamada, Novel Gold Catalysts for the Oxidation of Carbon Monoxide at a temperature far below 0 C, Chem. Lett., 16 (1987) 405-408.

[2] M. Haruta, N. Yamada, T. Kobayashi, S. Iijima, Gold catalysts prepared by coprecipitation for low-temperature oxidation of hydrogen and of carbon monoxide, Journal of Catalysis, 115 (1989) 301-309.

[3] M. Date, M. Okumura, S. Tsubota, M. Haruta, Vital role of moisture in the catalytic activity of supported gold nanoparticles, Angewandte Chemie-International Edition, 43 (2004) 2129-2132.

[4] M. Haruta, Size- and support-dependency in the catalysis of gold, Catalysis Today, 36 (1997) 153-166.

[5] T. Hayashi, K. Tanaka, M. Haruta, Sleective Vapor-Phase Epoxidation of Propylene over Au/TiO2 Catalysts in the Presence of Oxygen and Hydrogen, Journal of Catalysis, 178 (1998) 566-575.

[6] D. Andreeva, V. Idakiev, T. Tabakova, A. Andreev, R. Giovanoli, Low-temperature water gas-shift reaction on Au-Fe2O3 catalyst, Applied Catalysis A: General, 134 (1996) 275-283.

[7] A. Ueda, M. Haruta, Nitric Oxide Reduction with Hydrogen, Carbon Monoxide, and Hydrocarbons over Gold Catalysts, Gold Bulletin, 32 (1999) 3-11.

[8] G.C. Bond, P.A. Sermon, G. Webb, D.A. Buchanan, P.B. Wells, Hydrogenation over supported gold catalysts, J. Chem. Soc., Chem. Commun., 334 (1973) 444-445.

[9] J.H. Sinfelt, Catalysis by Alloys and Bimetallic Clusters, Acc. Chem. Res., 10 (1977) 15-20.

[10] J.H. Sinfelt, J.L. Carter, D.J.C. Yates, Catalytic hydrogenolysis and dehydrogenation over copper-nickel alloys, Journal of Catalysis, 24 (1972) 283-296.

[11] J.H. Sinfelt, Supported "bimetallic cluster" catalysts, Journal of Catalysis, 29 (1973) 308-315.

[12] V. Ponec, Alloy catalysts: the concepts, Applied Catalysis A: General, 222 (2001) 31-45.

[13] J.H. Sinfelt, Bimetallic Catalysts, Academic Press, Inc., New York, 1983.

[14] M. Garvey, J.A. Boscoboinik, L. Burkholder, J. Walker, C. Plaisance, M. Neurock, W.T. Tysoe, Structure of the Au/Pd(100) Alloy Surface, The Journal of Physical Chemistry C, 116 (2012) 4692-4697.

[15] J.A. Boscoboinik, C. Plaisance, M. Neurock, W.T. Tysoe, Monte Carlo and density functional theory analysis of the distribution of gold and palladium atoms on Au/Pd(111) alloys, Phys. Rev. B, 77 (2008) 714-722.

[16] G. Kyriakou, M.B. Boucher, A.D. Jewell, E.A. Lewis, T.J. Lawton, A.E. Baber, H.L. Tierney, M. Flytzani-Stephanopoulos, E.C.H. Sykes, Isolated Metal Atom Geometries as a Strategy for Selective Heterogeneous Hydrogenations, Science, 335 (2012) 1209-1212.

[17] F.R. Lucci, M.T. Darby, M.F.G. Mattera, C.J. Ivimey, A.J. Therrien, A. Michaelides, M. Stamatakis, E.C.H. Sykes, Controlling Hydrogen Activation, Spillover, and Desorption with Pd-Au Single-Atom Alloys, J. phys. Chem. Lett., 7 (2016) 480-485.

7

[18] J. Liu, F.R. Lucci, M. Yang, S. Lee, M.D. Marcinkowski, A.J. Therrien, C.T. Williams, E.C.H. Sykes, M. Flytzani-Stephanopoulos, Tackling CO Poisoning with Single-Atom Alloy Catalysts, Journal of the American Chemical Society, 138 (2016) 6396-6399.

[19] P.M. Colling, L.R. Johnson, I. Nicolau, Palladium-gold catalyst for vinyl acetate production, in: U.S.P. Office (Ed.), Hoechst Celanese Corporation, United States, 1996.

[20] L. Horning, F. Wunder, T. Quadflieg, Process for Preparing Vinyl Acetates, in: F.H.A.V.M.L. Bruning (Ed.), United States, 1967.

[21] M.S. Chen, D. Kumar, C.W. Yi, D.W. Goodman, The promotional effect of gold in catalysis by palladium-gold, Science, 310 (2005) 291-293.

[22] D.J. Stacchiola, F.C. Calaza, L. Burkholder, W.T. Tysoe, Vinyl acetate formation by the reaction of ethylene with acetate species on oxygen-covered Pd(111), Journal of the American Chemical Society, 126 (2004) 15384-15385.

[23] B. Samanos, P. Boutry, R. Montarnal, The mechanism of vinyl acetate formation by gas-phase catalytic ethylene acetoxidation, Journal of Catalysis, 23 (1971) 19-30.

[24] D. Stacchiola, F. Calaza, L. Burkholder, A.W. Schwabacher, M. Neurock, W.T. Tysoe, Elucidation of the Reaction Mechanism for the Palladium-Catalyzed Synthesis of Vinyl Acetate, Angewandte Chemie International Edition, 44 (2005) 4572-4574.

[25] F. Calaza, D. Stacchiola, M. Neurock, W.T. Tysoe, Structure and decomposition pathways of vinyl acetate on Pd(111), Surface Science, 598 (2005) 263-275.

[26] Z. Li, F. Calaza, C. Plaisance, M. Neurock, W.T. Tysoe, Structure and Decomposition Pathways of Vinyl Acetate on Clean and Oxygen-Covered Pd(100), The Journal of Physical Chemistry C, 113 (2009) 971-978.

8

[27] D.J. Stacchiola, W.T. Tysoe, The Kinetics of Ethylidyne Formation from Ethylene on Pd(111), J. Phys. Chem. C, 113 (2009) 8000-8001.

[28] F. Calaza, Z. Li, M. Garvey, M. Neurock, W. Tysoe, Reactivity and Selectivity in the Au/Pd(111) Alloy-Catalyzed Vinyl Acetate Synthesis, Catal Lett, 143 (2013) 756-762.

[29] M.S. Chen, K. Luo, T. Wei, Z. Yan, D. Kumar, C.W. Yi, D.W. Goodman, The nature of the active site for vinyl acetate synthesis over Pd-Au, Catalysis Today, 117 (2006) 37-45.

[30] I.I. Moiseev, M.N. Vargaftik, Perspectives in Catalysis, Chemistry for the 21st Century, Blackwell Scientific Oxford, 1992.

[31] I.I. Moiseev, M.N. Vargaftik, Izr. Akad. Nauk. SSSR, Engl. Transl., 133 (1960).

Chapter 2

Experimental Methods and Techniques

2.1 Ultrahigh Vacuum

Maintaining a clean environment when performing surface chemical reactions is crucial. Surface contamination can interfere with reactant binding, reaction progression, and interfere with precise knowledge of the reactant environment. To limit contamination of model catalyst surfaces the use of ultrahigh vacuum (UHV) chambers is common in the field of surface chemistry. Using a variety of vacuum pumps described in detail below, background pressure in a reaction chamber can be attained as low as 10^{-11} Torr, with pressures of 10^{-10} Torr also acceptable. To demonstrate why pressures on this order are needed consider the Hertz-Knudsen equation for Langmuirian adsorption[1]:

$$F = \frac{P}{\sqrt{2\pi m k_B T}} \tag{2.1}$$

where F is incident flux (molecules·m^{-2}·s^{-1}), P is pressure (Pa), m is the mass of the particle of gas (kg), k_B is the Boltzman constant (m^2·kg·s^{-2}·K^{-1}), and T is temperature (K). Assuming a sticking probability of unity, for a gas of molecular weight 28 g/mole, at a temperature of 300 K, and a surface comprising of ~10^{19} atoms per m^2, it is found that one monolayer of molecules adsorb within 1s at a pressure of 10^{-6} torr. Where pressure has been converted to Torr as it is a more widely used unit in the United States than Pascals (Pa).

This calculation emphasizes why UHV conditions are necessary to maintain pristine surfaces. With a base pressure of 10^{-10} Torr, a monolayer of contamination will take 10^4 seconds to accumulate, thereby providing an adequate window during which to perform experiments and assume cleanly conditions.

The unit the Langmuir (L) was introduced corresponding to an exposure (in pressure for a unit time period) where 1 L is defined as being equal to a 10^{-6} Torr exposure of a gas for 1 s. This convenient unit is the most common for describing gas exposure to surfaces in surface science since a 1 L exposure leads to approximately 1 ML of adsorbate on a typical surface when the sticking probability is unity, and as such is used throughout this work.

2.2 UHV Chambers

To maintain UHV conditions stainless-steel reaction chambers are the most commonly used reaction vessels for surface science experiments. One chamber can be equipped with a number of instruments for characterization of the surface and reaction monitoring, as well as the
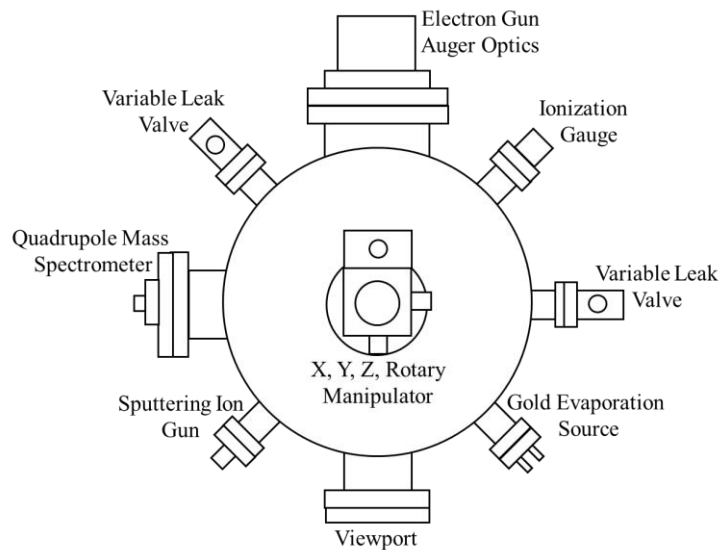
Figure 2.2.1 Top view of a typical TPD UHV chamber

11

pumps necessary to maintain vacuum through the use of conflat flange ports using copper gaskets to seal them. An example of a typical temperature programmed desorption (TPD), UHV chamber is shown in Figs. 2.2.1 and 2.2.2.

To achieve base pressures in the UHV region, it is necessary to bake the chamber at ~140 °C while pumping to accelerate the removal of contaminants, primarily water vapor from the external walls of the chamber, after exposure to atmospheric pressures. Once a suitable base pressure has been achieved in this way, minimal additional effort is required to maintain it.
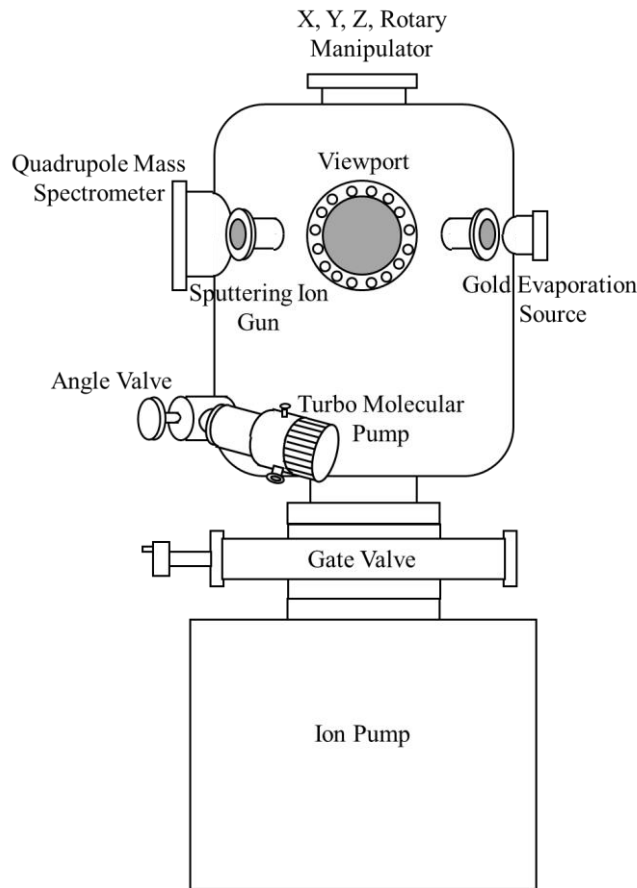
Figure 2.2.2 Front view of a typical TPD UHV chamber

2.3 Vacuum Pumps

Several different styles of pumps are utilized in tandem to achieve and maintain a base pressure in the UHV region, and will be discussed below.

2.3.1 Mechanical Pumps

Mechanical pumps, rough pumps, or rotary pumps provide an initial, low vacuum as they are utilized from atmospheric pressure to $\sim 10^{-3}$ Torr. Fig. 2.3.1 displays the design of a typical rotary pump, where the basic function involves the vanes, mounted on a spring rod, sealing against the stator, as the rotor spins. This compresses the inlet gas above atmospheric pressure, and allows expulsion once a vane rotates past the exhaust outlet. The specific model used in this work, a Welch model 1400 rotary pump, consists of two sets of rotors and vanes comprising "low pressure" and "high pressure" stages to the pump allowing for better vacuum to be achieved. This model of pump also contains a ballast. The ballast is an improvement over basic
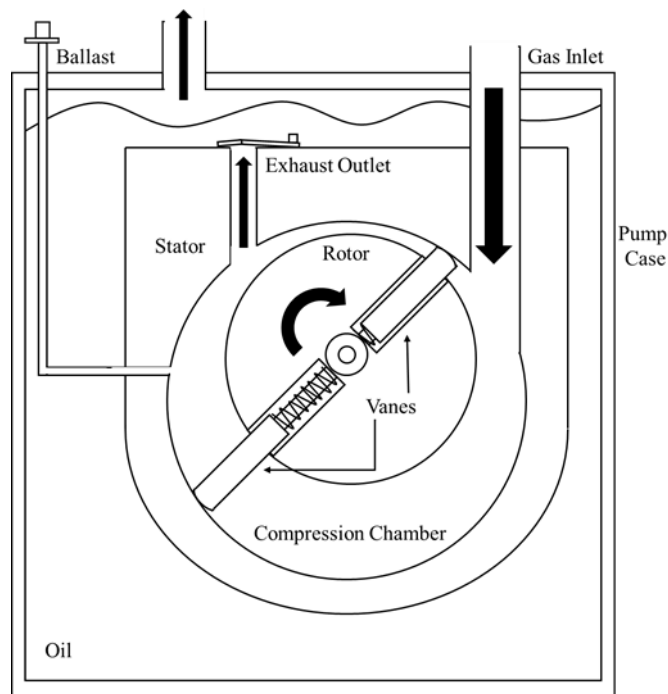
Figure 2.3.1.1 Schematic diagram of a rotary pump

13

rotary pumps that allows the direct addition of air into the compression chamber. This results in a lower compression, and ultimately less vapor being condensed into the oil.

2.3.2 Turbomolecular Pumps

The turbomolecular pump operates by transfer of momentum as gas molecules collide with turbine blade stages. These stages are comprised of a rotor moving at high speeds (krpm range) and a corresponding stator. The rotor blades are angled such that upon collision with the blade surface, gas molecules are directed and compressed to the lower levels and stages of the pump.   A mechanical pump is need to remove compressed gases at the outlet of the turbomolecular pump. Typical maximum pressures achieved by the turbomolecular pumps used (Varian V70) are in the 10^{-8} Torr range.
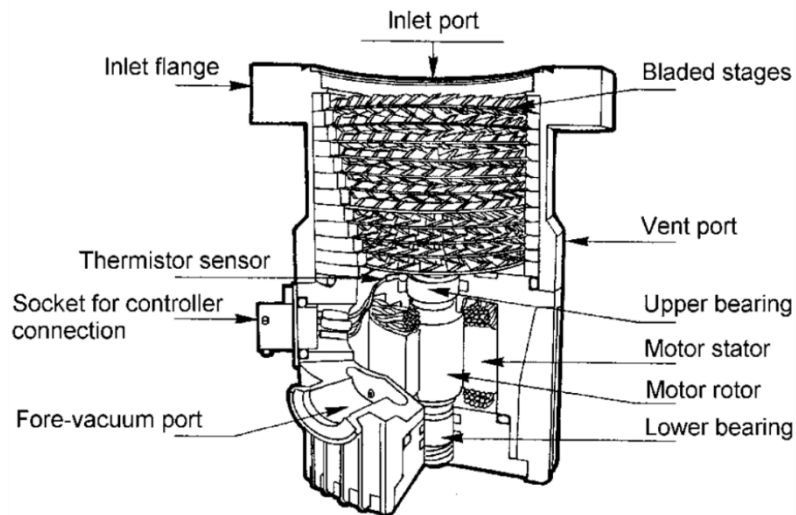
Figure 2.3.2.1 Schematic diagram of a turbomolecular pump

14

2.3.3 Diffusion Pumps

Diffusion pumps work on through the creation of differential pressure. Silicone-based oil is heated at the base of the pump its boiling point. The oil vapor is directed through one of three stages where it is compressed at the top of each stage. This compression causes high speed expulsion of the oil vapor through jet ports, trapping gas molecules as the vapor condenses on the walls and recollects at the base. Through this method UHV conditions (down to 10^{-11} Torr) can be obtained at the top of the pump, while a higher pressure build-up occurs at the base. As there are no moving parts to a diffusion pump, it must be used in tandem with a mechanical backing pump to remove condensed gases through the foreline exhaust. The base pressure achieved can be lowered through the use of a liquid-nitrogen trap, which can collect gas
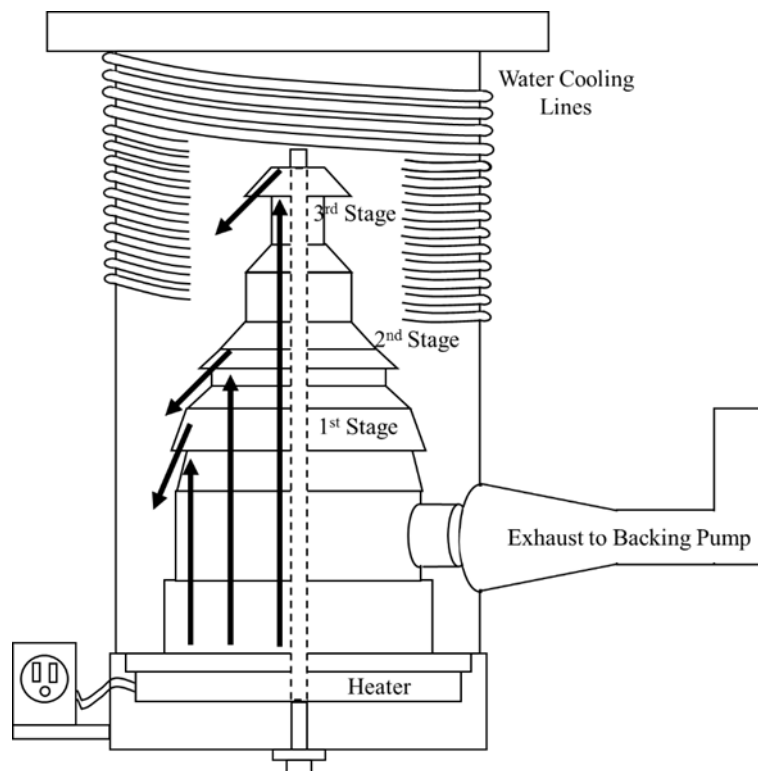
Figure 2.3.3.1 Schematic diagram of a diffusion pump

15

molecules as well as prevent oil backstreaming, a relevant issue with diffusion pumps. The main benefit of diffusion pumps is their high pumping speeds, which is critical when working with high gas loads and specifically with gases not pumped easily by other pumping methods, such as argon. The specific diffusion pumps used in this work are Varian M6, Varian HSA, and Varian HS2 models.

2.3.4 Ion Pumps

Ion pumps differ from the pumps previously discussed because they do not create high- and low-pressure regions where the high-pressure region is expelled through an exhaust port from the vacuum chamber. Generally, in the case of ion pumps, gas molecules are ionized and
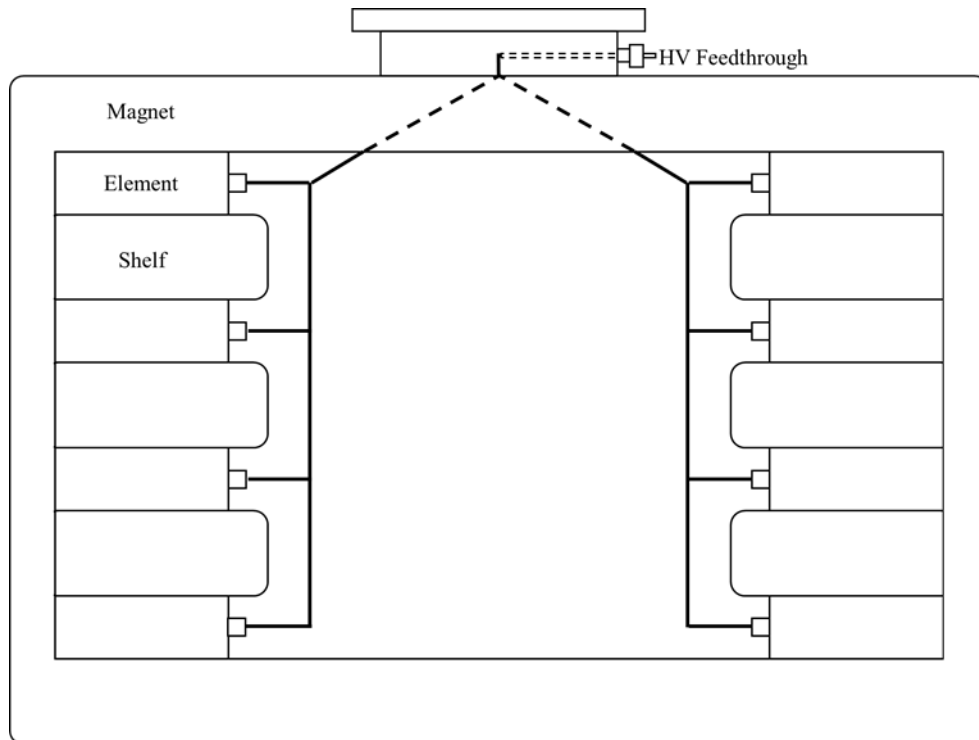
Figure 2.3.4.1 Schematic diagram of a typical ion pump

accelerated toward a cathode, and then embedded in the cathode, removing them from the gas phase, thereby lowering the pressure. To achieve this ion pumps employ high voltages (3-7 kV) to create a plasma discharge in the anode creating a Penning trap of electrons. This trap ionizes incoming gases and, in combination with external magnets, accelerates them toward the cathode where they can be embedded in the cathode, or sputter cathode material (titanium) onto the pump surfaces. This sputtered titanium is reactive, and will chemisorb or physisorb additional gases, thus removing them from the gas phase. This process is called gettering, and titanium is generally used as an effective getter for reactive gases.
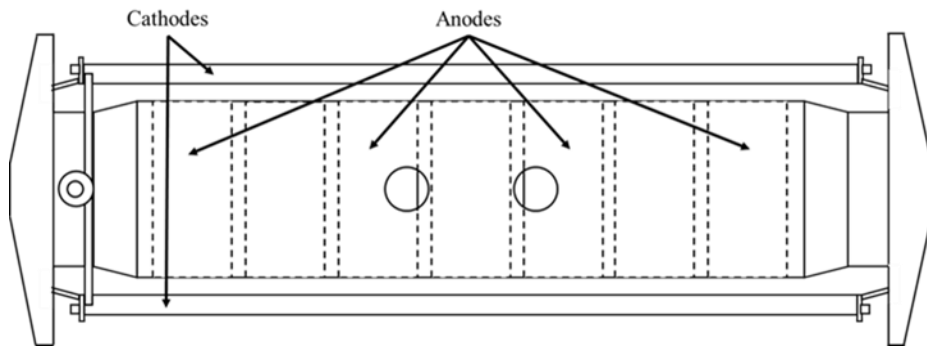
Figure 2.3.4.2 Schematic diagram of an ion pump element

2.4 Sample Manipulation and Preparation

2.4.1 Sample Manipulator

Sample motion, manipulation, heating and cooling, and temperature measurement within vacuum chambers is achieved through the use of X-Y-Z-θ-axis manipulators from Huntington Mechanical Labs equipped with multiple feedthrough ports and a rotary motion feedthrough. Sample movement of 2.5 cm are attained in both the x and y direction, and 5 cm in the z direction through the use of precision micrometer motion drives with full circular rotation about

17
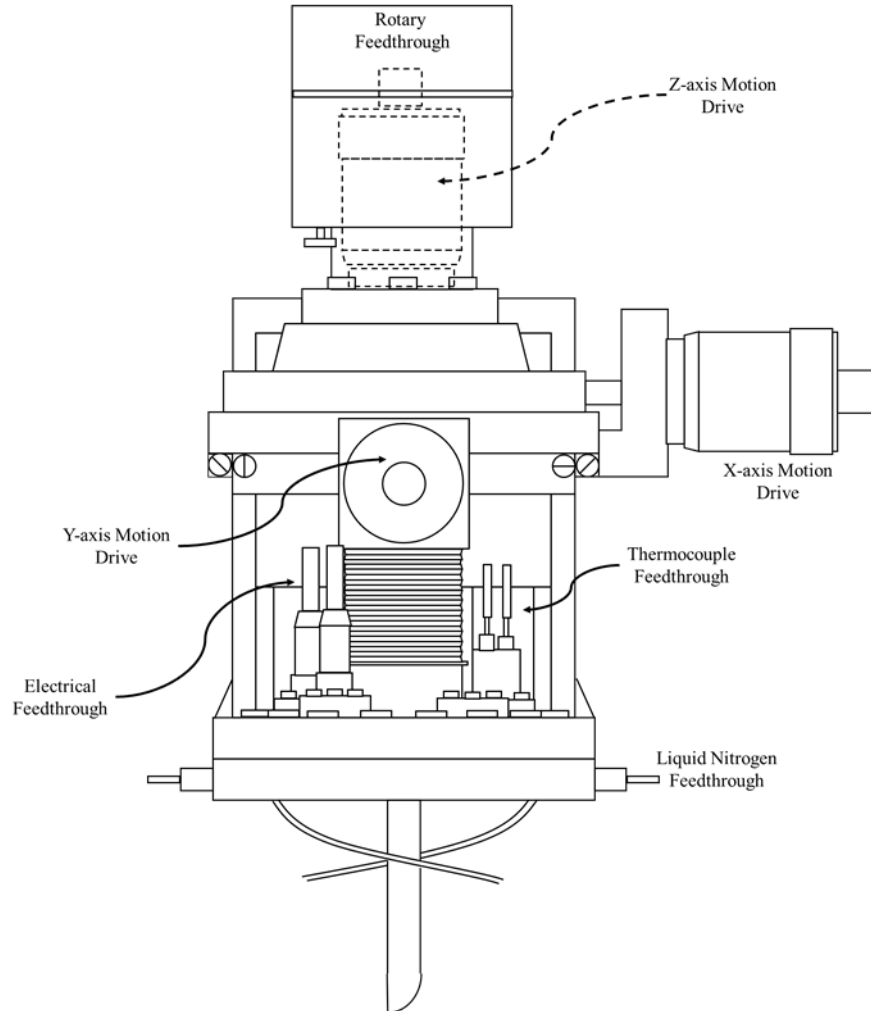
Figure 2.4.1.1 Schematic diagram of a typical sample manipulator

the z-axis. Through the use of current and liquid feedthroughs, the sample can be resistively heated to ~1200 K and cooled by contact with a liquid-nitrogen filled reservoir to ~90 K.

2.4.2 Mounting and Cleaning

A typical transition-metal single crystal mount is shown in Fig. 2.4.2.1. The single crystal in this work, either Pd(100) or Au(111), is attached via resistive spot-welding of tantalum wire and rods to the sample holder mounted on the manipulator, where the Pd crystal can be directly welded to the tantalum wire (typical energy of ~35 Ws), but the gold crystal is held in place by the tantalum wire through grooves in the edge of the crystal. A k-type thermocouple is

18

spot-welded (~5 Ws) directly to the palladium crystal, or to a tantalum wire in contact with the gold crystal.

The Pd(100) single crystal was consistently cleaned by Argon bombardment with a beam voltage of 2 keV and a sample current of 2-3 $\mu A/cm^2$ followed by annealing to ~1000 K in vacuo to reform a well-ordered (100) surface. This was followed by temperature cycling (~400 K-1000 K) of the sample in 5.0×10^{-8} Torr of oxygen. The cleanliness of the sample was monitored using Auger electron spectroscopy (AES) as well as with oxygen titrations monitoring oxygen and combustion products to judge the amount of carbon contaminating the surface as carbon and palladium have overlapping Auger peaks that preclude direct measurement of cleanliness with AES.
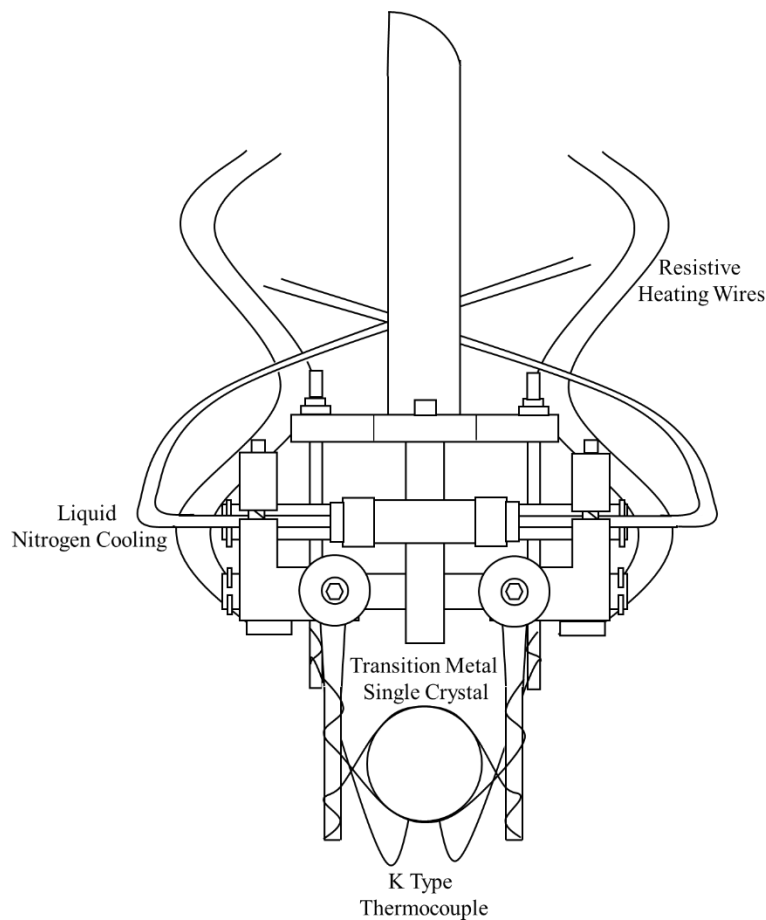
Figure 2.4.2.1 Schematic diagram of a single crystal sample mount

19

The Au(111) sample was cleaned using Argon ion bombardment with a beam voltage of ~0.5 keV and a sample current of ~1 $\mu A/cm^2$, and the sample cleanliness monitored by AES.

2.4.3 Alloy Preparation

Gold films were prepared by deposition of gold onto a Pd(100) single crystal surface from an evaporation source displayed in Fig. 2.4.3.1, originally designed by Lambert et al. [2]. Generally, gold is loaded into an alumina tube and the tube furnace is resistively heated until a flux of evaporated gold is achieved and directed via a stainless steel shroud. The amount of adsorbed gold is monitored by AES, with 5 ML of gold being a standard dose to create the alloy surfaces studied. Upon annealing of the 5 ML of gold on Pd(100), well-characterized alloy surfaces with gold surface coverages ranging from 1.0 to 0 ML can be reproducibly formed via a standard procedure developed previously [3, 4].
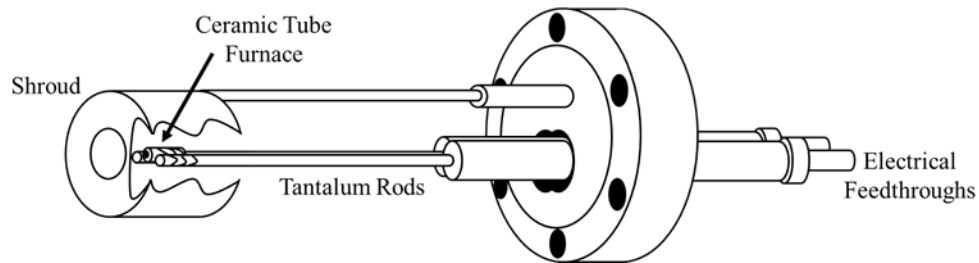
Figure 2.4.3.1 Schematic diagram of a gold dosing source

Gold films in this work were deposited with a power supply current of ~11.9 A and voltage of ~5 V for 20-30 minutes. The Pd(100) crystal was positioned directly in front of the stainless-steel shroud at a distance of 0.5-1 inch. For 5 ML of gold, the ratio of AES intensities for gold signature peak (69 eV) to the palladium signature peak (330 eV) was measured with a 7:1 ratio being indicative of 5 ML of gold [5]. Alloys compositions were confirmed by palladium ensemble probing by CO TPD and comparison to published spectra [3].

20

2.5 Ozone Generation and Dosing

For surfaces such as gold and high gold coverage Au/Pd alloys, where molecular oxygen does not dissociate, other methods must be used to obtain atomic oxygen on the surface. It has been shown previously [6] that ozone decomposes on gold surfaces to yield atomic oxygen on the surface and molecular oxygen.

Ozone dosing in this work was achieved by introduction of a mixture of O_3 and O_2, produced by an A2Z Ozone generator, through a self-designed flow, dosing source attached to a variable leak valve (Fig. 2.5.1). The ozone/O_2 mixture is piped directly to the leak valve via Teflon and glass tubing where the inner glass tube is directed at the inlet of the leak valve to minimize decomposition before admission to the UHV chamber. The outlet of the leak valve was fitted with a glass tube to direct the dosing to the surface of the crystal while minimizing
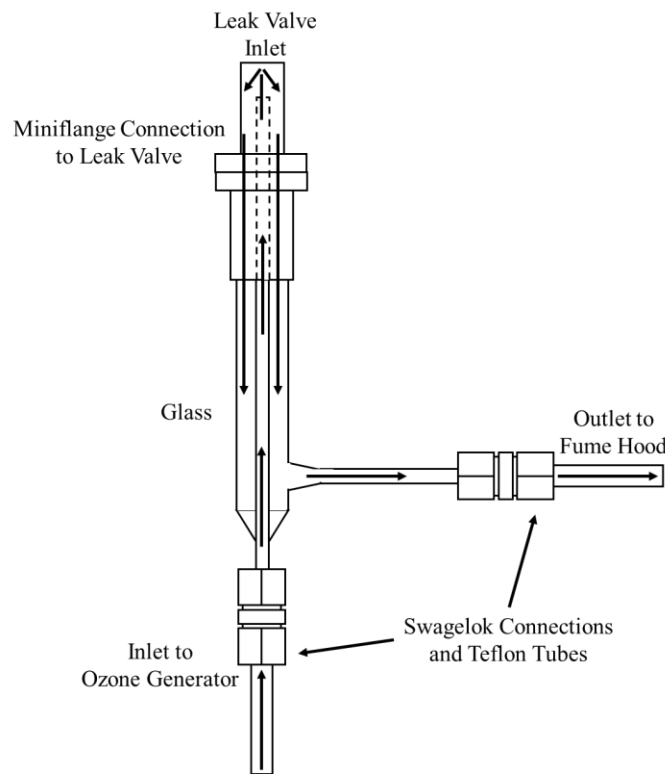
Figure 2.5.1: Schematic diagram of ozone dosing apparatus

21

decomposition. The concentration of ozone was calibrated by monitoring the 48 amu and 32 amu signals while dosing to the chamber. By this method it was found that the mixture contained ~5% O_3 and ~95% O_2. Ozone dosing in this work is work is referred to as the cumulative dose of O_3 and O_2.

2.6 Gas Manifold and Sample Purification

Gases are introduced into UHV chambers through the use of variable, precision leak valves. These leak valves are capable of introducing gases at a low pressures ($\sim 1 \times 10^{-10}$ Torr) into the chamber with atmospheric pressures at their inlet. Leak valves are connected to a gas manifold setup with multiple sample admission valves. The gas line is constructed from glass to reduce sample decomposition and the line pressure is measured by a manometer pressure gauge (see Fig. 2.6.1).

Before introduction to the UHV chamber, samples must be purified. Gases are typically purchased with high purities to limit purification needed. The manifold is flushed with the desired gas three times to ensure no contamination from any gas remaining in the line occurs. A flushing cycle consists of filling the manifold with the desired gas sample and pumping the contained volume away using the mechanical pump, and subsequently diffusion pumping.

Gases, and liquid samples with appreciable vapor pressures conducive to gas phase dosing can be further purified by the freeze-pump-thaw method where the sample is frozen with liquid nitrogen into a glass vial and the vial is pumped on to remove contaminants while allowing the sample to thaw. This technique is typically repeated over multiple cycles to remove the maximum amount of contaminants. Gas-phase samples are dosed to the UHV chamber and monitored for cleanliness using the quadrupole mass spectrometer.

22
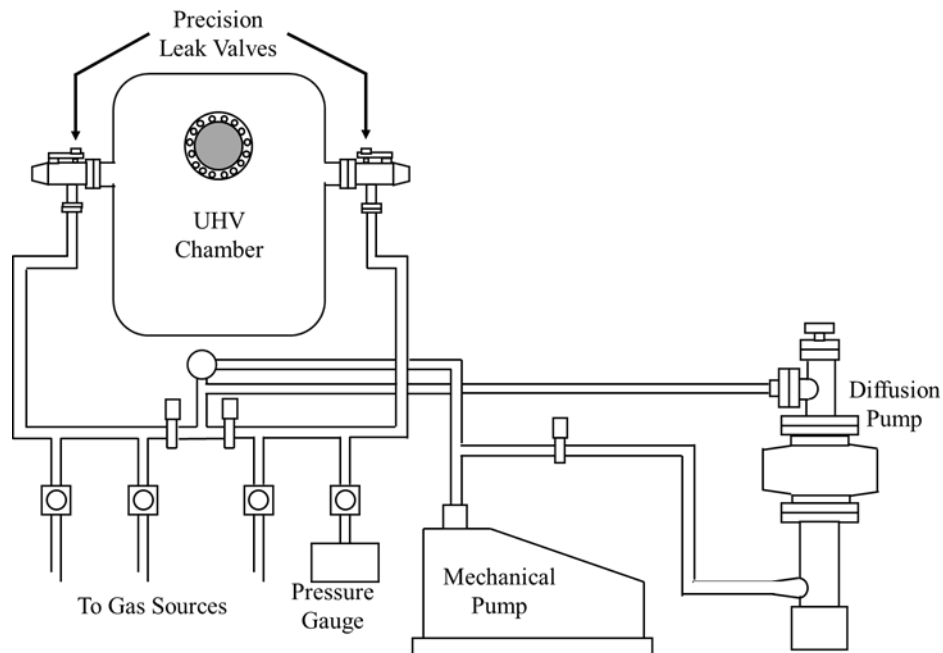
Figure 2.6.1 Schematic diagram of a typical gas manifold

2.7 Temperature Programmed Desorption (TPD)

Temperature programmed desorption (TPD) and temperature programmed reaction spectroscopy (TPRS) are powerful techniques that allow the kinetics of desorption and surface reaction events to be investigated. The difference between these techniques is subtle, and it is generally accepted that TPR spectroscopy involves surface reactions occurring during temperature ramping leading to reaction or decomposition products desorbing from the surface, while TPD involves desorption of adsorbates. In either case, compounds are dosed onto the surface of the single crystal via a variable leak valve, this sample is then heated while a mass spectrometer captures the evolution of species desorbing from the surface.

Desorption kinetics can be described using the Arrhenius equation:

$$R_{des} = -\frac{d\theta}{dt} = v \cdot \theta^x \cdot \exp\left(-\frac{E_{des}}{RT}\right) \tag{2.7.1}$$

23

where R_{des} is the rate of desorption, θ is the surface concentration (coverage) of adsorbed species, υ is the kinetic frequency factor that arises from transition-state theory [7], and will be described below, x is the kinetic order of desorption (typically 1 or 2), E_{des} is the activation energy for desorption, R is the universal gas constant: 8.314 J/mol·K, and T is absolute temperature. As the coverage of the desorbing species decreases, signal also decreases, resulting in a typical desorption shape shown in Fig. 2.7.1.
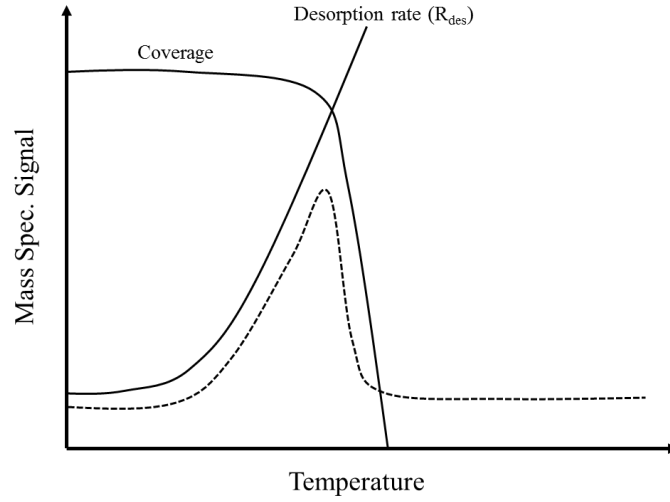
Figure 2.7.1 Typical desorption peak shape in TPD

Incorporating a linear heating rate, $\beta = dT/dt$, into equation 1 gives:

$$R_{des} = -\frac{d\theta}{dT} = \frac{\upsilon \cdot \theta^x}{\beta} \cdot \exp\left(-\frac{E_{des}}{RT}\right) \tag{2.7.2}$$

and considering that the temperature at the peak of the desorption profile corresponds to a change of 0 for the reaction rate as a function of temperature ($T=T_{max}$), i.e. the derivative of the desorption profile will be zero at the apex:

$$\left.\frac{dR_{des}}{dT}\right|_{T_{max}} = 0 = \left.\frac{d^2\theta}{d^2T}\right|_{T_{max}} = x \cdot \theta^{x-1} \cdot \frac{d\theta}{dT} + \theta^x \cdot \frac{E_{des}}{RT^2} \tag{2.7.3}$$

Substituting $\frac{d\theta}{dT}$ from 2 into 3 and solving for $\frac{E_{des}}{RT^2}$ gives

$$\frac{E_{des}}{RT^2} = \frac{1}{\beta} \cdot \upsilon \cdot x \cdot \theta^{x-1} \cdot \exp\left(-\frac{E_{des}}{RT_{max}}\right) \tag{2.7.4}$$

24

Thus it can be inferred that for first-order kinetics, where x=1, the rate of desorption increases linearly with surface coverage ((2.7.2)), and the peak temperature of the desorption profile is independent of the coverage of adsorbates ((2.7.4)). An approximation of equation (2.7.4) by Redhead [7] for first-order reactions provides an avenue to obtain a reasonable estimate of the activation energy for desorption as a function of the peak temperature of the desorption profile:

$$E_{des} = R \cdot T_{max} \cdot \left(\ln \left(\frac{\upsilon \cdot T_{max}}{\beta} \right) - 3.65 \right) \quad\quad\quad (2.7.5)$$

where the E_{des} was experimentally confirmed to linearly relate to T_{max} when the value of υ/β are between 10^{13} and 10^8, where $\upsilon/\beta = 10^{13}$ is typically used to provide an approximate E_{des}.

2.8 Reflection Absorption Infrared Spectroscopy (RAIRS)

Infrared spectroscopy is one of the most versatile spectroscopic techniques available for characterization of chemical samples. It allows for the probing of gases, liquids, solids, films, and, important to this work, surface samples. IR spectroscopy involves exposing a sample to infrared radiation, which, at certain energies will cause the vibration of atoms in the sample. Energy is absorbed at distinct frequencies for specific vibrational modes within the sample molecule. By varying the energy of the radiation, and tracking absorbance, a spectrum with signature peaks can be assigned to a molecule [8].

Infrared spectrometers have been commercially produced since the 1940s, and have benefitted from computer advancements, and largely from the use of the Fourier transform to process data; Fourier transform infrared spectroscopy (FTIR) is now the most common method of obtaining IR spectra. Briefly, FTIR spectrometers operate by changing the pathlength for two beams of infrared radiation, in most cases by the use of a Michelson interferometer and a polychromatic beam source. This produces an interferogram highlighting constructive and

25

destructive interference between the two beams. The raw interferogram can be converted into an infrared spectrum through the use of the Fourier transformation to obtain intensity as a function of wavenumber. FTIR spectrometers offer rapid, simultaneous data collection over large wavenumber ranges, with good signal to noise (SNR) ratios.

Reflection absorption infrared spectroscopy (RAIRS) uses commercially available IR spectrometers to produce an infrared beam that is reflected at grazing incidence from a reflective surface, in this work a Pd(100) single crystal. At a grazing incidence, the electric fields created parallel to the surface from s-polarized light (E_s and E_s') nearly cancel each other out, while the electric fields perpendicular to the surface arising from p-polarized light (E_p and E_p') are nearly doubled. The doubling of the electric field in the perpendicular direction to the surface enhances the intensity of vibrational modes of molecules with perpendicular components. As such, a polarizer is used to selectively obtain p-polarized light for use in RAIRS [9, 10]. This effect, known as the selection rule, is displayed in Figs. 2.8.1 and 2.8.2.

The detector used in this work is a Mercury Cadmium Telluride (MCT) detector. This detector gives increased sensitivity necessary when probing small concentrations typically found for surface-bound species. To reduce absorption from ambient pressure species, the IR beam is reflected to the sample in an enclosed, dry air purged path.
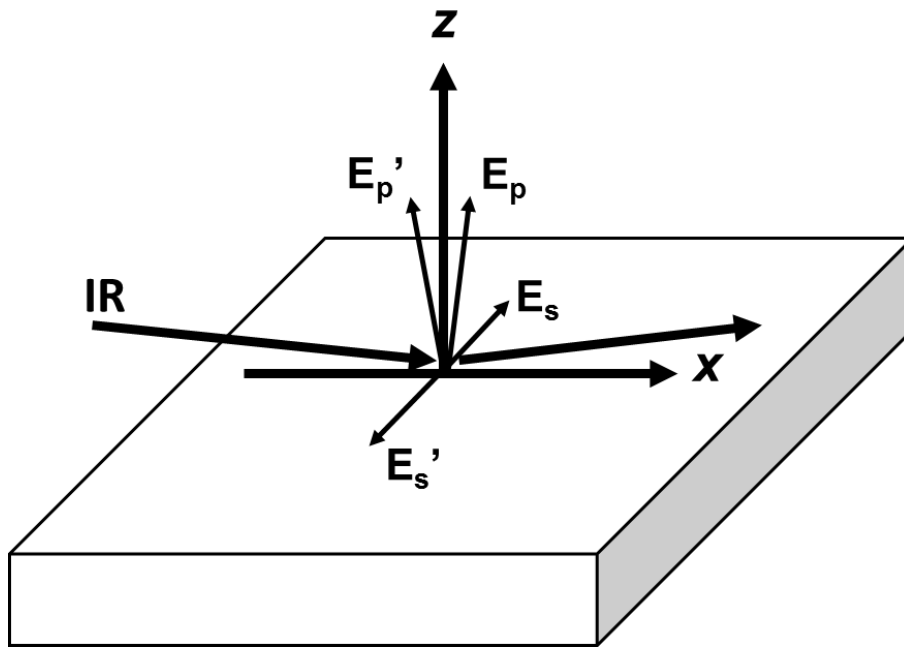
Figure 2.8.1 Diagram of electric fields produced from reflected and incident rays
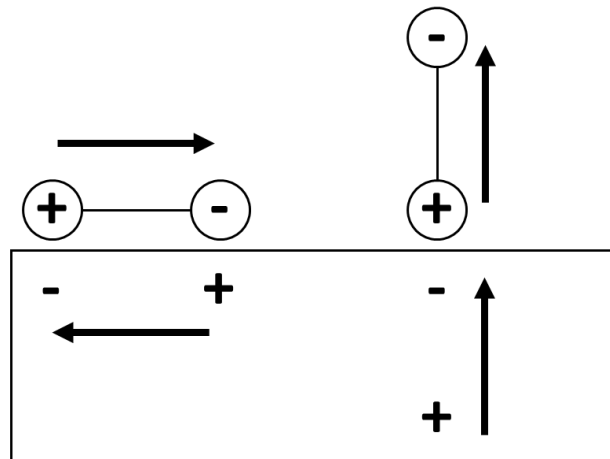
Figure 2.8.2 Diagram of subsurface image dipole effects

2.9 Auger Electron Spectroscopy (AES)

27

To measure cleanliness of a transition metal catalyst, AES can be used to identify surface contaminants present. AES relies on the identification of surface elements by measurement of the kinetic energy of ejected electrons that are characteristic of individual elements.

This process is achieved by impingement of the surface with an electron beam in the energy range of 2-10 keV, a sufficient energy to eject a core electron from a surface atom leaving it in an unstable, excited state. This excited state will relax with an electron from a higher energy level filling the core hole. This leaves a hole in the shallower energy level and an excess of energy resulting in the emission of an "Auger electron" with a specific kinetic energy [5]. This process is shown in Fig. 2.9.1.
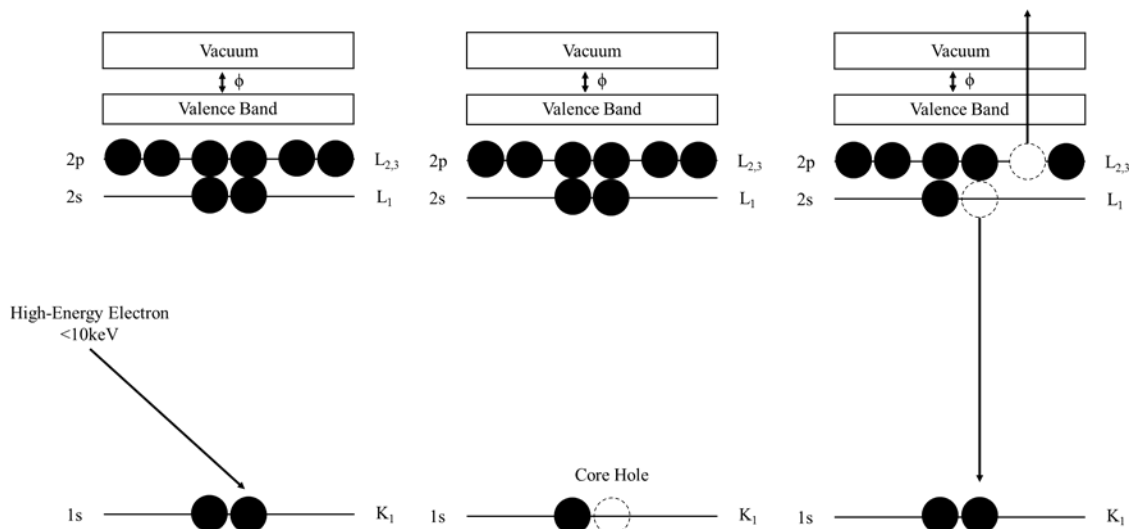
Figure 2.9.1 Diagram of Auger electron ejection

The energy of the emitted Auger electron, is specific to the transition that occurred in the atom. The kinetic energy can be quantified by equation 2.9.1:

$$E_{kin} = E_{K_1} - (E_{L_1} + E_{L_{2,3}}) \tag{2.9.1}$$

where the kinetic energy E_{kin} is equal to the energy of the electron the core shell minus the energy of the electrons in the outer shells. Since the energies of electrons in these orbitals are

unique to each atom, assignment of peaks in an Auger spectrum can be made to individual elements.

Direct measurement of Auger spectrums can be difficult as they are present with a large background of secondary electrons. For clarity, spectra are usually differentiated either through the use of an AC voltage or digitally, where the signal is then plotted as $\frac{dN(E)}{dE}$ vs. E_{kin} [11].

The Auger system employed in this work is a dual, electron gun-cylindrical mirror analyzer (CMA) to impinge incident electrons and measure auger electron emission. The resulting spectrum can be compared with standard spectra for each element in the Handbook of Auger Electron Spectroscopy [5] to determine cleanliness and composition of the surface. Typical settings for collecting an Auger spectrum: 3 kV beam voltage and 0.4 mA emission current.

2.10 References

[1] T.A. Delchar, Vacuum Physics and Techniques, Chapman and Hall, London, 1993.

[2] W.J. Whytenberg, R.M. Lambert, A Long-Lived Aluminium Evaporation Source for Controlled, Reproducible Deposition of Clean Ultra-Thin Films under UHV Conditions, J. Vac. Sci. Technol. A, 10 (1992).

[3] Z. Li, F. Gao, O. Furlong, W.T. Tysoe, Adsorption of carbon monoxide on Au/Pd(100) alloys in ultrahigh vacuum: Identification of adsorption sites, Surface Science, 604 (2010) 136-143.

[4] M.T. Garvey, J.A. Boscoboinik, L. Burkholder, J. Walker, C. Plaisance, M. Neurock, W.T. Tysoe, Structure of the Au/Pd(100) Alloy Surface, J. Phys. Chem. C, 116 (2012) 4692=4697.

[5] P.W. Palmberg, G.E. Riach, R.E. Weber, N.C. MacDonald, Handbook of Auger Electron Spectroscopy, Perkin Elmer Corp., Eden Prairie, MN, 1972.

[6] N. Saliba, D.H. Parker, B.E. Koel, Adsorption of oxygen on Au(111) by exposure to ozone, Surface Science, 410 (1998) 270-282.

[7] P.A. Redhead, Thermal desorption of gases, Vacuum, 12 (1962).

[8] B. Stuart, B. George, P. McIntyre, Modern Infrared Spectroscpy, Wiley, Chichester, 1996.

[9] R.G. Greenler, Infrared Study of Adsorbed Molecules on Metal Surfaces by Reflection Techniques, J. Chem. Phys., 44 (1966) 310-315.

[10] J. Fan, M. Trenary, Symmetry and the Surface Infrared Selection Rule for the Determination of the Structure of Molecules on Metal Surfaces, Langmuir, 10 (1994) 3649-3657.

[11] D.P. Woodruff, T.A. Delchar, Modern Techniques of Surface Science, Second Edition ed., Cambridge University Press, Cambridge, 1994.

Chapter 3

Adsorption Sites and Binding of Oxygen on Au/Pd(100) Alloys with High Gold Coverages

3.1 Introduction

Gold palladium alloys are used in a number of processes that include oxygen. For example, in the case of catalytic reactions, vinyl acetate monomer (VAM) is synthesized from ethylene and acetic acid on the presence of oxygen [1-10] and for the direct synthesis of hydrogen peroxide from hydrogen and oxygen [11]. Gold palladium alloys has also been found to effective for oxygen reduction in fuel cells.

In the following, the surface chemistry of oxygen is studied on model Au/Pd(100) alloy catalysts in ultrahigh vacuum to explore how alloying palladium with gold influences the binding strength and adsorption sites on the allow surface as a basis for understanding the effect on catalysis and oxygen reduction on fuel cells. The alloys are made by evaporating approximately four monolayers of gold onto a palladium single crystal substrate and by annealing to various temperatures to create an alloy thin film [12]. However, the structures of the alloys depend strongly on surface crystallography. In the case of Au/Pd(111) alloys, the gold and palladium atom distribution on the surfaces is almost random and is dominated by nearest-neighbor interactions between the gold and palladium [13, 14] and has been modeled using Monte Carlo methods [14]. In contrast, the longer-range interactions found on Au/Pd(100) surfaces lead to

31

the formation of ordered structures [15]. Because of these longer-range interactions, Au/Pd(100) alloys with gold coverages ≥0.5 monolayers (ML) contain only isolated palladium atoms with gold atoms as nearest neighbors, while at lower gold coverages, palladium-palladium bridge sites are present. It has been found that molecular oxygen only dissociates into atomic under ultrahigh vacuum conditions when the gold coverage is lower than ~0.5 ML[16] although adsorbed dioxygen species have been detected on Au/Pd(100) alloys. These effects are explored by dosing high-coverage Au/Pd(100) alloys with atomic oxygen using ozone [17, 18]. These studies are complemented by density functional theory calculation of the binding of atomic and molecular oxygen to high-gold-coverage alloys to compare with desorption energy measurements using temperature-programmed desorption, while the distribution of sites on the alloy surface is modeled using Monte Carlo simulations.

3.2 Experimental and Theoretical Methods

The apparatus used to collect reflection absorption infrared spectra (RAIRS) and temperature-programmed desorption (TPD) data has been described in detail elsewhere [19]. Briefly RAIR spectra were collected using a Bruker Equinox Fourier-transform infrared spectrometer, typically for 1000 scans at a resolution of 4 cm^{-1}. TPD data were collected at a heating rate of 3.7 K/s in another chamber equipped with a Dichor quadrupole mass spectrometer interfaced to a computer allowing up to five masses to be sequentially monitored in a single experiment as described elsewhere [20]. The sample could be cooled to 80 K in both chambers since it is in thermal contact with a liquid-nitrogen-filled reservoir, and could be resistively heated to ~1200 K.

32

The Pd(100) single crystal was cleaned using a standard procedure and its cleanliness monitored using Auger spectroscopy and TPD collected following oxygen adsorption [21]. Gold was evaporated from a small alumina tube furnace as described in detail elsewhere [12]. The gold coverage on the surface was monitored using Auger and X-ray photoelectron spectroscopies and the gold palladium alloy was formed according to a recipe developed by Lambert *et al* [22] and the gold coverages in the resulting alloy were measured using LEIS as described elsewhere [13].

Ozone was produced by an A2Z Ozone Inc., 5GLAB ozone generator where the output of the generator was connected *via* a Teflon tube directly to a high-precision variable leak valve through a 1 mm-diameter glass tube that was directed at the inlet of the leak valve to minimize ozone decomposition. The ozone was returned through an external concentric glass tube and led though a Teflon tube to a fume hood. The proportion of ozone in the gas mixture was maximized by monitoring the 32 (O_2^+) and 48 (O_3^+) signals in the mass spectrometer located inside the vacuum chamber and it is estimated that the ozone concentration in the gas mixture is ~4%.

The adsorption of oxygen on model Au/Pd(100) alloys was studied using first-principles, periodic density functional theory (DFT) calculations performed using the projector augmented wave (PAW) method [23, 24] as implemented in the Vienna *ab-initio* simulation package (VASP) code [25-27]. The exchange and correlation energies were calculated using the PBE (Perdew, Burke and Ernzerhof [28]) form of the generalized gradient approximation (GGA). The wavefunctions and electron density were converged to within 1×10^{-5} eV whereas geometric structures were optimized until the forces on the atoms were less than 0.03 eV/Å.

33

The alloy surface composition was modelled using Monte Carlo simulations as detailed previously [29] that allows for the specific distribution of four-fold hollow adsorption sites to be found for any surface alloy composition using lateral nearest neighbor interactions (Fig. 3.3.2). Simulated TPD spectra were created according to an established process [30]. Briefly, particles representing oxygen atoms are placed in four-fold hollow sites on the simulated surface (60 x 60 atom lattice), and different process such as diffusion, dimerization, and desorption are performed with increasing temperature using the calculated oxygen adsorption energies from DFT (Fig. 3.3.3).

3.3 Results

It has been found previously that O_2 adsorbs dissociatively on Au/Pd(100) alloys with
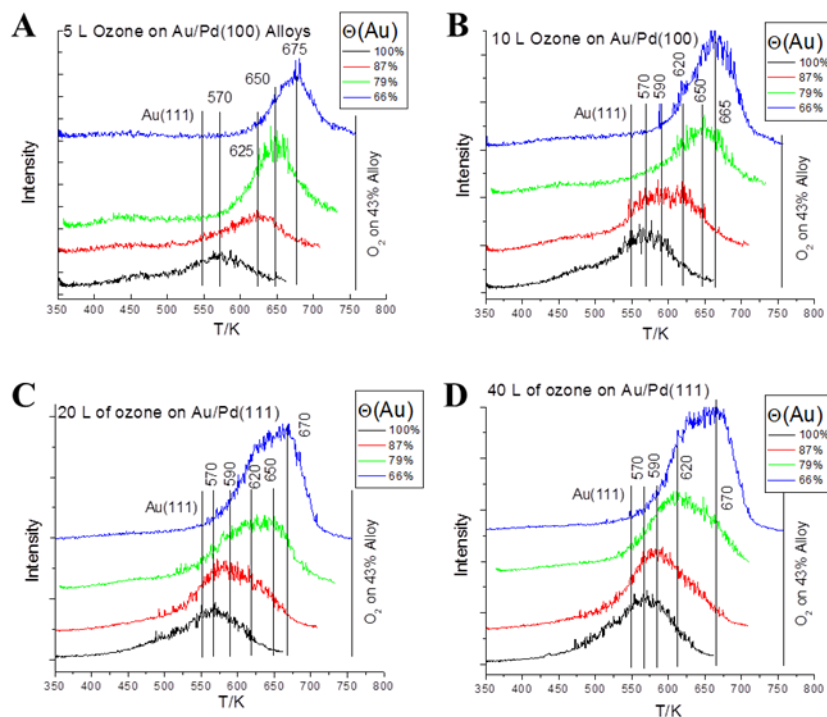
Figure 3.3.1: Temperature-programmed desorption data collected at 32 amu (O_2) of A/Pd(100) alloys with 100, 87, 79 and 66% gold, where the gold coverages are indicated on each figure with ozone exposures of (A) 5, (B) 10, (C) 20 and (D) 40 L (Langmuirs, 1 L = 1×10^{-6} Torr·s), using a heating rate of 4 K/s

34

gold coverages below ~0.5 ML and desorbs in a single peak centered at ~760 K without any strong dependence on the gold coverage [31]. However, since oxygen does not dissociatively adsorb onto surfaces with gold coverages >0.5 ML, oxygen is dosed onto these high-gold-coverage surfaces using ozone. The resulting 32 amu (O_2) temperature-programmed desorption (TPD) profiles are shown in Fig. 3.3.1 for various doses of oxygen (using various exposures of an O_3/O_2 mixture where a Au(111) surface saturates with a 80 L exposure) on various Au/Pd(100 alloys to probe the most stable adsorption sites, where the palladium coverage in the alloy is marked adjacent to the corresponding desorption profile. In all cases, the desorption temperatures for oxygen from alloys with coverages below 0.5 ML are indicated. The general trend is for the desorption temperature to increase as the gold coverage increases. However, molecular oxygen desorbs at ~570 K for the higher gold coverages in a symmetric peak with a temperature that remains approximately constant with increasing exposure. The symmetric peak profile is consistent with second-order desorption kinetics [32] but in contrast to oxygen
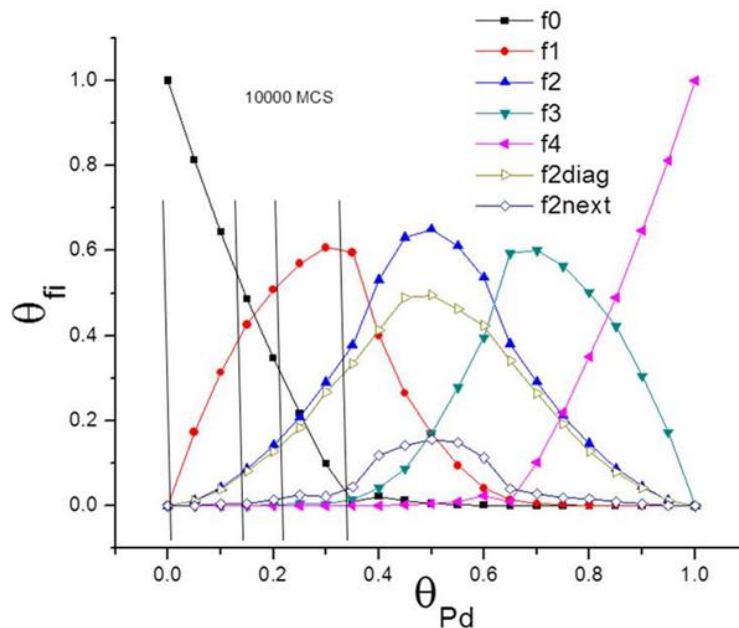
Figure 3.3.2: Plot of the proportion of types of four-fold hollow sites on Au/Pd(100), indicated as *fi*, where *i* refers to the number of palladium sites adjacent to the four-fold hollow site calculated using Monte Carlo simulations.

35

desorption from clean Pd(100) [33, 34] ascribed to lateral interactions [35]. This presumably occurs because the adsorption sites are sufficiently dilute to minimize such lateral interactions.

In order to explore how the available adsorption ensembles varies with composition, particularly at high gold coverages, we have carried out Monte Carlo simulations to explore the coverage of the most-stable four-fold hollow sites as a function of Au/Pd(100) alloy compositions using interaction parameters found previously for Au/Pd(100) alloys [36] and the results are displayed in Fig. 3.3.2. This reveals that for low palladium coverage (<0.5 ML), there are sites with no palladium neighbor ($f0$, ■), ones having a single nearest neighbor ($f1$, ●) and with two nearest neighbors ($f2$, ▲), that consist predominantly of diagonally distributed palladium atoms. Note also that the change in the proportion of $f4$ sites in the simulations at high palladium concentrations (Fig. 3.3.2) closely mimics the decrease in oxygen coverage on the Au/Pd(100) alloy surface for low palladium coverages [16], suggesting that a four-fold hollow site completely surrounded by palladium is required to dissociate molecular oxygen on the alloy.

$f1$
E_{ads}= -487 kJ/mol

$f2$
E_{ads}= -501 kJ/mol

Pd(100)
E_{ads}= -582 kJ/mol
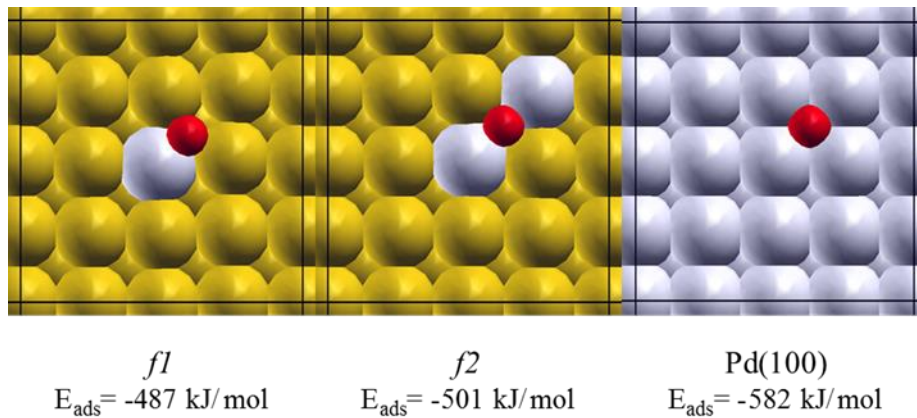
Figure 3.3.3: Structures and energies of the most-stable four-fold hollow sites on Au/Pd(100) alloys calculated using density functional theory. Oxygen atoms are indicated in red.

In order to gauge the effect of alloy composition on the heat of adsorption of adsorbed atomic oxygen on Au/Pd(100) alloys, we calculated the adsorption energy of atomic oxygen for

the predominant *f1* and *f2* sites compared to clean Pd(100) using density functional theory, and the results are displayed in Fig. 3.3.2. This suggests that there is a considerable effect of changing the nature of the Au/Pd ensemble on the heat of oxygen adsorption with the heat of adsorption of *f2* sites decreasing to ~500 kJ/mol and on *f1* sites to ~490 kJ/mol compared to ~580 kJ/mol on clean Pd(100). This will result in a lowering in the oxygen desorption activation energy and an increase in the activity of the adsorbed oxygen as found experimentally (Fig. 3.3.1), desorbing between ~600 and 650 K, compared to ~760 K for desorption from four-fold sites on alloys with high palladium contents.
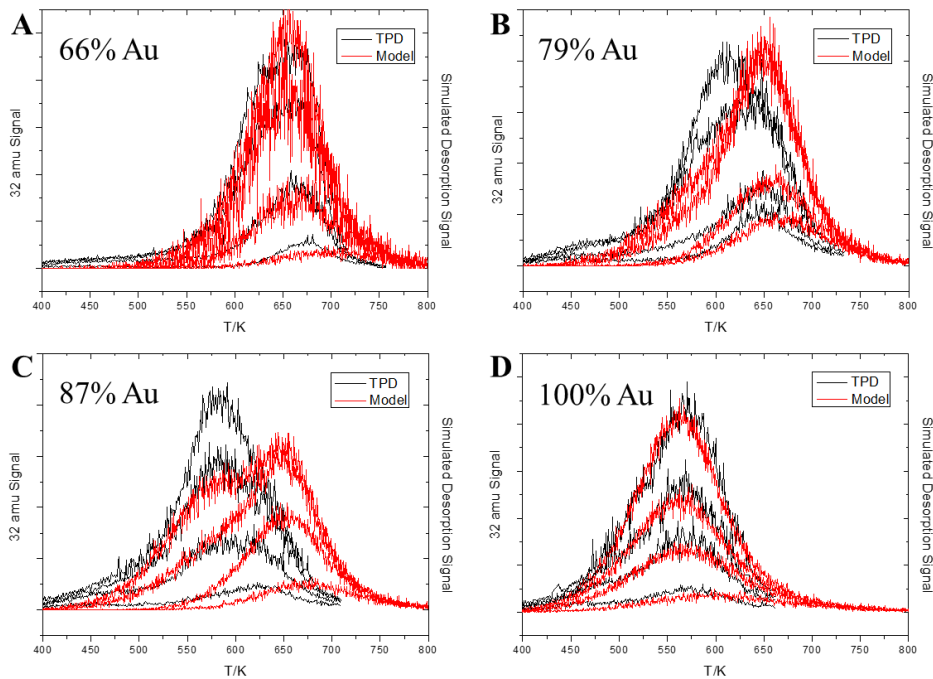
Figure 3.3.4: Plot of Monte Carlo model 1 with corresponding TPD data on 66 (A), 79 (B), 87 (C), and 100% (D) Au surface coverages.

Preliminary, simulated TPD spectra are shown in Figs. 3.3.4 and 3.3.5. Fig. 3.3.4 shows the results of the first Monte Carlo model (red) and the corresponding TPD spectra (black) on four alloy surface compositions with different concentrations of four-fold hollow sites (Fig. 3.3.2). In the first model, the ozone atoms are allowed to diffuse and dimerize, while dimers are

allowed to diffuse and desorb. The model in Fig. 3.3.5 only allows for diffusion of oxygen atoms and desorption of two nearest neighbor atoms. Good agreement is seen with both models at 66, 79, and 100% Au coverages for most surface-oxygen concentrations. In both models, the 87% Au alloy surface 32 amu TPD spectra were not well modelled with an appreciable trend to higher desorption temperatures, indicative of increased desorption from four-fold hollow sites with more Pd atoms present.
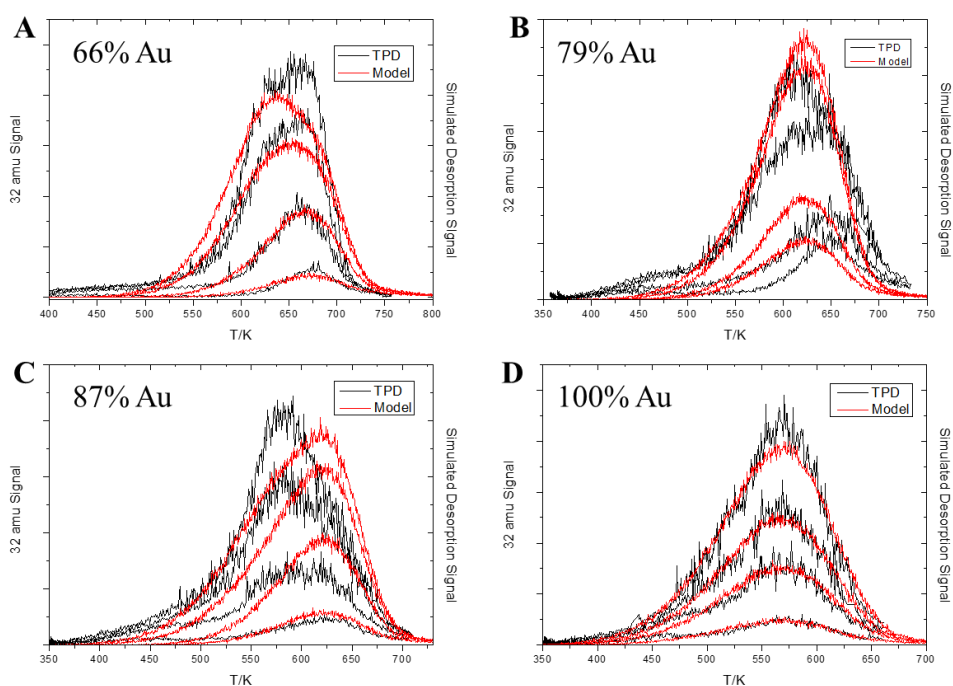
Figure 3.3.5: Plot of Monte Carlo model 2 with corresponding TPD data on 66 (A), 79 (B), 87 (C), and 100% (D) Au surface coverages.

3.4 Discussion

The general behavior of the TPD data for atomic oxygen on high-coverage Au/Pd(100) alloy is as expected with oxygen desorbing recombinatively with peak temperatures between the limits of that found on gold, where it desorbs at ~550 K, and on alloys with gold coverage below

~0.5 ML, where it desorbs at ~750 K. The trend with increasing gold content in the alloy is also what would be intuitively expected.

The results are analyzed in greater detail to identify how the variation in heat of adsorption of various sites influences the oxygen desorption. This can be accomplished by using the results of the Monte Carlo simulations (Fig. 3.3.2), where the alloy coverages for which the TPD data were collected are also marked on the figure. This shows that, at the lowest palladium coverage (Θ(Pd) = 0.14 ML, Θ(Au) = 0.66 ML), the surface contains predominantly four-fold hollow sites containing one (*f1*) palladium atoms (the remainder being gold). Note that a peak is also detected at 570 K for a gold overlayer on the palladium substrate. This is somewhat higher than the oxygen desorption peak from clean Au(111) (~550 K), suggesting some electronic modification of the gold film by the palladium below. This peak grows in intensity, but the peak position remains at ~570 K. In addition, the integrated areas under the desorption profiles for ozone on a gold film scales linearly with the oxygen coverage measured using the same apparatus on Au(111) [18] thereby providing a calibration for oxygen coverages on the alloys.

The plot in Fig. 3.3.2 indicates that oxygen occupies almost exclusively *f1* sites when the gold coverage in 0.87 ML. This oxygen desorbs at ~625 K with a low ozone exposure (Fig. 3.3.1 A), where oxygen is likely to only occupy *f1* (and only a small proportion of *f2*) sites. In order to establish whether the measured desorption peak temperature is consistent with the density functional theory measurements, the calculated heat of adsorption for an oxygen atom adsorbed on a *f1* site (Fig. 3.3.3, 303 kJ/mol) is used to estimate the activation energy for the desorption of O$_2$, $E_{act}(O_2)$ from:

$$E_{act}(O_2) \sim 2E_{ads}(O) - D(O = O) \qquad (1)$$

where $D(O = O)$ is the bond strength of molecular oxygen (498 kJ/mol). Note that, based on the oxygen coverage measured for ozone adsorption on Au(111) collected using the same system [18], the atomic oxygen coverage for a 5 L ozone exposure is ~0.09 ML, below the *f1* site coverage on this alloy. This predicts a desorption activation energy for two oxygen atoms adsorbed at *f1* sites of ~109 kJ/mol. In order to test this, the desorption activation energy was calculated from the low-exposure desorption profile (to exclude the effects of oxygen adsorption on the gold) by fitting it to an analytical solution to a second-order desorption process [32], which yields an activation energy of 110 ± 10 kJ/mol. As the ozone exposure increases, this peak broadens to lower temperatures so that, after a 40 L ozone exposure (Fig. 3.3.1D), the peak consists of an asymmetric profile comprising contributions from oxygen desorbing from gold (*f0*) and isolated palladium (*f1*) sites.

At higher palladium coverages, the coverage of both *f1* and *f2* sites increases, but without the appearance of any *f3* sites for the gold coverage range used in these experiments. In the case of the alloy with 0.79 ML of gold, (Θ(Pd) = 0.21 ML), the *f1* and *f2* site coverages are 0.52 and 0.1 ML, with ~0.3 ML of *f0* sites, while at a gold coverage of 0.66 ML (Θ(Pd) = 0.34 ML), the respective coverages increase to 0.6 and 0.3 ML, with negligible remaining *f0* sites. Thus, molecular oxygen can be produced from alloys with gold coverages less than ~0.8 ML from atomic oxygen adsorbed at both *f1* and *f2* sites. However, the integrated peak areas on the various alloys increase as the amount of palladium in the in the alloy increases indicating that the reactive sticking coefficient of ozone to deposit atomic oxygen also increases. In order to both determine the adsorption sites at which the molecular oxygen reacts to form molecular oxygen and to check the accuracy of the DFT calculations, the peak desorption temperatures of oxygen are compared for alloys with 87% gold (which contain almost exclusively *f1* sites) and 66% gold

40

where they contain both *f1* and *f2* sites. Since the second-order peak temperature depends on oxygen coverage, the oxygen coverages are measured from the integrated peak areas using the oxygen coverage calibration for ozone on Au(111). The value of k_2/β, where k_2 is the second-order desorption rate constant and β is the heating rate obtained by taking the oxygen desorption activation energy from the alloy with 0.87 ML of gold to be 110 kJ/mol with a peak temperature of 625 K. The desorption activation energies for oxygen formed by atomic oxygen only at *f2* sites is 126 kJ/mol using equation 1, and from a combination of *f1* and *f2* sites is 117.4 kJ/mol. This predicts that desorption from just *f2* sites should occur with a peak temperature at ~717 K, while desorption from a combination of *f1* and *f2* sites should be centered at 670 K. This implies that the ~675 K feature is due to desorption from oxygen adsorbed at both *f1* and *f2* sites. It should be noted that there are more *f1* sites available on this surface than *f2* sites, so that there could be a small amount of additional intensity in the low-temperature tail of the desorption profile for the 0.66 ML alloy in Fig. 3.3.1A, although the peak is quite symmetric as would be expected for a second-order desorption process [32]. Note that there is no evidence of any significant intensity at ~717 K that would indicate recombinative desorption from *f2* sites. This indicates that *f1* and *f2* sites are occupied with essentially equal probabilities.

As the ozone exposure to the alloy with 0.66 ML of gold increases, a shoulder appears on the desorption profile at an exposure of 10 L, and becomes more pronounced for an exposure of 20L of ozone. The oxygen coverage at this exposure is ~0.39 ML from the integrated desorption areas. However, the maximum coverage of available *f2* sites in this alloy is ~0.3 ML (Fig. 3.3.2) so that the extra oxygen on the *f1* sites initially desorbs as a low-temperature shoulder at ~670 K, while the remainder then desorbs from a combination of *f1* and *f2* sites. This trends continues when the ozone exposure increases to 40 L (Fig. 3.3.1D). This indicates that there is a clear

41

preference for oxygen at *f2* sites to react preferentially with f1 sites, presumably since the *f1* sites are adjacent to a palladium atom that is next to another palladium atom that forms the *f2* site.

A similar trend is seen for alloys with 0.79 ML of gold. However, in this case the much lower proportion of *f2* sites compared to *f1* sites (0.1 ML versus 0.5 ML) results in the high temperature (~670 K) shoulder being much smaller than the ~620 K peak, and also saturated at lower ozone exposures.

In order to corroborate the TPD spectra with the site distribution provided from the Monte Carlo simulations (Fig. 3.3.2), Monte Carlo TPD simulations were performed incorporating the distribution of four-fold hollow sites (Figs. 3.3.4 and 3.3.5), where very little distinguishing features between the models can be seen. It is immediately apparent that for both models studied, the desorption profiles can be well modelled for most gold coverages with the 66 (Figs. 3.3.4A and 3.3.5A) and 100% (Figs. 3.3.4D and 3.3.5D) gold coverage TPD spectra being reproduced most accurately at all ozone doses. Both models begin to deviate from the observed TPD spectra at high ozone doses on the 79% gold alloy (Figs. 3.3.4B and 3.3.5B), and significant differences are seen for the 87% gold surfaces (Figs. 3.3.4C and 3.3.5C). It appears that the number of *f0* sites is higher than predicted by Monte Carlo in both the 79 and 87% gold alloys than in the TPD data. The origin of this effect is unclear, and continued refinement of the Monte Carlo models used is currently underway. It is interesting to note that while ozone has been found previously chemisorb in a non-destructive manner with low doses, at high exposures gold clusters have been seen to form from surface extraction by ozone on gold single crystal surfaces[37, 38]. This effect on alloy surfaces with high gold coverages has not been studied, but could offer the possibility of gold enrichment of the surface causing increased desorption from *f0* sites as seen in the TPD data for the high ozone doses of 79 and 87% gold coverage,

42

where presumably the 66% surface is not gold enriched enough for extraction of gold clusters to occur.

3.5 Conclusion

The desorption behavior of oxygen adsorbed via controlled ozone dosing has been described through careful analysis using TPD and DFT in conjunction with previous Monte Carlo work to identify the possible desorption sites available on each alloy surface. Current Monte Carlo TPD simulations are underway to recreate the temperature programmed desorption profiles using the calculated binding energies from DFT. Preliminary results from TPD MC simulation overall fit the TPD data well, but suggest that on 87% Au/Pd alloy surfaces that significant extraction of gold atoms, increasing the coverage of gold, may occur via previously reported mechanisms.

3.6 References

[1] F. Calaza, Z. Li, M. Garvey, M. Neurock, W. Tysoe, Reactivity and Selectivity in the Au/Pd(111) Alloy-Catalyzed Vinyl Acetate Synthesis, Catal Lett, 143 (2013) 756-762.

[2] F. Calaza, Z.J. Li, W.T. Tysoe, Reaction Between Ethylene and Acetate Species on Clean and Oxygen-Covered Pd(100): Implications for the Vinyl Acetate Monomer Formation Pathway, Catal Lett, 141 (2011) 266-270.

[3] F. Calaza, M. Mahapatra, M. Neurock, W.T. Tysoe, Disentangling ensemble, electronic and coverage effects on alloy catalysts: Vinyl acetate synthesis on Au/Pd(1 1 1), Journal of Catalysis, 312 (2014) 37-45.

[4] F. Calaza, D. Stacchiola, M. Neurock, W.T. Tysoe, Kinetic Parameters for the Elementary Steps in the Palladium-Catalyzed Synthesis of Vinyl Acetate, Catal Lett, 138 (2010) 135-142.

[5] F. Calaza, D. Stacchiola, M. Neurock, W.T. Tysoe, Coverage Effects on the Palladium-Catalyzed Synthesis of Vinyl Acetate: Comparison between Theory and Experiment, Journal of the American Chemical Society, 132 (2010) 2202-2207.

[6] M. Chen, D. Kumar, C.-W. Yi, D.W. Goodman, The Promotional Effect of Gold in Catalysis by Palladium-Gold, Science, 310 (2005) 291-293.

[7] Y.F. Han, D. Kumar, C. Sivadinarayana, A. Clearfield, D.W. Goodman, The Formation of PdC<sub>x</sub> over Pd-Based Catalysts in Vapor-Phase Vinyl Acetate Synthesis: Does a Pd–Au Alloy Catalyst Resist Carbide Formation?, Catal Lett, 94 (2004) 131-134.

[8] M. Neurock, W. Tysoe, Mechanistic Insights in the Catalytic Synthesis of Vinyl Acetate on Palladium and Gold/Palladium Alloy Surfaces, Topics in Catalysis, 56 (2013) 1314-1332.

[9] D. Stacchiola, F. Calaza, L. Burkholder, A.W. Schwabacher, M. Neurock, W.T. Tysoe, Elucidation of the Reaction Mechanism for the Palladium-Catalyzed Synthesis of Vinyl Acetate, Angewandte Chemie International Edition, 44 (2005) 4572-4574.

[10] D. Stacchiola, F. Calaza, L. Burkholder, W.T. Tysoe, Vinyl Acetate Formation by the Reaction of Ethylene with Acetate Species on Oxygen-Covered Pd(111), Journal of the American Chemical Society, 126 (2004) 15384-15385.

[11] B.E. Solsona, J.K. Edwards, P. Landon, A.F. Carley, A. Herzing, C.J. Kiely, G.J. Hutchings, Direct Synthesis of Hydrogen Peroxide from H2 and O2 Using Al2O3 Supported Au—Pd Catalysts, ChemInform, 37 (2006) no-no.

[12] W.J. Wytenberg, R.M. Lambert, A Long-Lived Aluminium Evaporation Source for Controlled, Reproducible Deposition of Clean Ultra-Thin Films under UHV Conditions, Journal of Vacuum Science and Technology A, 10 (1992) 2.

[13] Z.J. Li, O. Furlong, F. Calaza, L. Burkholder, H.C. Poon, D. Saldin, W.T. Tysoe, Surface segregation of gold for Au/Pd(111) alloys measured by low-energy electron diffraction and low-energy ion scattering, Surface Science, 602 (2008) 1084-1091.

[14] J.A. Boscoboinik, C. Plaisance, M. Neurock, W.T. Tysoe, Monte Carlo and density functional theory analysis of the distribution of gold and palladium atoms on Au/Pd(111) alloys, Physical Review B, 77 (2008).

[15] M. Garvey, J.A. Boscoboinik, L. Burkholder, J. Walker, C. Plaisance, M. Neurock, W.T. Tysoe, The Structure of the Au/Pd(100) Alloy Surface, Journal of Physical Chemistry C, Submitted (2011).

[16] Z. Li, F. Gao, W.T. Tysoe, Carbon Monoxide Oxidation over Au/Pd(100) Model Alloy Catalysts†, The Journal of Physical Chemistry C, 114 (2010) 16909-16916.

[17] N. Saliba, D.H. Parker, B.E. Koel, Adsorption of oxygen on Au(111) by exposure to ozone, Surface Science, 410 (1998) 270-282.

[18] T. Thuening, J. Walker, H. Adams, O. Furlong, W.T. Tysoe, Kinetics of low-temperature CO oxidation on Au(111), Surface Science, 648 (2016) 236-241.

[19] M. Kaltchev, A.W. Thompson, W.T. Tysoe, Reflection-absorption infrared spectroscopy of ethylene on palladium (111) at high pressure, Surface Science, 391 (1997) 145-149.

[20] D. Stacchiola, W.T. Tysoe, The effect of subsurface hydrogen on the adsorption of ethylene on Pd(1 1 1), Surface Science, 540 (2003) L600-L604.

[21] G. Wu, M. Kaltchev, W.T. Tysoe, The Kinetics and Infrared Spectroscopy of C_1 Hydrocarbons Adsorbed on Clean and Oxygen-modified Mo(100), Surface Review and Letters, 6 (1999) 9.

[22] C.J. Baddeley, M. Tikhov, C. Hardacre, J.R. Lomas, R.M. Lambert, Ensemble Effects in the Coupling of Acetylene to Benzene on a Bimetallic Surface: A Study with Pd{111}/Au, The Journal of Physical Chemistry, 100 (1996) 2189-2194.

[23] G. Kresse, D. Joubert, From ultrasoft pseudopotentials to the projector augmented-wave method, Physical Review B, 59 (1999) 1758-1775.

[24] P.E. Blöchl, Projector augmented-wave method, Physical Review B, 50 (1994) 17953-17979.

[25] G. Kresse, J. Hafner, Ab initio molecular dynamics for liquid metals, Physical Review B, 47 (1993) 558-561.

[26] G. Kresse, J. Furthmüller, Efficiency of ab-initio total energy calculations for metals and semiconductors using a plane-wave basis set, Computational Materials Science, 6 (1996) 15-50.

[27] G. Kresse, J. Furthmüller, Efficient iterative schemes for ab initio total-energy calculations using a plane-wave basis set, Physical Review B, 54 (1996) 11169-11186.

[28] J.P. Perdew, K. Burke, M. Ernzerhof, Generalized Gradient Approximation Made Simple, Physical Review Letters, 77 (1996) 3865.

[29] M.T. Garvey, J.A. Boscoboinik, L. Burkholder, J. Walker, C. Plaisance, M. Neurock, W.T. Tysoe, Structure of the Au/Pd(100) Alloy Surface, J. Phys. Chem. C, 116 (2012) 4692=4697.

[30] J.L. Sales, R.O. Unac, M.V. Gargiulo, V. Bustos, G. Zgrablich, Monte Carlo Simulation of Temperature Programmed Desorption Spectra: A Guide through the Forest for Monomolecular Adsorption on a Square Lattice, Langmuir, 12 (1996) 95-100.

[31] Z. Li, F. Gao, W.T. Tysoe, Carbon Monoxide Oxidation over Au/Pd(100) Model Alloy Catalystst, Journal of Physical Chemistry C, 114 (2010) 16909-16916.

[32] P.A. Redhead, Thermal desorption of gases, Vacuum, 12 (1962) 203-211.

46

[33] G.W. Simmons, Y.N. Wang, J. Marcos, K. Klier, Oxygen adsorption on palladium(100) surface: phase transformations and surface reconstruction, The Journal of Physical Chemistry, 95 (1991) 4522-4528.

[34] S.L. Chang, P.A. Thiel, Oxygen on Pd(100): Order, reconstruction, and desorption, The Journal of Chemical Physics, 88 (1988) 2071-2082.

[35] Y. Zhang, V. Blum, K. Reuter, Accuracy of first-principles lateral interactions: Oxygen at Pd(100), Physical Review B, 75 (2007) 235406.

[36] M. Garvey, J.A. Boscoboinik, L. Burkholder, J. Walker, C. Plaisance, M. Neurock, W.T. Tysoe, Structure of the Au/Pd(100) Alloy Surface, The Journal of Physical Chemistry C, 116 (2012) 4692-4697.

[37] B.K. Min, X. Deng, D. Pinnaduwage, R. Schalck, C.M. Friend, Oxygen-induced restructuring with release of gold atoms from Au(111), Phys. Rev. B, 72 (2005) 121410-121411-121410-121414.

[38] T.A. Baker, B. Xu, X. Liu, E. Kaxiras, C.M. Friend, Nature of Oxidation of the Au(111) Surface: Experimental and Theoretical Investigation, J. Phys. Chem. C Lett., 113 (2009) 16561-16564.

Chapter 4

The Adsorption of Ethylene on Au/Pd(100) Alloy Surfaces

4.1 Introduction

The Lambert group carried out much of the early work on small hydrocarbons on Pd(111) surfaces focusing on ethylene [1, 2] adsorption and the cyclotrimerization of acetylene to benzene [3-6]. This work, along with Lambert's early studies showing the formation of acetate species from acetic acid on Pd(111) [7] formed the basis for exploring the mechanism of palladium-catalyzed coupling between ethylene and acetic acid to form vinyl acetate monomer (VAM) on a Pd(111) model catalyst surface. It was demonstrated that the reaction proceeds *via* a pathway first proposed by Samanos [8] in which ethylene reacts with adsorbed acetate species to form an acetoxyethyl-palladium intermediate, which yields VAM *via* a *β*-hydride elimination reaction [9, 10].

This reaction is catalyzed both by supported palladium and palladium-gold alloys, where alloying with gold leads to a substantial increase in selectivity from ~85% for pure palladium to approximately 92% for the alloy. Catalytic studies on model gold-palladium alloys showed that Au-Pd(100) alloys were the most active and proposed that the active ensemble consists of two gold atoms located at diagonally opposite corners of the square unit cell located on a (100) surface [11-14].

The reaction was found to also proceed *via* the Samanos pathway on Au/Pd(111) alloys, where a combination of electronic, ensemble and coverage effects were found the change the rate-limiting step in the surface reaction pathway [15, 16]. Ethylidyne forms on Pd(111) as the reaction proceeds [17] to maintain a crowded surface that inhibits product decomposition, thereby increasing reaction selectivity. Ethylidyne forms on Pd(111) *via* an intermediate vinyl species [18] and is stabilized by the availability of three-fold sites on the surface [19]. These become less prevalent on Au/Pd(111) alloys as the gold coverage increases; here product decomposition is inhibited by the alloy. Ethylene adsorption has been studied on clean Pd(100) [20, 21]. In this case, both π- and di-σ-bonded ethylene were found at low temperatures, and the π-bonded form desorbs between 100 and 300 K and the di-σ form has a σ-π parameter of 0.78 [22]. This work also suggested that a vinyl intermediate was stabilized, its conversion to ethylidyne being prevented by the absence of three-fold hollow sites on Pd(111). This observation is of particular relevance to VAM synthesis since an alternative pathway suggested by Moiseev [23, 24] proposes that VAM is formed by a direct coupling between vinyl and acetate species.

Accordingly, the surface chemistry of ethylene is studied on Au/Pd(100) alloys. In addition, it has been shown that alloying palladium with coinage metals, for example, gold results in an enhanced hydrogenation activity and selectivity [25] and has been investigated theoretically using density functional theory (DFT) calculations [26, 27].

The surface chemistry of ethylene has been investigated previously on Au-Pd(111) alloys [28] where it was found that, for gold coverages greater than ~0.7 monolayer (ML) ethylene adsorbs with a heat of adsorption less than 55 kJ/mol. At gold coverages between ~0.5 and ~0.7 ML, ethylene adsorbs on palladium sites in a π-bonded configuration desorbing with an

49

activation energy between ~57 and 62 kJ/mol. Varying the gold coverage in the alloy results in an almost linear increase in the ethylene desorption activation energy with increasing palladium coverage, eventually reaching a value of ~76 kJ/mol, close to that found on ethylene on clean Pd(111).

The distribution of gold and palladium on the surface of Au/Pd(100) alloys is quite different from the (111) alloy surfaces. In the latter case, it was found that only nearest-neighbor interactions between the gold and palladium in the surface were important, leading to an almost random distribution on the surface but with a somewhat higher concentration of isolated palladium atoms than expected for a completely random distribution [29]. In contrast, much longer-range interactions (up to third-nearest neighbors) were found on Au/Pd(100) model alloys, resulting in the formation of ordered LEED patterns [30]. It was found for low gold coverages that the surface contained mostly Pd-Pd bridge sites as expected. As the gold coverage increased, the coverage of bridge sites became vanishingly small for gold coverages lower than ~0.5 ML, where the surface comprised predominantly isolated palladium atoms with only gold nearest neighbors.

4.2 Experimental Methods

The apparatus used to collect reflection absorption infrared spectra (RAIRS) and temperature-programmed desorption (TPD) data has been described in detail elsewhere [31]. Infrared spectra are collected with Bruker Equinox spectrometer, typically for 1000 scans at a resolution of 4 cm^{-1}. TPD data were collected using a Dichor quadrupole mass spectrometer interfaced to a computer that allowed up to five masses to be monitored in a single experiment. The sample could be cooled to 80 K by thermal contact to a liquid-nitrogen-filled reservoir and

resistively heated to ~1200 K.

The Pd(100) single crystal was cleaned using a standard protocol and its cleanliness monitored using Auger spectroscopy and TPD collected following oxygen adsorption [32]. Gold was evaporated from a small alumina tube [33], which enabled controlled and reproducible evaporation rates to be achieved. In order to precisely control the temperature of the gold, and therefore its evaporation rate, a C-type thermocouple was placed into the gold pellet. The amount of gold deposited onto the surface was monitored using Auger spectroscopy from the peak-to-peak intensities of the Au NVV and Pd MNN Auger features and the monolayer coverage was gauged from breaks in the gold uptake signal. The gold palladium alloy was formed according to a recipe developed by Lambert *et al* [6] on Pd(111) surfaces by initially adsorbing four monolayers of gold, then annealing to various temperatures for a period of five minutes in ultrahigh vacuum to produce the desired Au/Pd atomic ratio on the surface. The ethylene (Matheson, Research Grade) was transferred to glass bottles which were attached to the gas-handling line for introduction into the vacuum chamber.

4.3 Results

TPD data were collected at a heating rate of 3.7 K/s as a function of ethylene exposure to various Au/Pd(100) alloy surfaces and the ethylene was dosed from a capillary source to minimize the rise in background pressure. Exposures are quoted in Langmuirs (1 L = 1×10^{-6} Torr s) where the dosing source pressure-enhancement factor was calibrated by comparing coverages obtained from the source and by back-filling the chamber with ethylene. Exposures are not corrected for ionization gauge sensitivity.

Figure 4.3.1 displays a series of 27 amu (ethylene) desorption profiles as a function of

51
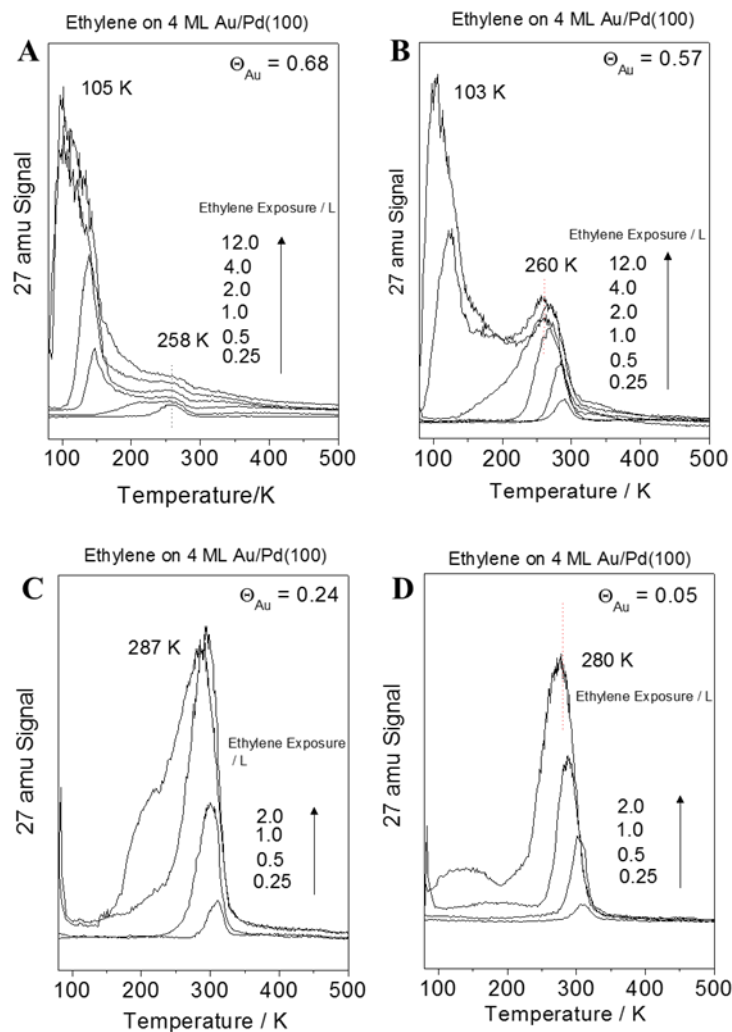
Figure 4.3.1: Temperature-programmed desorption spectra for various exposures of ethylene adsorbed at 80 K on Au/Pd(100) alloys with gold coverages of (A) 0.68, (B) 0.57, (C) 0.24 and (D) 0.05 ML, collected using a heating rate of 3.7 K/s. The ethylene exposures are marked adjacent to the corresponding spectrum.

ethylene exposure for some selected alloys with gold coverages of 0.68 (Fig. 4.3.1A), 0.57 (Fig. 4.3.1B), 0.24 (Fig. 4.3.1C) and 0.05 (Fig. 4.3.1D) ML. When the palladium coverage is relatively low ((Θ_{Pd}=0.32 ML, Fig. 4.3.1A), the desorption profile consists of a small feature centered at ~258 K and a larger feature that grows with increasing ethylene exposure and shifts from a peak desorption temperature of ~150 K at low coverages to lower temperature as the coverage increases. The shape of the profile at the largest ethylene exposures suggests that it is due to the trailing edge of a peak below the adsorption temperature (~80 K). This indicates that the small, high-temperature (~258 K) peak is due to ethylene adsorbed on palladium sites, while

52

the low-temperature feature is due to adsorption on gold sites. Reducing the gold coverage to 0.57 ML results in an increase in the ethylene yield in the high-temperature state (Fig. 4.3.1B) and a decrease in the population of the low-temperature state, consistent with the high-temperature desorption state being due to adsorption on palladium sites. The peak temperature of the high-temperature desorption states decreases from ~290 K at low coverages to ~260 K at saturation, indicative of repulsive lateral interactions between adsorbed ethylene molecules. A lower-temperature state grows at ~130 K after an ethylene exposure of ~4 L, decreasing to lower temperatures as the exposure increases further.

This trend continues when the gold coverage is reduced to ~0.24 ML (Fig. 4.3.1C) where the high-temperature feature increases in intensity and shifts to ~287 K at saturation. The desorption spectrum found with only 0.05 ML of gold (Fig. 4.3.1D) has a high-temperature desorption feature at ~280 K at saturation and a broad, lower-temperature feature.

In order to explore the most stable ethylene adsorption sites on Au/Pd(100) alloys in
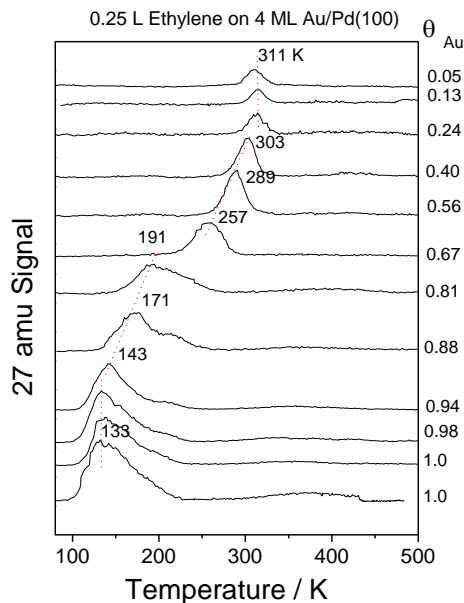
Figure 4.3.2: Temperature-programmed desorption spectra for 0.25 L of ethylene dosed at 80 K on various Au/Pd(100) alloys where the gold coverage is indicated adjacent to the corresponding desorption trace, collected using a heating rate of 3.7 K/s.

greater detail, various alloy surface were dosed with low exposure (0.25 L) of ethylene and the resulting 27 amu desorption profiles are displayed in Fig. 4.3.2. This shows that, for very low palladium coverages, ethylene adsorbs weakly at gold sites and desorbs at ~133 K. As the gold coverage decreases, there is a significant increase in desorption temperature up to a gold coverage of ~0.24 ML, after which the peak temperature remains constant at ~311 K for lower gold coverages. The heat of adsorption is estimated from the desorption activation energy using the Redhead equation [34] using the experimental heating rate (3.7 K/s) and assuming a standard pre-exponential factor of 1×10^{13} s^{-1}. The results are displayed in Fig. 4.3.3 as a function of palladium coverage in the alloy (▲), which shows a rather smooth increase in heat of adsorption from ~33 kJ/mol for the completely gold-covered surface ($\Theta_{Pd} = 0$) to a value of ~80 kJ/mol when the gold coverage decreases to ~0.4 ML ($\Theta_{Pd} = 0.6$), and then remains rather constant at higher palladium coverages. This curve also plots the coverages of Pd–Pd bridge (●) and
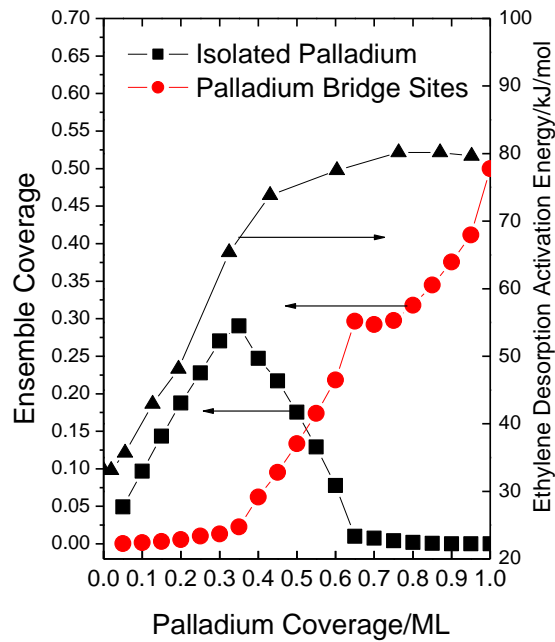
Figure 4.3.3: Plot of the low-coverage desorption activation energy of ethylene on various Au/Pd(100) alloys as a function of the gold coverage, where the desorption activation energies are calculated using the Redhead equation from the data in Fig. 4.3.2.

isolated Pd (■) sites on the Au/Pd(100) alloy surface obtained using Monte Carlo simulation [30]. This indicates that the desorption activation energy remains constant at ~80 kJ/mol when palladium bridge sites are present on the surface and decreases as isolated palladium sites appear.

The infrared spectra for saturation ethylene coverages on various Au/Pd(100) alloys (obtained using ethylene doses of 10 or 12 L) are displayed in Figs. 4.3.4 and 4.3.5 as a function of annealing temperature. The spectra were measured immediately after dosing at 80 K and then after heating to the indicating temperature for a period of 10 s. The spectra were collected at a sample temperature of 80 K.
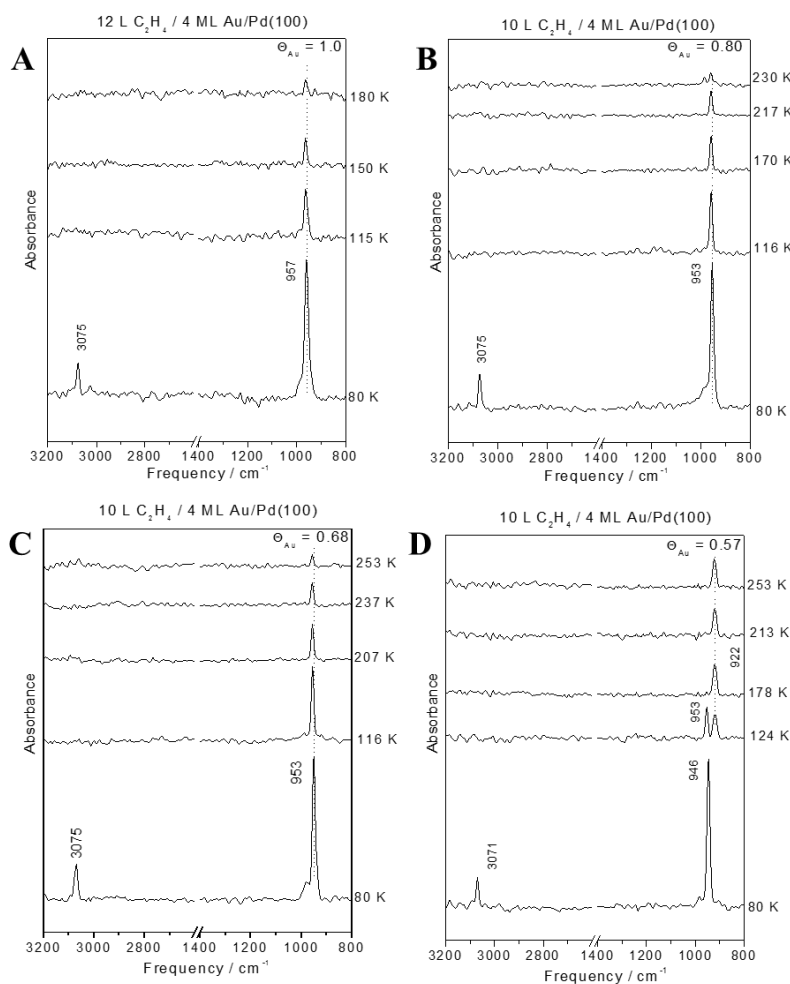
Figure 4.3.4: Reflection-absorption infrared spectra of 12 L of ethylene on Au/Pd(100) alloys with gold coverages of (A) 1.0, (B) 0.8, (C) 0.68, and (D) 0.57 ML as a function of annealing temperature where the annealing temperatures are marked adjacent to the corresponding spectrum.

55

Fig. 4.3.4A shows the infrared spectrum of ethylene adsorbed on a gold-saturated surface, which displays features at 957 and 3075 cm^{-1} immediately following ethylene adsorption at 80 K. The 957 cm^{-1} mode is assigned to a CH$_2$ wagging mode while that at 3075 cm^{-1} is due to a CH stretch. The latter mode should not be infrared allowed if the molecular plane of ethylene lies parallel to the surface [35] and suggests the formation of some second-layer ethylene at 80 K. Heating to ~115 K yields a single peak at ~957 cm^{-1} and a similar feature is found on a gold-saturated Au/Pd(111) alloy [28]. This feature is substantially attenuated by heating to ~180 K and disappears on annealing above ~180 K in accord with the TPD data (Fig. 4.3.2).

Similar results are obtained at slightly lower gold coverages (Θ_{Au} = 0.8 ML, Fig. 4.3.4B) where second-layer ethylene desorbs on heating to ~116 K and a sharp peaks remains at ~953 cm^{-1} but which persists to slightly higher temperature (>230 K). This trend continues for a gold coverage of 0.68 ML (Fig. 4.3.4C) where a ~953 cm^{-1} mode persists on heating to ~253 K and only completely disappears on heating to higher temperatures. This is in accord with the TPD data that shows that ethylene desorbs at ~191 K for a gold coverage of 0.81 ML and increases to 257 K when the gold coverage decreases to 0.67 ML (Fig. 4.3.2). The desorption profiles for an alloy with 0.68 ML of gold as a function of ethylene coverage (Fig. 4.3.1A) exhibit the most-intense desorption state at ~150 K, with a broad tail extending to higher temperatures. This is consistent with the change in infrared intensity with temperature seen in Fig. 4.3.4C. The number of isolated palladium atoms (completely surrounded by gold) on the Au/Pd(100) alloy reaches its maximum at this gold coverage, but has no Pd–Pd bridge sites (Fig. 4.3.3) [36].

Bridge sites appear on an alloy with a gold coverage of 0.57 ML, which results in significant changes to the infrared spectrum (Fig. 4.3.4D) and TPD (Fig. 4.3.1B). Weakly adsorbed ethylene (at ~953 cm^{-1}) desorbs by ~180 K, corresponding to the low-temperature peak

in TPD (Fig. 4.3.1B), resulting in the appearance of a feature at ~922 cm^{-1}, which persists at 253 K and is associated with an intense, high-temperature (~260 K) desorption state (Fig. 4.3.1B).

Similar infrared appear when the alloy gold coverage is 0.4 ML (Fig. 4.3.5A) and the isolated palladium site coverage has decreased considerably (Fig. 4.3.3) yielding vibrational modes at 942 and 906 cm^{-1}. The 942 cm^{-1} peak disappears on heating to ~200 K, while the ~906 cm^{-1} feature persist at 257 K.

As the gold coverage is reduced to 0.24 ML, and only Pd–Pd bridge sites are present on
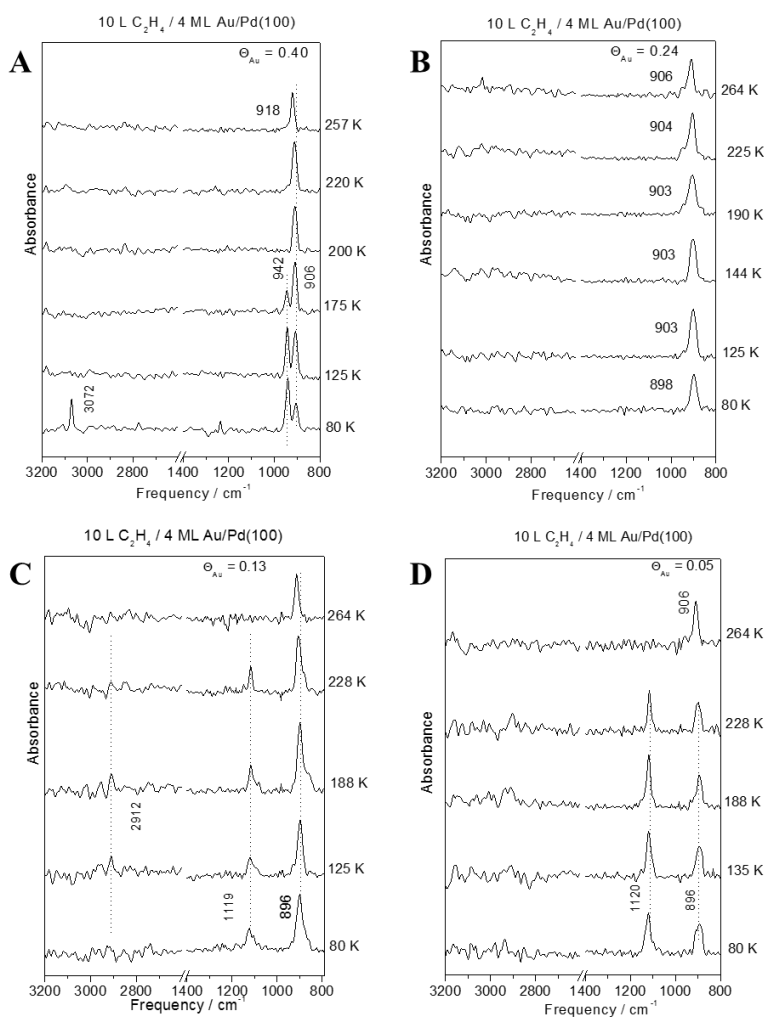
Figure 4.3.5: Reflection-absorption infrared spectra of 10 L of ethylene on Au/Pd(100) alloys with gold coverages of (A) 0.4, (B) 0.24, (C) 0.13, and (D) 0.05 ML as a function of annealing temperature where the annealing temperatures are marked adjacent to the corresponding spectrum.

57

the surface (Fig. 4.3.3), the infrared spectrum (Fig. 4.3.5B) consists of a relatively broad feature at ~904 cm^{-1} that is still present on heating to ~264 K and the corresponding desorption profile (Fig. 4.3.1C) displays a broad, low-temperature feature and a desorption peak centered at ~287 K consistent with the continued presence of the ~904 cm^{-1} infrared feature when heating to ~264 K.

The desorption profiles change little as the gold coverage decreases (Fig. 4.3.1D), while the infrared spectra change considerably. At a gold coverage of 0.13 ML (Fig. 4.3.5C), a new feature appears at ~1119 cm^{-1} along with an intense peak at ~896 cm^{-1}. The ~1119 cm^{-1} peak disappears on heating to 264 K, yielding a spectrum with a single feature at ~904 cm^{-1}. A similar spectral evolution is seen for a gold coverage of 0.05 ML (Fig. 4.3.5D), where the spectrum has peaks at 1120 and 896 cm^{-1}. The 1120 cm^{-1} feature disappears on heating to 264 K. The ~896 cm^{-1} feature becomes narrower on heating and shifts to ~906 cm^{-1}. Similar frequencies are found for ethylene on clean Pd(100) using high-resolution electron energy loss spectroscopy (HREELS) at 1135 and 920 cm^{-1} [8].

4.4 Discussion

The general trends observed for ethylene adsorbed on Au/Pd(100) alloys are similar to those found on Au/Pd(111) alloys [28] where decreasing the gold coverage in the alloy substantially increases the heat of ethylene adsorption and is accompanied by a continuous increase in σ-π parameters as the palladium coverage varies from close to zero (with a σ-π parameter ~0.08) to close to unity (with a σ-π parameter ~0.8) (Figs. 4.3.2 and 4.3.3). The infrared spectra of ethylene on Au/Pd(100) alloys at the highest gold coverages exhibit a single vibrational mode at ~955 cm^{-1} (Fig. 4.3.4 A (Θ_{Au}=1.0 ML), B (Θ_{Au} =0.8 ML), C (Θ_{Au}=0.68 ML), close to the CH2 wagging mode frequency found for ethylene on Au(111) [11]. A mode at this

frequency has been similarly assigned to ethylene adsorbed on gold sites on Au/Pd(111) alloys [28]. Ethylene desorbs from Au(110) in a broad feature centered at ~150 K when collected using a relatively high heating rate (11 K/s). Data collected at a lower heating rate (2.35 K/s, closer to the value used in this work) reveal a desorption feature centered at ~120 K, with a broad, higher-temperature tail extending to ~200 K [37] in reasonable agreement with the peak desorption temperatures at the highest gold coverages (Figs. 4.3.1 A-C).

For alloys with larger gold coverages, when only isolated palladium sites are present, for Θ_{Pd} from 0 to ~0.35 ML (Θ_{Au} from 1 to ~0.65 ML), ethylene exhibits a vibrational frequency of ~953 cm^{-1} and the desorption activation energy increases from ~33 to 65 kJ/mol (Fig. 4.3.3). The vibrational frequency indicates that the ethylene is π-bonded with a low σ-π parameter, which is similar for ethylene adsorbed on gold and isolated palladium sites.

Previous DFT calculations by Ge and Neurock found that the bridge site was the most stable for ethylene on Pd(100) with a heat of adsorption of ~90 kJ/mol [38]. The species is considerably rehybridized and the CH$_2$ plane is found to be tilted almost 30° away from the surface plane. Slightly less stable adsorption was found on an atop site (~79 kJ/mol) with the C=C axis oriented along (100) with the CH$_2$ group tilted at 17° from the surface, in reasonable agreement with the energies measured here (Fig. 4.3.3). Work by Bernardo and Gomez found a bridge-site adsorption energy of 81 kJ/mol with a CH$_2$ group tilted about 35° from the surface [39], close to the results found by Ge [38], but found a much lower atop-site adsorption energy of ~32 kJ/mol with a CH$_2$ group tilted ~19° from the surface plane. More recent work, that also examined ethylene adsorption on Au/Pd(100) alloys, gave a heat of adsorption for bridge sites of 90 kJ/mol and 78 kJ/mol on atop sites [40]. Calculations for π-bonded ethylene on Au/Pd(100) alloy clusters yield a binding energy of ~54 kJ/mol with a tilt angle of ~8.4°. Thus, while there

59

is a variation in calculated binding energies for π-bonded ethylene on atop palladium sites, the calculated values are in general agreement with the experimental results (Fig. 4.3.3).

In the intermediate coverage regime of Θ_{Pd} from 0.35 to ~0.65 ML (Θ_{Au} from 0.65 to ~0.35 ML), the number of isolated palladium sites decreases and the number of Pd–Pd bridge sites increases. This results in an increase in the binding energy of the most strongly bound ethylene from ~66 to 80 kJ/mol (Fig. 4.3.3). This is accompanied by the appearance of infrared peaks at ~953 (Fig. 4.3.4D) and ~942 cm^{-1} (Figure 4.3.5A), which disappear on heating to ~200 K, indicating that they are due to remaining π-bonded ethylene. With a gold coverage of 0.57 ML (Fig. 4.3.4D), an additional feature is also evident at ~922 cm^{-1}, which persist on heating to 253 K, and at a gold coverage of 0.4 ML (Fig. 4.3.5A), the peak initially appears at ~908 cm^{-1} and shifts to ~918 cm^{-1}, consistent with a decrease in σ-π parameter, suggesting more strongly bound species on Pd–Pd bridge sites.

For gold coverages lower than ~0.13 ML ($\Theta_{Pd} > 0.27$ ML), a new mode appears at ~1120 cm^{-1}, along with a peak at ~900 cm^{-1} (Figs. 4.3.5C and D). The low-coverage TPD profile is similar to that found for ethylene on Pd(100) [20], which desorbs in two states at 235 and 295 K (at a heating rate of 15 K/s), similar to the TPD data for an Au/Pd(100) alloy with low gold coverage (Fig. 4.3.1D). An ethylene vibrational frequency ~1120 cm^{-1} is suggestive of the presence of di-σ-bonded ethylene [37] with a σ-π parameter of ~0.85 [22], and modes assigned to di-σ-bonded ethylene have been detected at similar frequencies on Ni(111) (1088 cm^{-1} [41]), Ru(100) (1130 cm^{-1} [41]) and Pt(111) (1047 cm^{-1} [42]). These peaks are accompanied by a weaker feature above 1400 cm^{-1}, not observed here. Weak CH$_2$ stretching modes are also found between 2900 and 2950 cm^{-1}, and a very weak mode is detected at ~2912 cm^{-1} when the ~1120 cm^{-1} is present (Figs. 4.3.5 C and D). The peaks at ~1120 and ~906 cm^{-1} are clearly associated

60

with different surface species since they disappear at different annealing temperatures; heating causes the ~1120 cm^{-1} feature to disappear between ~228 and 264 K, while the ~906 cm^{-1} peak persists. Further insights into the nature of the surface species giving rise to the ~1120 cm^{-1} mode come from DFT calculations of ethylene and vinyl species on Au/Pd(100) alloys [26]. They yield a binding energy for π-bonded ethylene of ~54 kJ/mol, in good agreement with the desorption data (Fig. 4.3.3) and the frequencies of the most intense CH_2 wagging modes are at ~900 and 922 cm^{-1} (Figs. 4.3.4D and 4.3.5A). The calculations also find a strongly bound vinyl species (with a binding energy of ~184 kJ/mol) on an alloy with non-contiguous palladium atoms surrounded by gold. The calculated vibrational frequencies show that the strongest model has an in-plane rocking frequency of ~1154 cm^{-1}, suggesting that the 1120 cm^{-1} mode should be assigned to a vinyl species. A similar frequency (~1160 cm^{-1}) has been reported for vinyl on Ni(100) [43].

It has been suggested that the reactive ensemble on model gold-palladium (100) model vinyl acetate synthesis catalysts comprise neighboring Pd–Pd sites [3]. DFT calculations suggest that vinyl species are stable on a surface containing this ensemble while vibrational frequencies consistent with the presence of vinyl species are detected on alloys with relatively low gold coverages. This raises the possibility that VAM formation could occur on these alloy surface *via* the Moiseev pathway from the direct coupling between vinyl and acetate species. However, the vinyl species decompose below the temperatures at which VAM synthesis is carried out, while adsorbed ethylene is stable, implying the VAM formation on Au/Pd(100) alloys is most likely to occur *via* the Samanos pathway as found on Au/Pd(111) alloys.

4.5 Conclusions

61

The heat of ethylene adsorbed on Au/Pd(100) model alloys increases with the palladium content in the alloy from ~ 33 kJ/mol for a completely gold-covered surface, to ~80 kJ/mol as the gold coverage decreases to zero. The most rapid change in adsorption energy, from ~33 to ~65 kJ/mol, is found for palladium coverages between 0 and ~0.35 monolayers when the surface is covered by isolated palladium sites, with the heat of adsorption varying much more slowly at higher coverages. This is accompanied by an increase in the ethylene σ-π parameter.

A vibrational mode is found at ~1120 cm^{-1} for gold coverages below ~0.2 monolayers which is assigned to the formation of vinyl species on the surface. The feature disappears on heating to ~250 K indicating that it has decomposed at this temperature. While the presence of vinyl species suggests that vinyl acetate monomer formation could occur through a Moiseev pathway involving a direct coupling between adsorbed vinyl and acetate species, its decomposition at such low temperatures indicates that it is not sufficiently stable to react, implying the VAM formation on Au/Pd(100) alloys is most likely to proceed *via* a Samanos pathway.

4.6 References

[1] W.T. Tysoe, G.L. Nyberg, R.M. Lambert, Structural, kinetic, and reactive properties of the palladium(111)-ethylene system, J. Phys. Chem., 88 (1984) 1960-1963.

[2] L.P. Wang, W.T. Tysoe, R.M. Ormerod, R.M. Lambert, H. Hoffmann, F. Zaera, Determination of the bonding and orientation of ethylene on palladium (111) by near-edge x-ray absorption fine structure and photoelectron spectroscopy, J. Phys. Chem., 94 (1990) 4236-4239.

[3] C.H. Patterson, R.M. Lambert, Molecular Pathways in the Cyclotrimerization of Ethyne on Palladium – Role of the C-4 Intermediate, Journal of the American Chemical Society, 110 (1988) 6871-6877.

[4] C.H. Patterson, R.M. Lambert, Molecular Mechanisms in the Cyclotrimerization of Acetylene to Benzene on Palladium, J. Phys. Chem., J. Phys. Chem., 92 (1988) 1266-1270.

[5] C.H. Patterson, J.M. Mundenar, P.Y. Timbrell, A.J. Gellman, R.M. Lambert, Molecular Pathwys in the Cyclotrimerization fo Acetylene on Pd(111) – Vibrational Spectra of the C4H4 Intermediates and its Thermal-Decompsition Products, Surface Science, 208 (1989) 93-112.

[6] C.J. Baddeley, M. Tikhov, C. Hardacre, J.R. Lomas, R.M. Lambert, Ensemble Effects in the Coupling of Acetylene to Benzene on a Bimetallic Surface: A Study with Pd{111}/Au, J. Phys. Chem., 100 (1996) 2189-2194.

[7] R. Haley, M. Tikhov, R. Lambert, The Surface Chemistry of Acetic Acid on Pd{111}, Catal Lett, 76 (2001) 125-130.

[8] B. Samanos, P. Boutry, R. Montarnal, The mechanism of vinyl acetate formation by gas-phase catalytic ethylene acetoxidation, Journal of Catalysis, 23 (1971) 19-30.

[9] D. Stacchiola, F. Calaza, L. Burkholder, W.T. Tysoe, Vinyl acetate formation by the reaction of ethylene with acetate species on oxygen-covered Pd(111), Journal of the American Chemical Society, 126 (2004) 15384-15385.

[10] D. Stacchiola, F. Calaza, L. Burkholder, A.W. Schwabacher, M. Neurock, W.T. Tysoe, Elucidation of the Reaction Mechanism for the Palladium-Catalyzed Synthesis of Vinyl Acetate, Angewandte Chemie International Edition, 44 (2005) 4572-4574.

[11] M. Chen, D. Kumar, C.-W. Yi, D.W. Goodman, The Promotional Effect of Gold in Catalysis by Palladium-Gold, Science, 310 (2005) 291-293.

[12] M.S. Chen, K. Luo, T. Wei, Z. Yan, D. Kumar, C.W. Yi, D.W. Goodman, The nature of the active site for vinyl acetate synthesis over Pd-Au, Catalysis Today, 117 (2006) 37-45.

[13] D. Kumar, M.S. Chen, D.W. Goodman, Synthesis of vinyl acetate on Pd-based catalysts, Catalysis Today, 123 (2007) 77-85.

[14] P. Han, S. Axnanda, I. Lyubinetsky, D.W. Goodman, Atomic-Scale Assembly of a Heterogeneous Catalytic Site, Journal of the American Chemical Society, 129 (2007) 14355-14361.

[15] F. Calaza, D. Stacchiola, M. Neurock, W.T. Tysoe, Coverage Effects on the Palladium-Catalyzed Synthesis of Vinyl Acetate: Comparison between Theory and Experiment, Journal of the American Chemical Society, 132 (2010) 2202-2207.

[16] F. Calaza, M. Mahapatra, M. Neurock, W.T. Tysoe, Disentangling ensemble, electronic and coverage effects on alloy catalysts: Vinyl acetate synthesis on Au/Pd(1 1 1), Journal of Catalysis, 312 (2014) 37-45.

[17] F. Calaza, D. Stacchiola, M. Neurock, W.T. Tysoe, Kinetic Parameters for the Elementary Steps in the Palladium-Catalyzed Synthesis of Vinyl Acetate, Catal Lett, 138 (2010) 135-142.

[18] D. Stacchiola, W.T. Tysoe, The Kinetics of Ethylidyne Formation from Ethylene on Pd(111), The Journal of Physical Chemistry C, 113 (2009) 8000-8001.

[19] J.A. Boscoboinik, F.C. Calaza, M.T. Garvey, W.T. Tysoe, Identification of Adsorption Ensembles on Bimetallic Alloys, J. Phys. Chem. C, 114 (2010) 1875-1880.

[20] E.M. Stuve, R.J. Madix, Bonding and dehydrogenation of ethylene on palladium metal. Vibrational spectra and temperature-programmed reaction studies on palladium(100), Surface Science, 89 (1985) 105-112.

[21] E.M. Stuve, R.J. Madix, C.R. Brundle, The adsorption and reaction of ethylene on clean and oxygen covered Pd(100), Surface Science, 152–153, Part 1 (1985) 532-542.

[22] E.M. Stuve, R.J. Madix, Use of the π-σ parameter for characterization of rehybridization upon adsorption on metal surfaces, J. Phys. Chem., 89 (1985) 3183-3185.

[23] I.I. Moiseev, M.N. Vargaftik, Izr. Akad. Nauk. SSSR, Engl. Transl., 133 (1960).

[24] I.I. Moiseev, M.N. Vargaftik, Perspectives in Catalysis, Chemistry for the 21st Century, Blackwell Scientific Oxford, 1992.

[25] E.G. Allison, G.C. Bond, The Structure and Catalytic Properties of Palladium-Silver and Palladium-Gold Alloys, Catal. Rev., 7 (1972) 233-289.

[26] I. Rivalta, G. Mazzone, N. Russo, E. Sicilia, Adsorption of Ethylene, Vinyl, Acetic Acid, and Acetate Species on PdAu(111) and PdAu(100) Surface Alloys: A Cluster Model Study, J. Chem. Theory Comput., 5 (2009) 1350-1360.

[27] D. Mei, E.W. Hansen, M. Neurock, Ethylene Hydrogenation over Bimetallic Pd/Au(111) Surfaces: Application of Quantum Chemical Results and Dynamic Monte Carlo Simulation, J. Phys. Chem. B, 107 (2003) 798-810.

[28] F.C. Calaza, F. Gao, Z. Li, W.T. Tysoe, The adsorption of ethylene on Au/Pd(111) alloy surfaces, Surface Science, 601 (2007) 714-722.

[29] J.A. Boscoboinik, C. Plaisance, M. Neurock, W.T. Tysoe, Monte Carlo and density functional theory analysis of the distribution of gold and palladium atoms on Au/Pd(111) alloys, Phys. Rev. B, 77 (2008) 714-722.

[30] M. Garvey, J.A. Boscoboinik, L. Burkholder, J. Walker, C. Plaisance, M. Neurock, W.T. Tysoe, The Structure of the Au/Pd(100) Alloy Surface, Journal of Physical Chemistry C, 116 (2011) 6.

[31] M. Kaltchev, A.W. Thompson, W.T. Tysoe, Reflection-absorption infrared spectroscopy of ethylene on palladium (111) at high pressure, Surface Science, 391 (1997) 145-149.

[32] Z. Li, F. Gao, W.T. Tysoe, Surface chemistry of acetic acid on clean and oxygen-covered Pd(111), Surface Science, 602 (2008) 416-423.

[33] W.J. Wytenberg, R.M. Lambert, A Long-Lived Aluminium Evaporation Source for Controlled, Reproducible Deposition of Clean Ultra-Thin Films under UHV Conditions, Journal of Vacuum Science and Technology A, 10 (1992) 2.

[34] P.A. Redhead, Thermal desorption of gases, Vacuum, 12 (1962) 9.

[35] R.G. Greenler, Infrared Study of Adsorbed Molecules on Metal Surfaces by Reflection Techniques, The Journal of Chemical Physics, 44 (1966) 310-315.

[36] Z. Li, F. Gao, O. Furlong, W.T. Tysoe, Adsorption of carbon monoxide on Au/Pd(100) alloys in ultrahigh vacuum: Identification of adsorption sites, Surface Science, 604 (2010) 136-143.

[37] D. Stacchiola, L. Burkholder, W.T. Tysoe, Ethylene adsorption on Pd(1 1 1) studied using infrared reflection–absorption spectroscopy, Surface Science, 511 (2002) 215-228.

[38] Q. Ge, M. Neurock, Correlation of adsorption energy with surface structure: ethylene adsorption on Pd surfaces, Chem. Phys. Letts., 358 (2002) 377-382.

[39] C.G.P.M. Bernardo, J.A.N.F. Gomes, The adsorption of ethylene on the (100) surfaces of platinum, palladium, and nickel: a DFT study, J. Mol. Struc.-THEOCHEM, 542 (2001) 263-271.

[40] D. Yuan, X. Gong, R. Wu, Ensemble effects on ethylene dehydrogenation on PdAu(001) surfaces investigated with first-principles calculation and nudged-elastic-band simulations, Phys. Rev. B, 75 (2007) 233401.

[41] E. Cooper, R. Raval, Infrared studies of ethylene adsorption on Ni ⟨111⟩ , Surface Science, 331-333, Part A (1995) 94-99.

[42] J. Fan, M. Trenary, Symmetry and the Surface Infrared Selection Rule for the Determination of the Structure of Molecules on Metal Surfaces, Langmuir, 10 (1994) 3649-3657.

[43] F. Zaera, R.B. Hall, Low temperature decomposition of ethylene over Ni(100): Evidence for vinyl formation, Surface Science, 180 (1987) 1-18.

Chapter 5

Kinetics and Mechanism of Vinyl Acetate Monomer Synthesis on Pd(100) Model Catalysts

5.1 Introduction

Vinyl acetate monomer (VAM) is catalytically synthesized by a reaction between ethylene, acetic acid and oxygen over supported palladium with a selectivity of about 80 % [1, 2]. The mechanism of VAM formation has been extensively studied on Pd(111) [3, 4] and is found to proceed *via* the so-called Samanos pathway [5-7] in which ethylene inserts into an O–Pd bond of the acetate to form an acetoxyethyl intermediate, where the rate-limiting step is the subsequent β-hydride elimination reaction to form VAM [6].

This reaction pathway has also been predicted by DFT calculations [8], which demonstrated that the reactant coverage exerted a profound influence on the elementary-step activation energies; the activation energy for the reaction between adsorbed acetate and ethylene to form the acetoxyethyl intermediate decreased from 103 kJ/mol at a low acetate coverage (Θ=1/9 ML (monolayers)) to 73 kJ/mol at a higher, acetate-saturation coverage (Θ=1/3 ML), while the calculated activation energy for β-hydride elimination increased from +43 kJ/mol at low coverages to +61 kJ/mol at saturation. Thus, the activation energy for the bond-forming coupling reaction decreased with increasing coverage, while the activation energy for the β-hydride elimination, a bond-breaking reaction increased [9].

68

Studies of VAM on clean Pd(111) surfaces in ultrahigh vacuum reveal that it decomposes at temperatures below those at which VAM is synthesized on Pd(111) [10]. However, as the adsorbed acetate species react with ethylene, ethylene also reacts on the vacant palladium sites to form ethylidyne species [11-13], thereby maintaining a high total adsorbate coverage which inhibits VAM decomposition [8].

Gold-palladium alloy catalysts increase the selectivity to VAM formation (to over 90%) and VAM syntheses carried out on single-crystal model alloy catalysts reveal that Au/Pd(100) alloys are particularly active, where it was suggested that the active site on the alloy surface consists of isolated palladium atoms that are surrounded by gold located at opposite corners of a square unit cell on the surface [3]. The elementary-step kinetics of VAM formation have also been studied on Au/Pd(111) alloys. Here, alloy formation changes the rate-limiting step in the Samanos pathway for VAM formation due to a combination of electronic and coverage effects [14]. However, the elementary-step kinetics of VAM formation on the most active Au/Pd(100) surface has not yet been studied. Studies of the chemistry of ethylene on Au/Pd(100) alloys reveal that high gold coverages significantly weaken the ethylene bonding, but the results imply that ethylene can react to form vinyl species on low-gold-coverage alloys [15] as suggested to occur on clean Pd(100) [16, 17]. In this case, the lack of three-fold sites on the surface inhibits the formation of stable ethylidyne species. In addition, a reaction which is initiated by a dehydrogenation reaction (to form a vinyl group) followed by a vinyl-acetate coupling reaction has been proposed by Moiseev [18] suggesting the possibility that reaction could occur by this route on Pd(100), although the barriers for this pathway have been calculated to be much larger than those for the Samanos route on Pd(111) [9].

69

The titration of adsorbed acetate species by gas-phase ethylene has been studied previously on Pd(100) [19] where the rate of acetate removal was found to depend on the initial oxygen coverage, where the fastest reaction was found for the c(2×2)O/Pd(100) surface. However, no VAM was detected spectroscopically on the surface, so that the reaction pathway was not investigated in detail. The following therefore explores the reaction pathway and kinetics on the most active c(2×2)O/Pd(100) surface using reflection-absorption infrared spectroscopy (RAIRS) when acetate-covered surfaces are exposed to gas-phase ethylene. While the energy barriers for the elementary steps are expected to be similar on Pd(100) and Pd(111), there are several important effects of changing the exposed crystal face. First is the lack of ethylidyne formation on Pd(100) referred to above. Second, based on the relative intensities of the acetate infrared features on Pd(111) and Pd(100), the saturation coverage of acetate species is lower on the (100) surface (~0.17 ML) compared to Pd(111), where the saturation acetate coverage is ~0.33 ML. In the case of the titration of acetate species on Pd(111), reaction was initiated by ethylene adsorbing at a small number of defect sites on the surface and the total adsorbate coverage remained high, thereby inhibiting product decomposition. The lower acetate saturation coverage on Pd(100), combined with the lack of ethylidyne formation suggest that there will be greater tendency for reaction products and/or intermediates to decompose during reaction on the (100) surface of palladium than on the (111) face. Furthermore, the decomposition pathways for VAM differ on the two faces. On Pd(111), VAM decomposes to form acetyl and vinyloxy species [10], while on Pd(100), VAM decomposes to reform acetate species and produce CO [20].

5.2 Experimental Methods

70

Infrared data were collected as described previously [5, 21] where the Pd(100) single crystal sample was mounted in a modified 2 ¾" six-way cross, equipped with infrared-transparent, KBr windows, attached to a ultrahigh vacuum (UHV) chamber operating at a base pressure of ~2×10^{-10} Torr following bakeout. The crystal could be resistively heated to 1200 K, or cooled to ~90 K using liquid nitrogen. Samples were prepared by exposing an oxygen-saturated Pd(100) single crystal to acetic acid and then by pressurizing the infrared cell with 1×10^{-4} Torr of C_2H_4. Kinetic data were collected at 4 cm^{-1} resolution, and the collection time was varied according to the reaction rate.

Temperature-programmed desorption (TPD) experiments were carried out in another UHV chamber also operating at a base pressure of ~2×10^{-10} Torr following bakeout, in which the sample could also be cooled to ~90 K using liquid nitrogen. The sample was placed in front of a ~ 1 cm diameter orifice in a shroud enclosing the Dycor quadrupole mass spectrometer, which could sequentially collect desorption profiles for up to 5 masses using a heating rate of 5 K/s.

The Pd(100) sample was cleaned using a standard procedure that consisted of heating to 1000 K in ~4×10^{-8} Torr of oxygen and then annealing at 1200 K *in vacuo* to remove any remaining oxygen.

The C_2H_4 (Matheson, Research Grade), acetic acid (Aldrich, 99.99+ %), C_2D_4 (CIL, 98 % D), 1,1-ethylene-d$_2$ (CIL, 98 % D), 1,2-ethylene-d$_2$ (CIL, 98 % D), and O_2 (Matheson, Research Grade) were transferred to glass bottles, which were attached to a gas-handling line for introduction into the vacuum chamber. The cleanliness of all reactants was monitored mass spectroscopically.

5.3 Results

71

Kinetic measurements were made on a Pd(100) surface with a c(2×2) oxygen overlayer which was then dosed with acetic acid to saturate it with acetate species. The sample was exposed to gas-phase ethylene isotopomers, C_2H_4, C_2D_4 and 1,1- and 1,2-ethylene-d_2 and the infrared spectra were recorded as a function of time [5, 7, 8, 22] to obtain the kinetic data.

5.3.1 Reaction Between Adsorbed Acetate Species and Ethylene on c(2×2)-O/Pd(100)

The reaction of adsorbed acetate species on a c(2×2)-O/Pd(100) surface pressurized with $1×10^{-4}$ Torr of ethylene as a function of time collected at a sample temperature of 234 K are displayed in Fig. 5.3.1.1A, where the times are displayed adjacent to each spectrum. Note that only selected spectra are displayed for clarity. As will be shown below, this ethylene pressure is selected to be sufficiently high that the reaction rate is independent of ethylene pressure and thus reflects the kinetics of the surface reaction. At t = 0, the spectrum initially shows a single intense feature at ~1407 cm^{-1}. Vibrational features at ~1414 cm^{-1} have been assigned to adsorbed acetate species [21, 23] indicating that acetate species are formed on the oxygen-covered Pd(100) surface. The peak absorbance of the acetate feature is ~$2.3×10^{-3}$ absorbance units, which is approximately 50% of the value measured for acetate species on Pd(111) collected using the same apparatus [5], indicating that the acetate coverage on the oxygen-covered Pd(100) surface is ~1/6 ML (monolayer). The infrared spectra evolve as the surface is pressurized with ethylene (Fig. 5.3.1.1A) indicating that a reaction takes place between ethylene and acetate species. In particular, the intensity of the acetate feature (at 1407 cm^{-1}) decreases, and the integrated intensity of the acetate feature is plotted as a function of time, for data collected over finer time

72

intervals, in Fig. 5.3.1.1(C). The line through the data is a fit to a kinetic model, which will be discussed in greater detail below.

Figure 5.3.1.1: (A) A series of infrared spectra for acetate species adsorbed on Pd(100) with a c(2×2) oxygen overlayer pressurized with 1×10^{-4} Torr of gas-phase ethylene as a function of time, where the times are marked adjacent to the corresponding spectrum. Each spectrum was collected at a resolution of 4 cm^{-1} at a sample temperature of 234 K. Note that not all collected spectra are displayed for clarity. (B) Plot of the time dependence of the coverage of carbon monoxide as a function of time taken from the integrated area under the CO absorption peaks (■). (C) Plot of the time dependence of the integrated intensity of the 1407 cm^{-1} (acetate) feature (■) as a function of time. The solid line shows a fit to the data (See text), and the red curve in this figure shows the associated change in CO coverage.

The vibrational frequencies of the surface species participating in the VAM formation reaction have been identified; as discussed above, a mode at ~1414 cm^{-1} is assigned to adsorbed acetate species [21, 23] and a feature at ~1790 cm^{-1} is due to adsorbed VAM [21]. This is generally weak when acetate species are reacted with ethylene on Pd(111), and no features are detected at this frequency on oxygen-coverage Pd(100). The predominant ethylidyne mode occurs at ~1333 cm^{-1} [11-13, 24-26] but does not appear on Pd(100) due to the absence of three-fold hollow sites [16, 17]. The acetoxyethyl intermediate, which would appear at ~1720 cm^{-1} [21], is also not observed and is only detected on Pd(111) when using perdeuterated ethylene [5,

7, 9]. The only detected products as the acetate species are removed exhibit vibrational frequencies at ~ 1892 and 1967 cm^{-1}, similar to the results found previously for the reaction of ethylene with acetate species on oxygen-covered Pd(100) [19]. Carbon monoxide on Pd(111) displays vibrational frequencies between ~1895 and ~1950 cm^{-1} as the CO coverage increases from low coverages to a maximum of ~0.5 ML [27-29].

The shape of the titration curves for acetate species reacting with ethylene on oxygen-covered Pd(100) is quite different from that found previously on Pd(111) [5, 8, 9, 21]. In the case of reaction on Pd(111), the titration curve is sigmoidal in shape, where the rate is initially slow and then accelerates as the surface becomes depleted of acetate species and the adsorbed ethylene coverage increases, while the titration curve for oxygen-covered Pd(100), shown in Fig. 5.3.1.1C, has an approximately exponential decrease in intensity as a function of time. The CO accumulation, measured from the integrated intensity of the CO features (Fig. 5.3.1.1A) is shown in Fig. 5.3.1.1B, and the CO coverage increases as the acetate species are removed from the surface.

Similar experiments were performed at a reaction temperature of 276 K and the results are displayed in Fig. 5.3.1.2A. Again, the acetate species are removed relatively rapidly from the surface and no features are detected that could be assigned either to VAM or an acetoxyethyl intermediate, and only CO is formed. The accumulation of CO as a function of time is shown in Fig. 5.3.1.2B, where the total CO is now significantly larger than for reaction at ~234 K (Fig. 5.3.1.1). The titration curve is displayed in Fig. 5.3.1.2C, along with the CO formation kinetics, and the line through the data is a fit to a kinetics model that will be discussed in greater detail below.

74
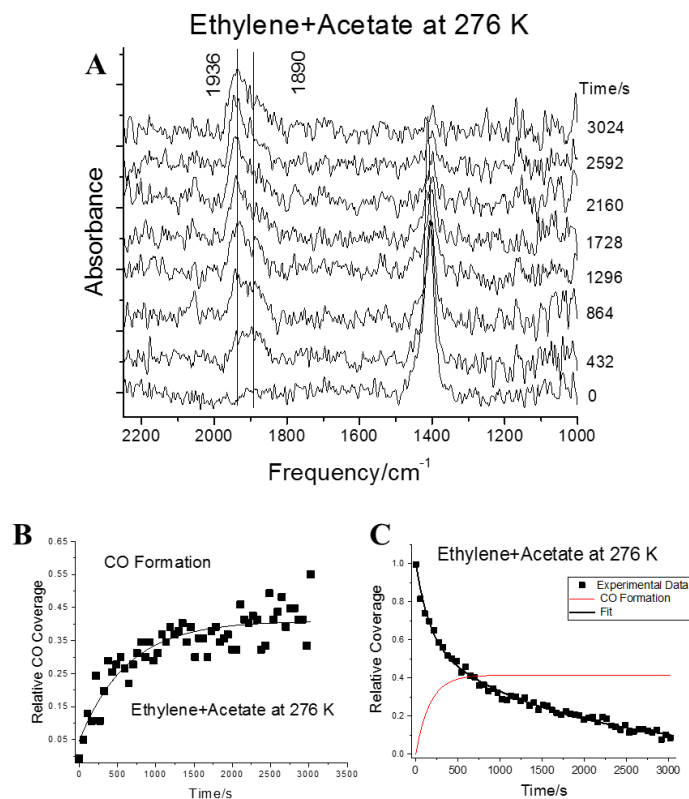
Figure 5.3.1.2: (A) A series of infrared spectra for acetate species adsorbed on Pd(100) with a c(2×2) oxygen overlayer pressurized with 1×10⁻⁴ Torr of gas-phase ethylene as a function of time, where the times are marked adjacent to the corresponding spectrum. Each spectrum was collected at a resolution of 4 cm⁻¹ at a sample temperature of 276 K. Note that not all collected spectra are displayed for clarity. (B) Plot of the time dependence of the coverage of carbon monoxide as a function of time taken from the integrated area under the CO absorption peaks (■). (C) Plot of the time dependence of the integrated intensity of the 1407 cm⁻¹ (acetate) feature (■) as a function of time. The solid line shows a fit to the data (See text), and the red curve in this figure shows the associated change in CO coverage.

In order to compare the reaction rates on oxygen-covered Pd(100) with those measured previously on Pd(111), the rate of acetate removal on oxygen-covered Pd(100) by gas-phase ethylene was measured at a sample temperature of 289 K, similar to the temperature at which the reaction rate was measured on the Pd(111) surface [8] and the results are displayed in Fig. 5.3.1.3. The acetate species (giving rise to the peak at ~1411 cm⁻¹) in the spectra in Fig. 5.3.1.3A now disappear more rapidly than at 276 K (Fig. 5.3.1.2), and again only give rise to additional features at ~1896 cm⁻¹, again indicating that CO is also formed on the surface. Again, Fig.

5.3.1.3B shows a plot of the time-dependent accumulation of carbon monoxide, which now is the predominant product. Indeed, as will be shown below, reaction at 306 K produces exclusively CO. Again, the titration curve is shown in Fig. 5.3.1.3C, along with a fit to the kinetic model.
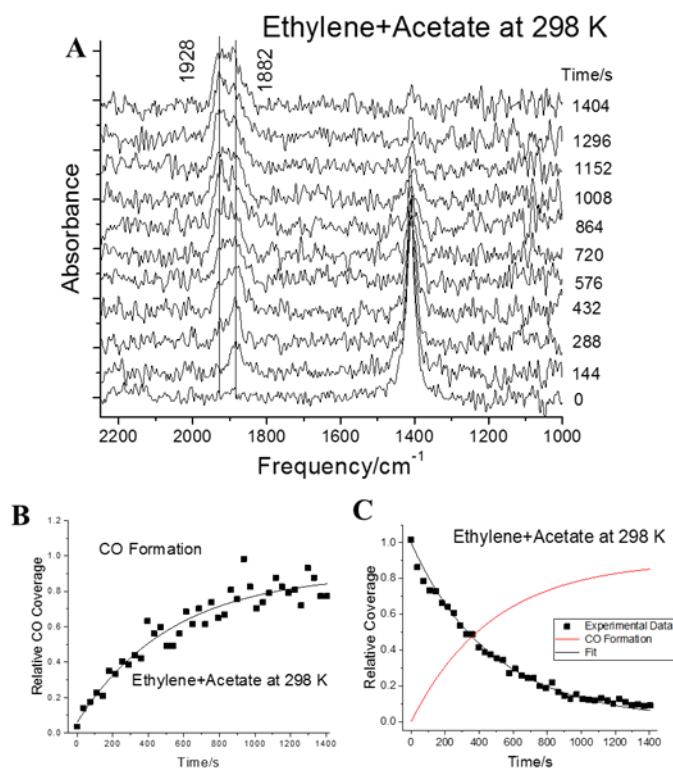
Figure 5.3.1.3: (A) A series of infrared spectra for acetate species adsorbed on Pd(100) with a c(2×2) oxygen overlayer pressurized with 1×10^{-4} Torr of gas-phase ethylene as a function of time, where the times are marked adjacent to the corresponding spectrum. Each spectrum was collected at a resolution of 4 cm^{-1} at a sample temperature of 298 K. Note that not all collected spectra are displayed for clarity. (B) Plot of the time dependence of the coverage of carbon monoxide as a function of time taken from the integrated area under the CO absorption peaks (■). (C) Plot of the time dependence of the integrated intensity of the 1407 cm^{-1} (acetate) feature (■) as a function of time. The solid line shows a fit to the data (See text), and the red curve in this figure shows the associated change in CO coverage.

Fig. 5.3.1.4 shows a plot of the effective rate constant for the removal of acetate species on oxygen-covered Pd(100) as a function of gas-phase ethylene pressure at a constant reaction temperature of 298 K. The solid line is a fit to a simple Langmuir isotherm and indicates that the acetate removal rate is essentially independent of ethylene pressure above $\sim 1 \times 10^{-4}$ Torr.
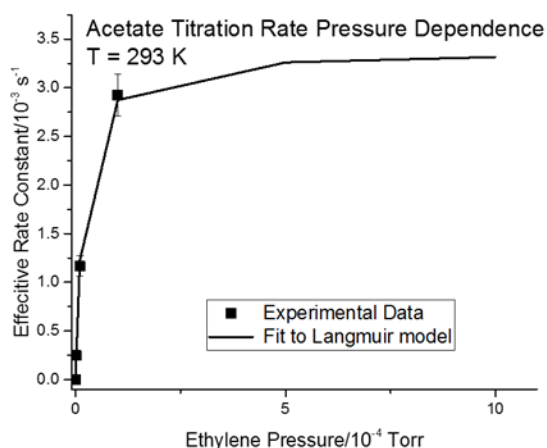
Figure 5.3.1.4: Plot of an effective rate constant for the removal of acetate species from an oxygen-covered Pd(100) surface with a c(2×2) oxygen overlayer with various ethylene pressures of gas-phase C_2H_4 (■). The solid line shows a rate calculated by assuming that the reaction is first order in ethylene pressure and that the ethylene coverage is given by a Langmuir adsorption isotherm.

5.3.2 Reaction Between Adsorbed Acetate Species and d_2- and d_4-Ethylene on c(2×2)-O/Pd(100)

The data collected for C_2H_4 reacting with adsorbed acetate species confirm that acetate species react with gas-phase ethylene but the results give no indication that VAM is formed in the reaction or on the pathways. However, previous work on VAM reactions on Pd(111) revealed an easily measurable primary deuterium isotope effect [21]. Accordingly, reactions were carried out using various ethylene isotopomers. Since C_2D_4 showed significant primary isotope effects on Pd(111), the spectra obtained by reacting 1×10^{-4} Torr of perdeuterated ethylene with acetate species adsorbed on c(2×2)-O/Pd(100) are displayed in Fig. 5.3.2.1.

The spectra at a low reaction temperature of 180 K are shown in Fig. Fig. 5.3.2.1A. At this low temperature, the acetate signal is only slightly attenuated, where the reaction removed ~20% of the initial acetate species. A small amount of CO is formed on the surface giving rise to a small peak at ~1880 cm^{-1}, which could also have contributions from CO adsorbed from the background during the relatively long duration of the experiment. Additional features are evident
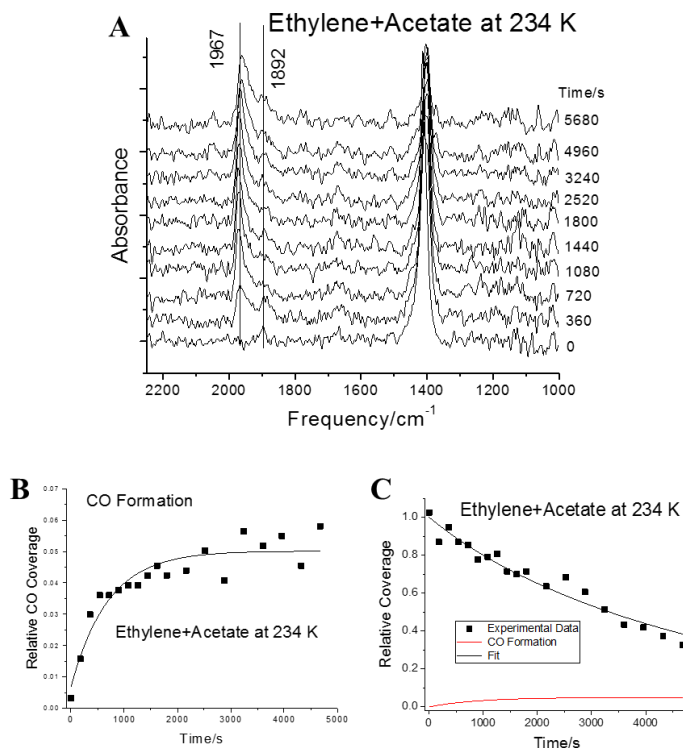
77
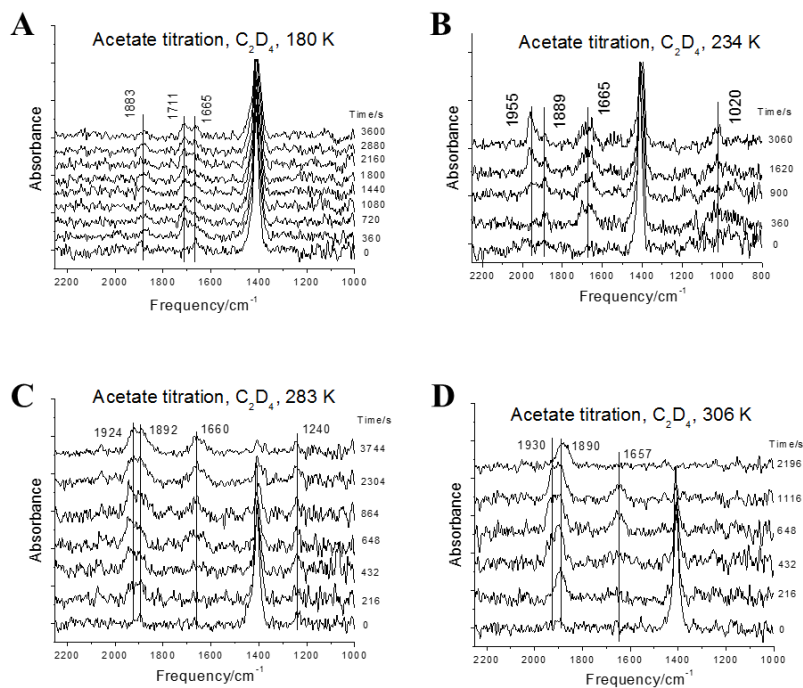
Figure 5.3.2.1: A series of infrared spectra for acetate species adsorbed on Pd(100) with a c(2×2) oxygen overlayer reacting with 1×10^{-4} Torr of gas-phase C_2D_4 at various temperatures as a function of time, where the times are marked adjacent to the corresponding spectrum using reaction temperatures of (A) 180, (B) 234, (C) 283 and (D) 306 K.

at ~1711 and 1665 cm^{-1}, which appear quite quickly after exposure to C_2D_4 and grow slowly thereafter. A feature near ~1715 cm^{-1} has been identified during reaction between ethylene and C_2D_4 on Pd(111) [7] and assigned to an acetoxyethyl intermediate, consistent with VAM being formed in the reaction via the Samanos pathway on oxygen-covered Pd(100).

Carrying out the reaction at ~235 K (Fig. 5.3.2.1B) results in the formation of more CO and the appearance of a ~1665 cm^{-1} peak, with an additional feature at ~1020 cm^{-1} perhaps evident above the background noise. However, there is no feature evident at ~1715 cm^{-1} indicating that the acetoxyethyl intermediate has reacted at this temperature. Further increasing the reaction temperature to ~283 K (Fig. 5.3.2.1C) still results in the presence of the ~1660 cm^{-1} peak. Similar behavior is seen at the reaction temperature increases to ~306 K (Fig. 5.3.2.1D) showing the presence of the ~1660 cm^{-1} peak and perhaps a small feature at ~1240 cm^{-1} peak.

78

After the longest reaction time at ~306 K, the ~1660 cm^{-1} peak disappears to leave only CO on the surface.

The spectra of various ethylene isotopomers reacting with acetate species on c(2×2)-O/Pd(100) at 306 K are compared in Fig. 5.3.2.2. There are now significant differences between the products that are formed for each ethylene isotopomer. The infrared spectra in Fig. 5.3.2.2 also show that reaction of C$_2$H$_4$ and C$_2$D$_4$ with acetate species produces a substantial amount of CO with intense peaks at ~1906 cm^{-1} with C$_2$H$_4$ (Fig. 5.3.2.2A) and at ~1920 cm^{-1} with C$_2$D$_4$ (Fig. 5.3.2.2B). A negligible amount of CO is found when using 1,1-C$_2$H$_2$D$_2$ (Fig. 5.3.2.2C) and some CO is formed when using 1,2-C$_2$H$_2$D$_2$ (Fig. 5.3.2.2D), with a CO stretching frequency of ~1876 cm^{-1}. In addition, as indicated in the data shown in Fig. 5.3.2.1, reaction with C$_2$D$_4$ also produces a feature at ~1650 cm^{-1} that grows with time that is not seen with other isotopomers (Fig. 5.3.2.2).
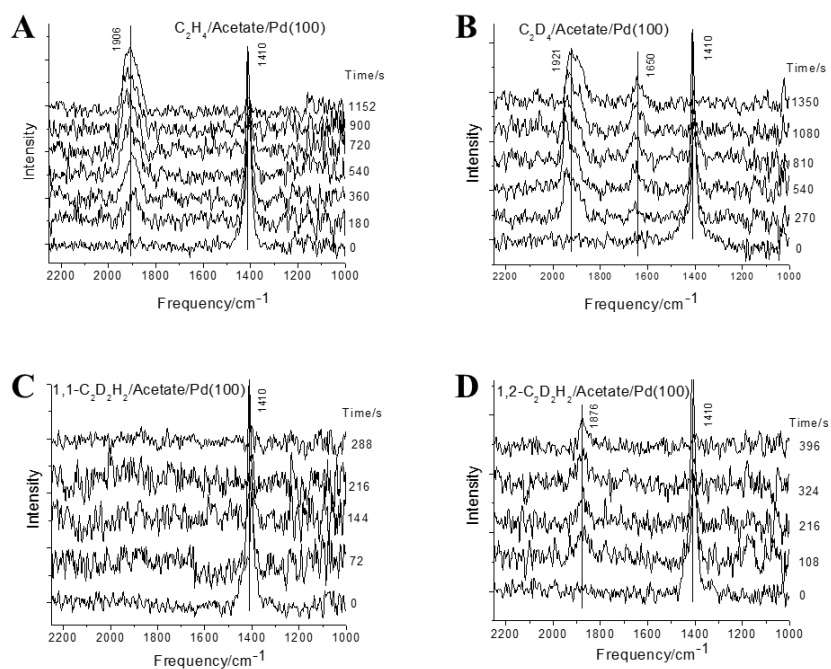
Figure 5.3.2.2: A series of infrared spectra for acetate species adsorbed on Pd(100) with a c(2×2) oxygen overlayer pressurized with 1×10^{-4} Torr of gas-phase ethylene isotopomers as a function of time at a sample temperature of 306 K, where the times are marked adjacent to the corresponding spectrum, when using (A) C$_2$H$_4$, (B) C$_2$D$_4$, (C) 1,1-C$_2$H$_2$D$_2$ and (D) 1,2-C$_2$H$_2$D$_2$.

In all cases, the acetate species react with the ethylene isotopomers and the corresponding titration curves for acetate removal are compared in Fig. 5.3.2.3 for reaction at ~306 K. The rates for C_2D_4 (●) and C_2H_4 (■) are similar, which could imply that the reaction does not exhibit a primary H/D kinetic isotope effect. However, 1,1-ethylene-d_2 (♦) and 1,2-ethylene-d_2 (▲) show similar, but faster rates, implying that hydrogen *is* involved in the reaction between ethylene and acetate species on Pd(100). These results imply that a significant part of the difference between the reaction rates for the ethylene isotopomers is due to the different amounts of CO in the surface when reactions are carried out using C_2H_4 and C_2D_4 compared to 1,2-$C_2H_2D_2$ and 1,1-$C_2H_2D_2$.
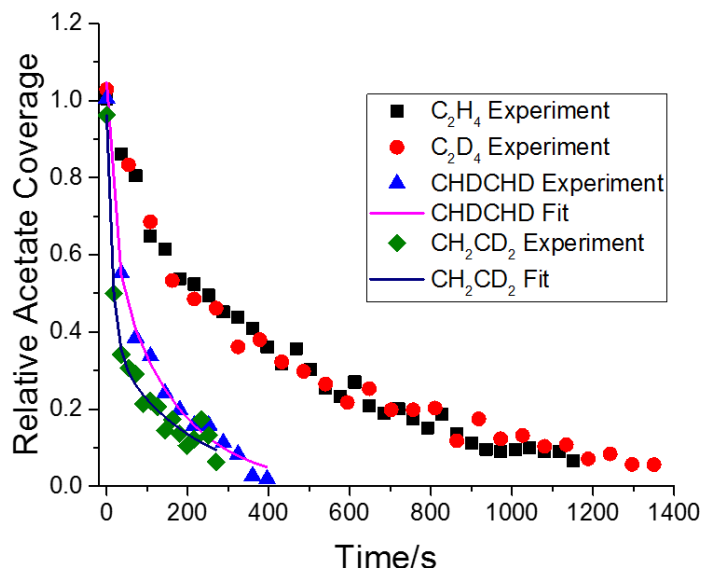
Figure 5.3.2.3: Titration curves comparing the reaction kinetics of various isotopomers of ethylene with acetate species on oxygen-covered Pd(100) for C_2H_4 (■), C_2D_4, (●), 1,2-$C_2H_2D_2$ (▲) and 1,1-$C_2H_2D_2$ (♦), at a sample temperature of 305 K.

5.3.3 Exploration of the CO Formation Pathway from the Reaction of Acetate Species and Ethylene on c(2×2)-O/Pd(100)

The above results indicate that the reaction between gas-phase ethylene and acetate species on c(2×2)-O/Pd(100) differs significantly from that found on the Pd(111) surface; on

80

Pd(111), reaction occurs relatively cleanly with product decomposition being inhibited by the ability of the (111) surface to maintain a high total surface coverage during the course of the reaction. Apparently, the lower initial acetate coverage on Pd(100), as well as the lack of ethylidyne formation allow a much larger extent of decomposition that produces relatively large amounts of CO, especially at higher reaction temperatures (Fig. 5.3.1.1, 5.3.1.2 and 5.3.1.3). There are a number of possible origins for these side reactions. VAM adsorbed on clean and oxygen-covered Pd(100) decomposes to reform acetate species and produce CO. The acetoxyethyl intermediate, which can be trapped by carrying out the reaction at low temperature (~180 K, Fig. 5.3.2.1A), rapidly disappears as the reaction temperature increases (Fig. 5.3.2.1B,
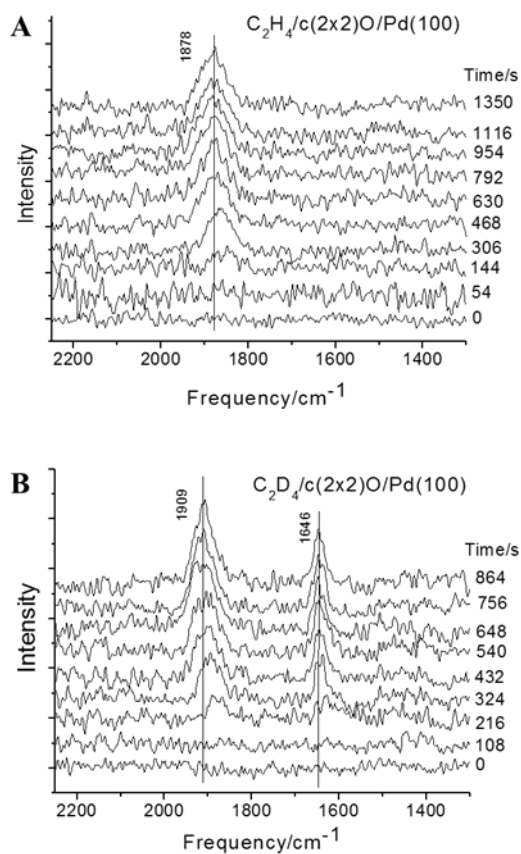
Figure 5.3.3.1: A series of infrared spectra for an oxygen-covered Pd(100) surface with a c(2×2) oxygen overlayer pressurized with 1×10^{-4} Torr of (A) gas-phase C_2H_4 and (B) gas-phase C_2D_4, as a function of time at a sample temperature of 306 K, where the times are marked adjacent to the corresponding spectrum.

81

5.3.2.1C and 5.3.2.1D), suggesting that it might be a possible source for CO formation. Acetate species are relatively stable on Pd(111) and Pd(100) and do not, on their own, form CO. However, ethylene may also react with remaining adsorbed oxygen. In order to explore this, C_2H_4 and C_2D_4 were reacted at 304 K with an oxygen-covered Pd(100) surface in the absence of acetate species and the results are displayed in Fig. 5.3.3.1. The spectra show the growth of a CO feature at ~1880 cm^{-1} when using C_2H_4 and at ~1909 cm^{-1} after reaction with C_2D_4, with the lower frequency implying that slightly more CO is formed from perdeuterated ethylene than with normal ethylene. This indicates that substantial ethylene oxidation takes place and is consistent with kinetic measurements for VAM synthesis on Pd/SiO$_2$ catalysts [30]. In addition, a feature is detected at ~1646 cm^{-1} when using C_2D_4 (Fig. 5.3.3.1B) indicating that this feature, which is also observed in the presence of coadsorbed acetate species (Fig. 5.3.2.1), may originate from a direct reaction with ethylene. This will be explored further below. However, the appearance of this species by reaction with ethylene alone aids in the assignment of this mode. It is clearly stabilized by the presence of deuterium, indicating that its decomposition pathway involves a C–H scission step. However, the observed frequency is below that which would be expected for a vibrational model involving a carbon-oxygen bond [31] and is closer to what might be expected for a C=C bond. This suggests that this mode could be assigned to a vinyloxy group. This has been proposed for VAM decomposition on Pd(111) [10], where the C=C stretching mode occurs at ~1580 cm^{-1}, lower than the frequency found here, but with a C–O stretching frequency of ~1090 cm^{-1} [32-34], close to the value seen for perdeutrated ethylene reaction with acetate species at 234 K (Fig. 5.3.2.1B). In addition, vinyl alcohol has a C=C stretching frequency of ~1628 cm^{-1} [32], close to the value found for C_2D_4 adsorbed on oxygen-covered Pd(100) (Fig. 5.3.3.1B). An alternative possibility is the isomerization of the vinyloxy to form an acetyl species

82

(η^1(C)-(C=O)(CH$_3$)) [33]. This would have the effect of weakening the carbon-carbon bond, thereby facilitating CO formation. Acetyl organometallic complexes with platinum yield an intense CO stretching mode at ~1630 cm^{-1} for a CH$_3$-containing acetyl species, shifting to 1639 cm^{-1} when it is perdeuterated [35]. The corresponding palladium complex exhibits a strong vibrational mode between 1660 and 1675 cm^{-1}, in good agreement with the frequency found for C$_2$D$_4$ on oxygen-covered Pd(100) (Fig. 5.3.3.1B) and during reaction with acetate species (Fig. 5.3.2.2B). This can presumably decompose by C–C bond cleavage or by dehydrogenation. The former pathway yields CO, which has been detected on Pt(111) [33].

However, while plausible, this does not indicate whether the CO is indeed formed by the reaction of ethylene with oxygen remaining on the surface, in particular, since much of it is consumed by acetate formation. In order to further explore this, ethylene was reacted with acetate species that had been formed on an ^{18}O-covered surface. If the CO that is formed is produced by ethylene reacting with oxygen remaining on the surface, the resulting CO should contain the labeled oxygen. The results of this experiment are displayed in Fig. 5.3.3.1, which shows a time sequence of infrared spectra collected for reaction at 306 K. This indicates that the acetate species are removed to form CO as found on the ^{16}O-covered surface. However, the CO stretching frequency is identical to that found on the ^{16}O-covered surface. Fig. 5.3.3.2 also shows the shift that would occur if C^{18}O were adsorbed on the surface. There may be evidence of as small amount of C^{18}O, but the CO predominately contains ^{16}O, indicating that the oxygen derives from the acetate species.
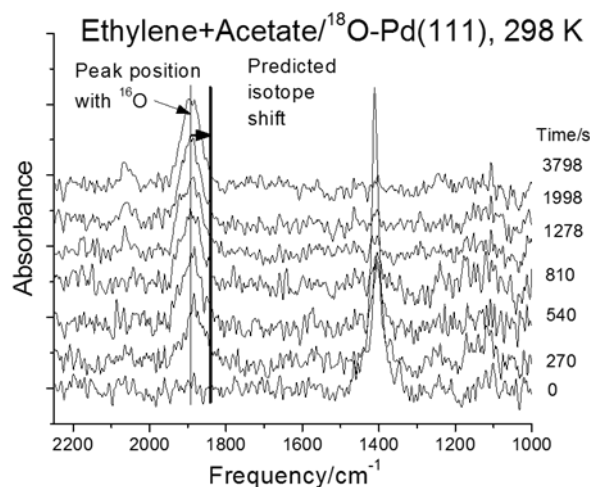
Figure 5.3.3.2: A series of infrared spectra for acetate species adsorbed on oxygen-covered Pd(100) with a c(2×2) ^{18}O overlayer pressurized with $1×10^{-4}$ Torr of gas-phase C_2H_4 as a function of time at a sample temperature of 298 K, where the times are marked adjacent to the corresponding spectrum.

5.4 Discussion

The results presented above clearly show that ethylene reacts with adsorbed acetate species on oxygen-covered Pd(100), although the reaction pathways are less selective than found for acetate species on Pd(111) [5, 8, 9, 21]. In the case of reaction on Pd(111), where the saturation coverage of acetate species is larger than on Pd(100), VAM is selectively formed while the vacant sites are populated as the reaction proceeds by the formation of stable ethylidyne species from ethylene. This was suggested to have several consequences since the repulsive interactions between co-adsorbed species facilitates bond-forming reactions and inhibits bond-breaking ones [7, 36]. First, it lowers the energy barrier for coupling between ethylene and adsorbed acetate species to form the acetoxyethyl intermediate in the so-called Samanos pathway [6], while increasing the barrier for the subsequent β-hydride elimination step [7-9], as well as inhibiting the decomposition of the VAM that is formed on the surface [8]. Lowering the saturation coverage of acetate species on the (111) surface by alloying with gold

84

changes the rate-limiting step for the reaction from the β-hydride elimination step to the coupling step with a consequent loss in deuterium isotope effect [37]. This change occurs at a gold coverage in the alloy of ~0.25 ML (where coverages in this case are referenced to the atom sites density on the (111) surface), corresponding to a decrease in the saturation coverage of acetate species from ~0.33 ML on the clean surface to ~0.25 ML on the alloy.

Since the activation energies calculated for the alternative Moiseev pathway [18] on Pd(111) are significantly higher than for the Samanos pathway on Pd(111) [9], it is anticipated that the reaction should proceed via the same pathway on Pd(100) and the detection of a feature at ~1711 cm^{-1} at ~180 K following the reaction between ethylene and acetate species on Pd(100) (Fig. 5.3.2.1A), assigned to the acetoxyethyl intermediate, indicates that it does. The behavior on Pd(100) can be tentatively predicted based on the observations on the VAM-formation chemistry on Pd(111), primarily due to the effects of the lower acetate coverage on the Pd(100) surface. First, linearly interpolating the energy barriers for the coupling step between ethylene and acetate species and the β-hydride elimination step to estimate the barrier at an acetate coverage of ~1/6 ML suggests a barrier for the coupling step of ~88 kJ/mol and a value of ~52 kJ/mol for β-hydride elimination, and would, at first sight, predict that the initial, coupling step is rate limiting, so that the reaction should not exhibit a primary isotope effect when using C_2D_4. The results in Fig. 5.3.2.3 are consistent with this observation. However, the dideutero isotopomers should therefore also react at the same rate as C_2H_4, while they react more rapidly (Fig. 5.3.2.3). Nevertheless, the low barrier for the subsequent β-hydride elimination step would indicate that any acetoxyethyl intermediate formed on the surface should react relatively rapidly to form VAM and is consistent with the absence of the ~1411 cm^{-1} mode when reacting C_2D_4 with adsorbed acetate species at higher temperatures (Figs. 5.3.2.1A, 5.3.2.1 B, and 5.3.2.1C). A

85

second consequence of the lower acetate coverage on Pd(111) along with the lack of ethylidyne formation on this surface is that products and intermediates formed from acetate-ethylene coupling will be more prone to decompose on the surface. This is clearly evident from the results presented in Figs. 5.3.1.1, 5.3.1.2 and 5.3.1.3, where CO is the major product on the oxygen-covered Pd(111) surface, as observed previously [19].

We first address the possible CO formation pathways. As indicated above, the decomposition reaction seems to involve a vinyloxy or acetyl species. While this can form by direct oxidation of ethylene (Fig. 5.3.3.1), carrying out the reaction with ^{18}O on the surface does not result in the labeled oxygen being included in the CO that is produced. Indeed, the large amount of CO produced on the surface at higher reaction temperatures are unlikely to originate from the pre-adsorbed oxygen, which also react with acetic acid to form acetate species. This, therefore suggests that the vinyloxy includes oxygen that originates from the acetate species and therefore presumably arises from O–C bond scission in either VAM or the acetoxyethyl intermediate. However, VAM decomposes on Pd(100) to reform an acetate species and produce CO [20], while on Pd(111) it decomposes to form a vinyloxy species [10]. Thus, VAM decomposition may also contribute to CO formation, but not to the overall removal to acetate species from the surface, which is found during the reaction on Pd(100) (Figs. 5.3.1.1, 5.3.1.2 and 5.3.1.3). Thus, the acetoxyethyl intermediate is most likely precursor for the CO that is formed. Here, scission of the $(–CH_2–CH_2-O)–(C=O)CH_3)$ bond would yield an acetyl and $CH_2–CH_2-O$ moiety, which could deprotonate to form vinyloxy. In this case, the decomposition of the acetoxyethyl intermediate would be facilitated by deuterium in the β position that would slow the rate of VAM formation. However, the putative vinyloxy intermediate is also stabilized by deuteration (Figs. 5.3.2.1B and 5.3.3.1B) thereby slowing the rate of CO formation. These

86

opposing effects appear to result in relatively similar amounts of CO formation when using C_2H_4 and C_2D_4 (Figs. 5.3.1.1, 5.3.1.2, 5.3.1.3 and 5.3.2.1). Interestingly, reaction with dideuteroethylenes results is less CO being formed (Fig. 5.3.2.2) and a consequently fast rate of acetate removal (Fig. 5.3.2.3) presumably due to the ethylene adsorption not being blocked by CO and thus reacting more quickly. The origin for this effect is not clear.

The titration kinetics can be modeled based on the reaction pathways outline above. The lower initial acetate coverage on Pd(100) allows a significant coverage of ethylene to initially adsorb on the acetate-saturated surface and temperature-programmed desorption experiments comparing ethylene on clean and acetate-saturated Pd(100) suggest that a relative coverage of 0.37 ± 0.03 ML of ethylene adsorbs on acetate-covered Pd(100) compared to the clean surface. The following kinetic analysis is carried out using relative coverages, so that the initial acetate coverage is taken to be unity, and the initial ethylene coverage is Θ_e^0 (= 0.37 ML). It is assumed that the reaction is carried out at sufficiently high ethylene pressures that any vacant sites are occupied by ethylene (Fig. 5.3.1.4) so that:

$$\Theta_e + \Theta_{CO} + \Theta_a = 1 + \Theta_e^0 = \Theta_{tot} \qquad (1),$$

where Θ_e is the ethylene coverage, Θ_{CO} is the CO coverage, Θ_a is the acetate coverage and Θ_{tot} is the total saturation coverage. Similar to previous analyses on Pd(111) [5], the rate of acetate removal is given by:

$$-\frac{d\Theta_a}{dt} = k_1 \Theta_a \Theta_e \qquad (2),$$

where k_1 is the effective rate constant for the coupling reaction. Substituting from Eqn. 1 gives:

$$\frac{d\Theta_a}{dt} + k_1(\Theta_{tot} - \Theta_{CO}) = k_1 \Theta_a^2 \qquad (3).$$

87

The results in Figs. 5.3.1.1, 5.3.1.2 and 5.3.1.3 indicate that the CO coverage increases exponentially and is thus given by: $\Theta_{CO} = \Theta_{CO}^0(1 - \exp(-k_2 t))$, where Θ_{CO}^0 is the maximum amount of CO formed with a rate constant k_2. Substituting into Eqn. 3 yields:

$$\frac{d\Theta_a}{dt} + k_1\left(\Theta_{tot} - \Theta_{CO}^0(1 - \exp(-k_2 t))\right) = k_1\Theta_a^2 \qquad (4).$$

This is a form of the Bernouilli equation [38] with $n = 2$ and can be linearized by putting $\Theta_a(t) = \frac{1}{z(t)}$. This can now be solved analytically using the boundary conditions that $\Theta_a(t = 0) = 1$ to give:

$$\Theta_a(t) = \frac{\exp(-\alpha t)exp\left(\frac{\beta}{k_2}e^{-k_2 t}\right)}{k_1\alpha t + \left(\frac{\beta}{k_2}\right)(e^{-k_2 t} - 1) + exp\left(\frac{\beta}{k_2}\right)} \qquad (5)$$

where $\alpha = k_1(\Theta_{tot} - \Theta_{CO}^0)$ and $\beta = k_1\Theta_{CO}^0$. In order to minimize the total number of fitting parameters, the value of Θ_e was constrained to be ~0.37 ML, and the values of k_2 were taken from separate fits to the variation in CO coverage (see for example Figs. 5.3.1.1B, 5.3.1.2B and 5.3.1.3B). Examples of the resulting fits to the data are shown in Figs. 5.3.1.1C, 5.3.1.2C and 5.3.1.3C, where the fits for results collected at other reaction temperatures were equally good. As evident from the plot in Fig. 5.3.1.3C for reaction at ~298 K, reaction with acetate species results predominantly in the formation of CO suggesting that the decomposition of the acetoxyethyl intermediate dominates the reaction at higher temperatures. An Arrhenius plot of k_1 is displayed in Fig. 5.4.1 and is linear with a slope yielding an effective activation energy of 32 ± 5 kJ/mol, significantly lower than the value of ~55 kJ/mol found for acetate titration by ethylene on Pd(111) [8].
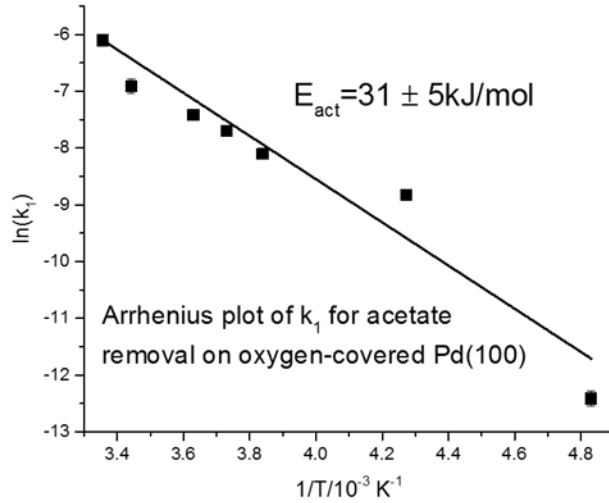
Figure 5.4.1: Arrhenius plot of the rate constant k_1 for the reaction between ethylene and acetate species on oxygen-covered Pd(100).

An effective rate constant for the Samanos pathway can be derived using the elementary step rate constants shown in Scheme 1, assuming that the coupling step is reversible so that:

Scheme 1: Depiction of the reactions occurring on the surface during titration of acetate species by ethylene in the Samanos pathway.
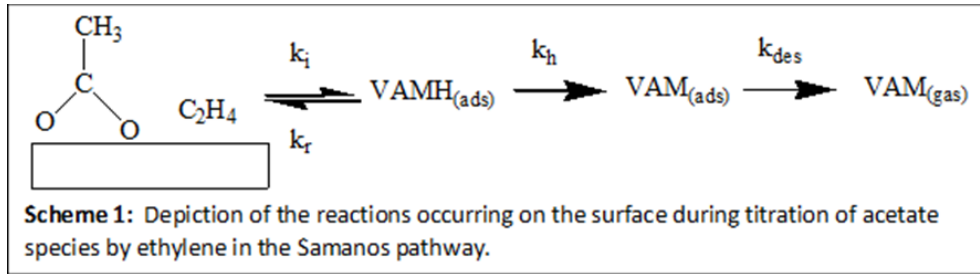
$$-\frac{d\Theta_a}{dt} = k_i \Theta_a \Theta_a - k_r \Theta_{VAMH} \qquad (6)$$

where Θ_{VAMH} is the coverage of the acetoxyetyl intermediate. The rate of formation of the acetoxyethyl intermediate is also given by:

$$\frac{d\Theta_{VAMH}}{dt} = k_i \Theta_a \Theta_a - k_r \Theta_{VAMH} - k_h \Theta_{VAMH} \qquad (7).$$

The coverage of the acetoxyethyl intermediate is assumed to be in steady state to give:

$$\Theta_{VAMH} = \frac{k_i}{(k_r + k_h)} \Theta_a \Theta_e \qquad (8).$$

Substituting into Eqn. 6 gives an effective rate constant for acetate removal, k_1 equal to:

$$k_1 = k_i \left(1 - \left(1 + \frac{k_h}{k_r}\right)^{-1}\right) \qquad (9).$$

89

In the case of VAM formation on Pd(111), the β-hydride elimination step is rate limiting, so that $k_h \ll k_r$. Expanding $\left(1 + \frac{k_h}{k_r}\right)^{-1}$ as a Taylor series to first order gives:

$$k_1 = \frac{k_i k_h}{k_r} \qquad (10),$$

and yields good agreement with the experimentally measured barrier [8, 9]. Correspondingly, if k_h is large, $k_1 = k_h$. A similar analysis, but now including a step involving decomposition of the acetoxyethyl intermediate to CO with rate constants k_{CO} gives:

$$k_1 = k_i \left(1 - \left(1 + \frac{k_h + k_{CO}}{k_r}\right)^{-1}\right) \qquad (11).$$

The data in Fig. 5.4.1 indicates that the rate constant occurs with a relatively low activation barrier of 31 ± 5 kJ/mol, compared with an apparent barrier of ~55 kJ/mol for acetate titration on Pd(111). This implies that the coupling reaction is not rate limiting otherwise, based on the results for Pd(111), the activation barrier should be ~88 kJ/mol, in which case, Eqn. 11 can be rewritten as:

$$k_1 = \frac{k_i (k_h + k_{CO})}{k_r} \qquad (12).$$

This suggests that a combination of co-adsorbed CO and ethylene can provide a sufficiently crowded surface to lower the barrier for ethylene-acetate coupling, but not to inhibit acetoxyethyl intermediate decomposition. In this case, the activation barrier for the overall reaction would depend on whether k_h or k_{CO} limited the overall reaction. The data in Figs. 5.3.1.2 and 5.3.1.3 suggest that CO formation dominates at most reaction temperatures included in the Arrhenius plot, implying that CO formation dominates the overall kinetics, and would result in no isotope effect. If it is assumed that the activation barriers for k_i and k_r are similar on Pd(111) and Pd(100) would suggest that the barrier for acetoxyethyl decomposition to form CO on Pd(111) is ~40 kJ/mol.

90

The reaction between ethylene and adsorbed acetate species on Pd(100) results in a much less selective initial reaction than on the Pd(111) surface. The significant amount of CO formed in the reaction, in particular at higher reaction temperatures, is in contrast to results found for model single crystal alloy catalysts under catalytic conditions, where the (100) face of the model catalyst with a palladium coverage of unity was higher than the (111) face [3]. However, spectroscopic studies of a Pd(100) single crystal model catalysis after reaction at high pressures [39] reveal the presence of a large amount of carbon including significant carbon monoxide. A possible explanation for the apparent lack of selectivity in the initial stages of the reaction on Pd(100) is that relatively strongly bound CO accumulates on the surface to eventually produce a crowded surface under high-pressure reaction conditions that inhibits the decomposition of the intermediate and an improvement in selectivity and reactivity.

5.5 Conclusions

The reaction between gas-phase ethylene and acetate species adsorbed on a Pd(100) surface with a c(2×2) oxygen overlayer is compared with previous analogous experiments on Pd(111). The relatively high acetate coverage on Pd(111) of ~0.33 ML, as well the ability of ethylene to react to form stable ethylidyne species on this surface maintains a crowded surface that influences both the elementary-step reaction rates and prevents product decomposition to yield high selectivities. In contrast, the saturation coverage of acetate species on oxygen-covered Pd(100) is much lower than that on Pd(111), and the lack of three-fold hollow sites suppresses ethylidyne formation. This is expected to result in a much lower selectivity for the reaction on the Pd(100) surface and this is borne out experimentally, where large amounts of carbon

91

monoxide are detected, with the selectivity to CO formation approaching ~100% for reactions carried out above ~300 K.

However, reacting adsorbed acetate species with C_2D_4 at ~180 K results in the appearance of a feature at ~1711 cm^{-1}, previously assigned to an acetoxy ethyl intermediate on Pd(111). This indicates that acetate reacts directly with ethylene on both surfaces to form an acetoxyethyl intermediate and thus proceeds by a pathway proposed by Samanos. However, carrying out the reaction at slightly higher temperature does not result in the detection of the acetoxy ethyl intermediate suggesting that it is unstable on the less crowded Pd(100) surface, implying that the decomposition of this intermediate leads the formation of non-selective products. A kinetic model is developed that incorporates tis non-selective pathways that shows good agreement with the experiment titration curves.

5.6 References

[1] P.M. Colling, L.R. Johnson, I. Nicolau, Palladium-gold catalyst for vinyl acetate production, in: U.S.P. Office (Ed.), Hoechst Celanese Corporation, United States, 1996.

[2] L. Horning, F. Wunder, T. Quadflieg, Process for Preparing Vinyl Acetates, in:

F.H.A.V.M.L. Bruning (Ed.), United States, 1967.

[3] M. Chen, D. Kumar, C.-W. Yi, D.W. Goodman, The Promotional Effect of Gold in Catalysis by Palladium-Gold, Science, 310 (2005) 291-293.

[4] Y.F. Han, D. Kumar, D.W. Goodman, Particle size effects in vinyl acetate synthesis over Pd/SiO2, Journal of Catalysis, 230 (2005) 353-358.

[5] D. Stacchiola, F. Calaza, L. Burkholder, W.T. Tysoe, Vinyl Acetate Formation by the Reaction of Ethylene with Acetate Species on Oxygen-Covered Pd(111), J. Am. Chem. Soc., 126 (2004) 15384-15385.

[6] B. Samanos, P. Boutry, R. Montarnal, The mechanism of vinyl acetate formation by gas-phase catalytic ethylene acetoxidation, Journal of Catalysis, 23 (1971) 19-30.

[7] D. Stacchiola, F. Calaza, L. Burkholder, A.W. Schwabacher, M. Neurock, W.T. Tysoe, Elucidation of the Reaction Mechanism for the Palladium-Catalyzed Synthesis of Vinyl Acetate, Angewandte Chemie International Edition, 44 (2005) 4572-4574.

[8] F. Calaza, D. Stacchiola, M. Neurock, W.T. Tysoe, Kinetic Parameters for the Elementary Steps in the Palladium-Catalyzed Synthesis of Vinyl Acetate, Catal Lett, 138 (2010) 135-142.

[9] F. Calaza, D. Stacchiola, M. Neurock, W.T. Tysoe, Coverage Effects on the Palladium-Catalyzed Synthesis of Vinyl Acetate: Comparison between Theory and Experiment, Journal of the American Chemical Society, 132 (2010) 2202-2207.

[10] F. Calaza, D. Stacchiola, M. Neurock, W.T. Tysoe, Structure and decomposition pathways of vinyl acetate on Pd(111), Surface Science, 598 (2005) 263-275.

[11] L.L. Kesmodel, L.H. Dubois, G.A. Somorjai, Dynamical LEED study of C2H2 and C2H4 chemisorption on Pt(111): evidence for the ethylidyne group, Chemical Physics Letters, 56 (1978) 267-271.

[12] D. Stacchiola, W.T. Tysoe, The Kinetics of Ethylidyne Formation from Ethylene on Pd(111), The Journal of Physical Chemistry C, 113 (2009) 8000-8001.

[13] L.V. Moskaleva, Z.-X. Chen, H.A. Aleksandrov, A.B. Mohammed, Q. Sun, N. Rösch, Ethylene Conversion to Ethylidyne over Pd(111): Revisiting the Mechanism with First-Principles Calculations, The Journal of Physical Chemistry C, 113 (2009) 2512-2520.

[14] F. Calaza, M. Mahapatra, M. Neurock, W.T. Tysoe, Disentangling ensemble, electronic and coverage effects on alloy catalysts: Vinyl acetate synthesis on Au/Pd(1 1 1), Journal of Catalysis, 312 (2014) 37-45.

[15] Z. Li, T. Thuening, W.T. Tysoe, The adsorption of ethylene on Au/Pd(100) alloy surfaces, Surface Science.

[16] E.M. Stuve, R.J. Madix, C.R. Brundle, The adsorption and reaction of ethylene on clean and oxygen covered Pd(100), Surface Science, 152–153, Part 1 (1985) 532-542.

[17] E.M. Stuve, R.J. Madix, Bonding and dehydrogenation of ethylene on palladium metal. Vibrational spectra and temperature-programed reaction studies on palladium(100), The Journal of Physical Chemistry, 89 (1985) 105-112.

[18] I.I. Moiseev, M.N. Vargaftik, Perspectives in Catalysis, Chemistry for the 21st Century, Blackwell Scientific, Oxford, 1992.

[19] F. Calaza, Z.J. Li, W.T. Tysoe, Reaction Between Ethylene and Acetate Species on Clean and Oxygen-Covered Pd(100): Implications for the Vinyl Acetate Monomer Formation Pathway, Catal Lett, 141 (2011) 266-270.

[20] Z. Li, F. Calaza, C. Plaisance, M. Neurock, W.T. Tysoe, Structure and Decomposition Pathways of Vinyl Acetate on Clean and Oxygen-Covered Pd(100), The Journal of Physical Chemistry C, 113 (2009) 971-978.

[21] D. Stacchiola, F. Calaza, L. Burkholder, A.W. Schwabacher, M. Neurock, W.T. Tysoe, Elucidation of the reaction mechanism for the palladium-catalyzed synthesis of vinyl acetate, Angew. Chem.-Int. Edit., 44 (2005) 4572-4574.

[22] F. Calaza, Z. Li, M. Garvey, M. Neurock, W. Tysoe, Reactivity and Selectivity in the Au/Pd(111) Alloy-Catalyzed Vinyl Acetate Synthesis, Catal Lett, 143 (2013) 756-762.

94

[23] J. James, D.K. Saldin, T. Zheng, W.T. Tysoe, D.S. Sholl, Structure and binding site of acetate on Pd(1 1 1) determined using density functional theory and low energy electron diffraction, Catalysis Today, 105 (2005) 74-77.

[24] R.J. Koestner, M.A. Van Hove, G.A. Somorjai, Molecular structure of hydrocarbon monolayers on metal surfaces, The Journal of Physical Chemistry, 87 (1983) 203-213.

[25] P.S. Cremer, X. Su, Y.R. Shen, G.A. Somorjai, Ethylene Hydrogenation on Pt(111) Monitored in Situ at High Pressures Using Sum Frequency Generation, Journal of the American Chemical Society, 118 (1996) 2942-2949.

[26] F. Zaera, G.A. Somorjai, Hydrogenation of ethylene over platinum (111) single-crystal surfaces, Journal of the American Chemical Society, 106 (1984) 2288-2293.

[27] A.M. Bradshaw, F.M. Hoffmann, The chemisorption of carbon monoxide on palladium single crystal surfaces: IR spectroscopic evidence for localised site adsorption, Surface Science, 72 (1978) 513-535.

[28] A. Ortega, F.M. Huffman, A.M. Bradshaw, The adsorption of CO on Pd(100) studied by IR reflection absorption spectroscopy, Surface Science, 119 (1982) 79-94.

[29] J. Szanyi, W.K. Kuhn, D.W. Goodman, CO adsorption on Pd(111) and Pd(100): Low and high pressure correlations, Journal of Vacuum Science & Technology A, 11 (1993) 1969-1974.

[30] Y.F. Han, D. Kumar, C. Sivadinarayana, D.W. Goodman, Kinetics of ethylene combustion in the synthesis of vinyl acetate over a Pd/SiO2 catalyst, Journal of Catalysis, 224 (2004) 60-68.

[31] N.B.D.L.H.W.S.E. Colthup, Introduction to infrared and Raman spectroscopy, Academic Press, N.Y.

[32] M. Hawkins, L. Andrews, Reactions of atomic oxygen with ethene in solid argon. The infrared spectrum of vinyl alcohol, Journal of the American Chemical Society, 105 (1983) 2523-2530.

[33] G.E. Mitchell, P.L. Radloff, C.M. Greenlief, M.A. Henderson, J.M. White, The surface chemistry of ketene on Pt(111) II. HREELS, Surface Science, 183 (1987) 403-426.

[34] M.A. Henderson, P.L. Radloff, J.M. White, C.A. Mims, Surface chemistry of ketene on ruthenium(001). 1. Surface structures, The Journal of Physical Chemistry, 92 (1988) 4111-4119.

[35] D.M. Adams, G. Booth, 206. Infrared spectra of acetyl complexes of platinum and palladium, Journal of the Chemical Society (Resumed), (1962) 1112-1116.

[36] R.A.v. Santen, M. Neurock, S.G. Shetty, Reactivity Theory of Transition-Metal Surfaces: A Brønsted−Evans−Polanyi Linear Activation Energy−Free-Energy Analysis, Chemical Reviews, 110 (2009) 2005-2048.

[37] F. Calaza, M. Mahapatra, M. Neurock, W.T. Tysoe, Disentangling ensemble, electronic and coverage effects on alloy catalysts: Vinyl acetate synthesis on Au/Pd(1 1 1), Journal of Catalysis, 312 (2014) 37-45.

[38] D. Zwillinger, Handbook of differential equations, Academic Press, San Diego, Calif., 1998.

[39] D. Kumar, Y.-F. Han, M.S. Chen, D.W. Goodman, Kinetic and Spectroscopic Studies of Vinyl Acetate SynthesisOver Pd(100), Catal Lett, 106 (2006) 1-5.

Chapter 6

Vinyl Acetate Formation on Au/Pd(100) Alloy Surfaces

6.1 Introduction

The synthesis of vinyl acetate monomer (VAM) by a reaction between ethylene, acetic acid and oxygen is catalyzed both by supported palladium and palladium-gold alloys, where alloying with gold leads to a substantial increase in selectivity from ~85% for pure palladium to approximately 92% for the alloy [1, 2]. The reaction mechanism has been extensively studied on Pd(111) [3, 4] where it is found to proceed *via* the so-called Samanos pathway [5-7] in which ethylene inserts into an O–Pd bond of an η^2-acetate to form an acetoxyethyl-palladium intermediate, and the rate-limiting step is the subsequent β-hydride elimination reaction to form VAM [6].

This reaction has also been studied using DFT calculations [8], which demonstrated that the reactant coverage has a profound influence on the elementary-step activation energies; the activation energy for the reaction between adsorbed acetate and ethylene to form the acetoxyethyl intermediate decreases from 103 kJ/mol at a low acetate coverage (Θ=1/9 ML (monolayers)) to 73 kJ/mol at a higher, acetate-saturation coverage (Θ=1/3 ML), while the calculated activation energy for β-hydride elimination increased from +43 kJ/mol at low coverages to +61 kJ/mol at saturation. Thus, the activation energy for the bond-forming coupling reaction decreased with increasing coverage, while the activation energy for the β-hydride

elimination, a bond-breaking reaction increased [9]. In addition, it is found that VAM decomposes on Pd(111) at temperatures below that at which the VAM-formation reaction proceeds [10], but the formation of ethylidyne species from ethylene [11-13] maintains a high total adsorbate coverage, which stabilizes the VAM that is formed, thereby improving the reaction selectivity [8]. Mechanistic studies on model Au/Pd(111) alloys shows that alloying induces a change in the rate-limiting step in the Samanos pathway for VAM formation due to a combination of electronic, ensemble and coverage effects [14].

High-pressure reactor studies of VAM syntheses using model single-crystal catalysts reveal that Au/Pd(100) alloys are particularly active, and it was suggested that the active site on the alloy surface consists of isolated palladium atoms that are surrounded by gold atoms located at opposite corners of a square unit cell on the surface [3]. However, the lack of three-fold sites on Pd(100) prevent ethylidyne formation, thus excluding the possibility that VAM decomposition is inhibited by surface crowding as found on the (111) surfaces. Indeed, recent studies have shown that the selectivity to VAM formation on clean Pd(100) is relatively low and results in the formation of substantial amounts of CO [15, 16]. Accordingly, the mechanism of VAM formation is studied on Au/Pd(100) alloys here to explore the effects of alloying on both the reactivity and selectivity of VAM formation

The structures of Au/Pd(100) alloy surfaces are different from those of Au/Pd(111) [17, 18]. There are weak nearest-neighbor interactions between the gold and palladium on Au/Pd(111) that result in an almost random gold and palladium distribution [17, 18]. However, much longer-range interactions are found on Au/Pd(100) alloys resulting in the appearance of ordered structures, in particular a c(2×2) structure for a palladium coverage of ~0.5 monolayers (ML) [19]. As a consequence, there are no isolated palladium sites (without palladium nearest

98

للاستشارات

neighbors) on Au/Pd(100) alloys for gold coverages below ~0.35 ML (see Fig. 6.4.1).

The surface chemistry of the reactants and products has been studied on Au/Pd(100) alloys. High gold coverages significantly weaken the ethylene bonding on Au/Pd(100) alloys [20] compared to clean Pd(100) [21, 22]. In addition, the VAM decomposition pathways on Pd(100) differ from that on Pd(111), where VAM decomposes to form acetyl and vinyloxy species [10], while on Pd(100), VAM decomposes to reform acetate species and produce CO [23]. VAM adsorbs on Au/Pd(100) alloys that have gold coverages greater than ~0.5 ML in a flat-lying geometry and desorb with an activation energy of ~55 kJ/mol with only a small proportion decomposing, while at lower gold coverages, VAM adsorbs via a rehybridized vinyl group [24]. This work also reveals that adsorbed VAM is significantly stabilized on alloys with high gold coverages. Acetic acid forms η^2-acetate species on Au/Pd(100) alloys at lower gold coverages, where the acetate is stabilized as the gold coverage increases [25]. This implies that higher coverages of gold on the Au/Pd(100) alloy should serve to stabilize any VAM that is formed.

6.2 Experimental Methods

Infrared data were collected as described previously [5, 26] where a Au/Pd(100) single crystal sample was mounted in a modified 2 ¾" six-way cross, equipped with infrared-transparent, KBr windows, attached to a ultrahigh vacuum (UHV) chamber operating at a base pressure of ~2×10^{-10} Torr following bakeout. The crystal could be resistively heated to 1200 K, or cooled to ~90 K using liquid nitrogen.

Temperature-programmed desorption (TPD) experiments were carried out in another UHV chamber also operating at a base pressure of ~2×10^{-10} Torr following bakeout, which could

99

also be cooled to ~90 K using liquid nitrogen. The sample was placed in front of a ~ 1 cm diameter orifice in a shroud enclosing the Dycor quadrupole mass spectrometer, which could sequentially collect desorption profile at up to 5 masses using a heating rate of 5 K/s.

A Pd(100) single crystal was cleaned using a standard procedure that consisted of heating to 1000 K in ~4×10^{-8} Torr of oxygen and then annealing at 1200 K *in vacuo* to remove any remaining oxygen, and its cleanliness monitored using Auger spectroscopy and TPD collected following oxygen adsorption [27]. Gold was evaporated from a small alumina tube furnace [28], which enabled controlled and reproducible evaporation rates to be achieved. In order to precisely control the temperature of the gold, and therefore its evaporation rate, a C-type thermocouple was placed into the gold pellet. The gold palladium alloy was formed by initially depositing five monolayers of gold on the Pd(100) substrate, which was then annealed to various temperatures for a period of five minutes in ultrahigh vacuum to produce the desired alloy composition [19].

Samples were first prepared for reaction by creating oxygen-saturated Au/Pd(100) alloy single crystal surfaces. Saturated oxygen overlayers were obtained by exposing alloys with gold coverages below 0.5 ML to 20 L O$_2$, which was sufficient to saturate the surface and form a c(2×2) structure on Pd(100) [29]. For alloys with gold coverages above 0.5 ML, ozone was used as an atomic oxygen source, as described elsewhere [30, 31], because O$_2$ does not dissociate on alloys without Pd–Pd dimer sites. After oxygen preadsorption, acetic acid was introduced into the reaction cell to form an acetate-saturated surface, and was subsequently pressurized in the infrared cell, generally with 1×10^{-4} Torr of C$_2$H$_4$. Kinetic data were collected by sequentially obtaining infrared spectra at 4 cm^{-1} resolution, and the collection time was varied according to the reaction rate. In some cases, reactions were carried out using 2 Torr of ethylene. Here, the strong gas-phase ethylene infrared signal precluded the reaction being followed while the

100

reaction cell was pressurized. In this case, infrared spectra were collected after the cell had been evacuated.

The C_2H_4 (Matheson, Research Grade), acetic acid (Aldrich, 99.99+ %), and O_2 (Matheson, Research Grade) were transferred to glass bottles, which were attached to a gas-handling line for introduction into the vacuum chamber. The cleanliness of all reactants was monitored mass spectroscopically.

6.3 Results

Because of the difference in available ensembles for gold coverage above and below ~0.5 ML, and the correspondingly different reactivities, the results obtained for the two gold coverage regimes will be discussed separately. Fig. 6.3.1 displays results for the reaction of acetate-saturated Au/Pd(100) alloys that were pressurized with 1×10^{-4} Torr of ethylene with a sample temperature of 306 K, which plots the evolution in the infrared spectra as a function of time, where the times are displayed adjacent to the corresponding spectrum. In all the experiments described below, the ethylene was introduced into the reaction cell through a dosing tube directed towards the sample, and pressures were measured in the adjacent vacuum chamber so that local pressures will be larger than this value. It has also been found that this ethylene pressure is sufficiently high for the reaction to be zero order in ethylene pressure on clean Pd(100) [16]. Acetic acid reacts rapidly on both clean Pd(100) (Fig. 6.3.1A) and Au/Pd(100) alloys with gold coverages up to 0.38 ML (Figs. 6.3.1B, $\Theta_{Au} = 0.11$ ML, C $\Theta_{Au} = 0.22$ ML, and D $\Theta_{Au} = 0.38$ ML) to form η^2 acetate species with a characteristic vibrational signature at ~1405 cm^{-1} [16]. The spectra for clean Pd(100) are included for reference since the selectivity to VAM formation is zero on this surface at this reaction temperature; all the VAM that is produced by

the reaction decomposes to CO [16], as evidenced by the large CO infrared signals at between ~1885 and 1917 cm^{-1} [32]. In all cases, the acetate species react with gas-phase ethylene, but the time required to completely remove the acetate species decreases with increasing gold coverage (up to a maximum of 0.38 ML). In addition, the amount of carbon monoxide that is produced by the reaction decreases as the gold content in the alloy increases.
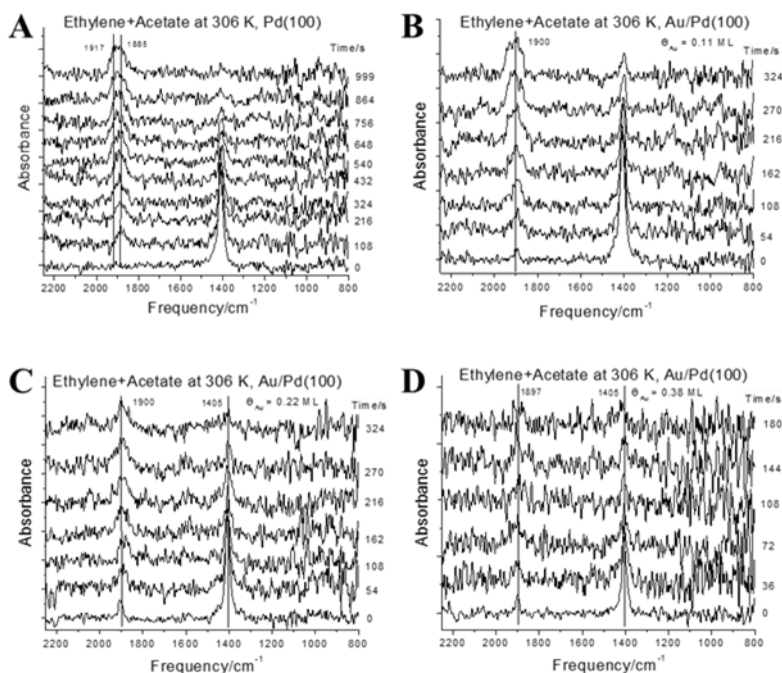
Figure 6.3.1: A series of infrared spectra for acetate species adsorbed on a series of Au/Pd(100) alloys pressurized with 1×10^{-4} Torr of gas-phase ethylene as a function of time, where the times are marked adjacent to the corresponding spectrum. Each spectrum was collected at a resolution of 4 cm^{-1} at a sample temperature of 306 K. Note that not all collected spectra are displayed for clarity. Shown in (A) are the spectra for acetate species adsorbed on Pd(100) with a c(2×2) oxygen overlayer. The remaining figures show the infrared spectra for alloys with (B) 0.11, (C) 0.22 and (D) 0.38 ML of gold in the Au/Pd(100) alloy.

Kinetic measurements were also made using identical reaction conditions, but with the sample held at 260 K. The results are shown in Fig. 6.3.2 (A $\Theta_{Au} = 0.11$ ML, B $\Theta_{Au} = 0.22$ ML, and C $\Theta_{Au} = 0.38$ ML). Again, in all cases, adsorbed acetate species react with gas-phase ethylene, but now at lower rates compared to the results collected at 306 K (Fig. 6.3.1). Carbon monoxide is still the predominate reaction product, evidenced by infrared features between ~1900 and ~1950 cm^{-1}, with an additional feature at ~2060 cm^{-1} due to CO adsorbed on gold-containing sites [29]. This is not detected during reaction at 306 K, because CO adsorbed on

102
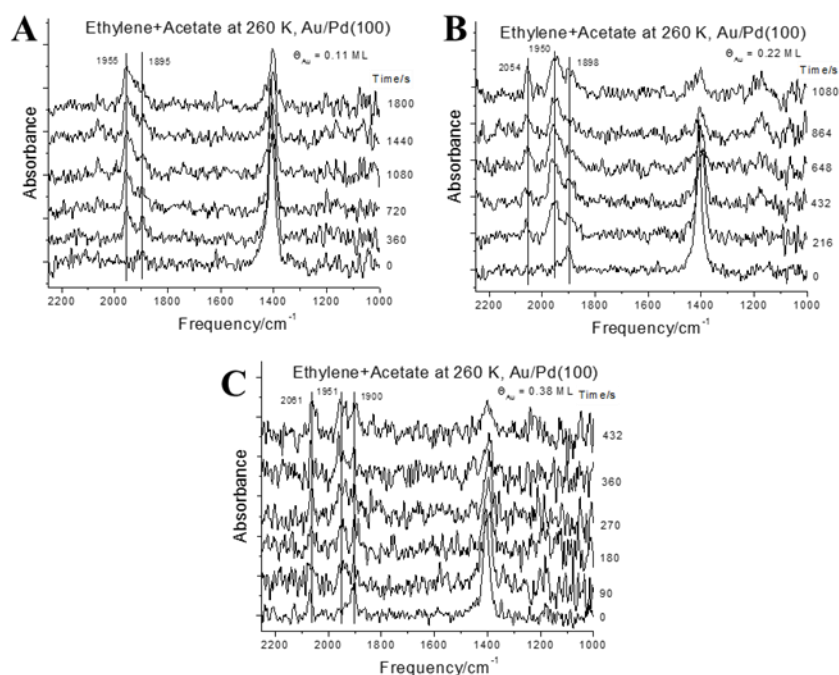
Figure 6.3.2: A series of infrared spectra for acetate species adsorbed on a series of Au/Pd(100) alloys pressurized with 1×10^{-4} Torr of gas-phase ethylene as a function of time, where the times are marked adjacent to the corresponding spectrum. Each spectrum was collected at a resolution of 4 cm^{-1} at a sample temperature of 260 K for alloys with (A) 0.11, (B) 0.22 and (C) 0.38 ML of gold in the Au/Pd(100) alloy. Note that not all collected spectra are displayed for clarity.

these sites has desorbed by this temperature. No clear additional features are observed, in particular peaks at ~1718 cm^{-1} that would indicate the presence of an acetoxyethyl-palladium intermediate [7] that would provide evidence for the reaction proceeding via the Samanos pathway.

We now show results for Au/Pd(100) alloys with higher gold coverages (of 0.66, 0.79 and 0.87 ML). Note that these alloys are of particular interest because they were found to be the most catalytically active of all model alloy surfaces [3]. The results are displayed in Fig. 6.3.3 for reaction at 306 K, using identical conditions as for the low-gold-coverage alloys above. It is clear that the nature of the initial acetic-acid derived species is different from that at lower alloy coverages and consists of broad features, the with most intense peak centered at ~1450 cm^{-1}, with a less intense peak at ~1590 cm^{-1}, with evidence of a weak peak at ~1414 cm^{-1}. Similar features have been detected previously on Au/Pd(100) alloys with gold coverages above ~0.5

103
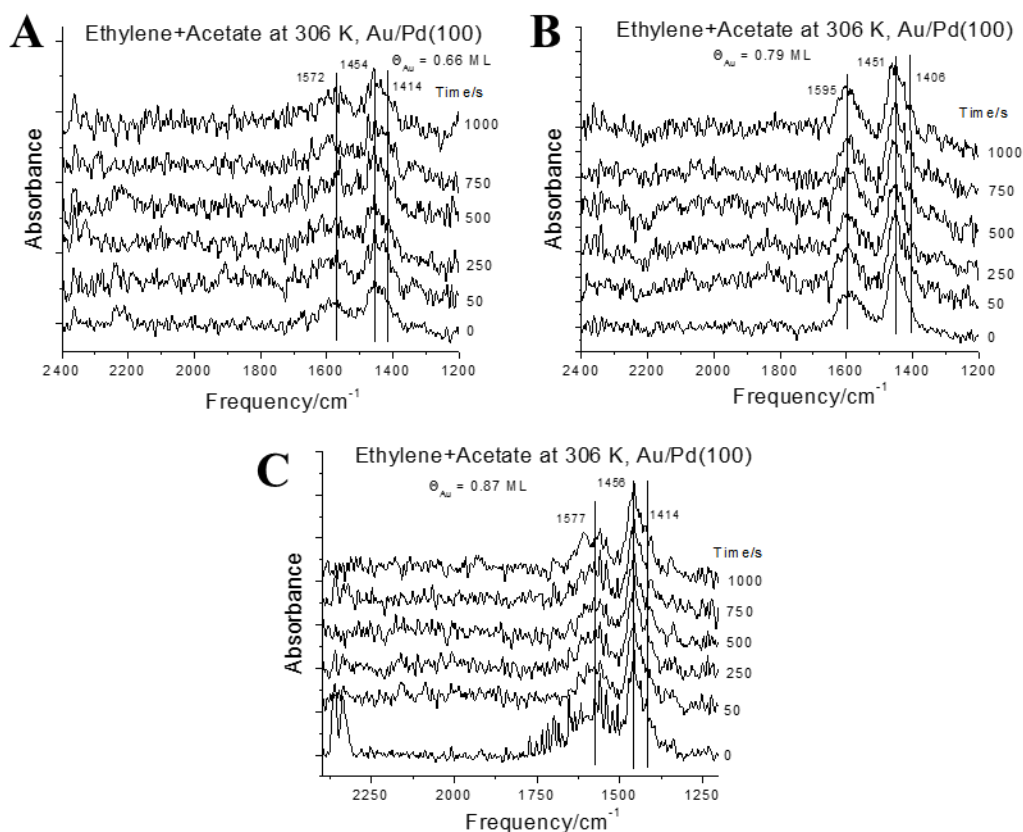
Figure 6.3.3: A series of infrared spectra for acetate species adsorbed on a series of Au/Pd(100) alloys pressurized with 1×10^{-4} Torr of gas-phase ethylene as a function of time, where the times are marked adjacent to the corresponding spectrum. Each spectrum was collected at a resolution of 4 cm^{-1} at a sample temperature of 306 K for alloys with (A) 0.66, (B) 0.79 and (C) 0.87 ML of gold in the Au/Pd(100) alloy. Note that not all collected spectra are displayed for clarity.

ML [25], where acetic acid was adsorbed at ~90 K and the sample heated and resulted in the appearance of features at 1591 and 1478 cm^{-1}, with a shoulder at ~1419 cm^{-1}. These surfaces were then pressurized by 1×10^{-4} Torr of gas-phase ethylene. However, there is no evident change in the intensity of these features even after ~1000 s reaction time, indicating that the acetic-acid derived species on the surface for alloy coverages greater than ~0.5 ML are much less reactive than those found for alloys with lower gold coverages (Figs. 6.3.1 and 6.3.2).

To further explore the reactivity of these acetic-acid derived species, a Au/Pd(100) alloy with 0.87 ML of gold that had been exposed to acetic acid was pressurized by 2 Torr of ethylene for 360 s. The large infrared signal due to gas-phase ethylene prohibits the surface infrared spectrum from being collected while the sample is being pressurize. However, the results shown

104
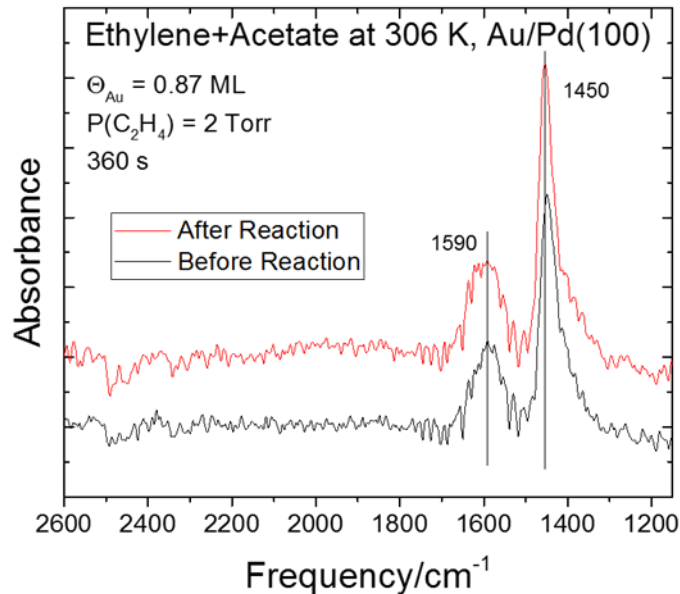
Figure 6.3.4: Infrared spectra of an Au/Pd(100) alloy with 0.87 ML of gold before exposure to gas-phase ethylene (Bottom spectrum), and after pressurizing with 2 Torr of ethylene for 360s at 306 K (Top spectrum).

in Fig. 6.3.4 reveal that there is no change in the infrared spectra even after exposure to high ethylene pressures. However, the longer spectral detection times show clear features at ~1590 and 1450 cm^{-1}.

In order to confirm that these infrared species are due to acetic-acid derived species on the alloys, rather than being due to decompositions products, TPD profiles were obtained while detecting various masses for high-gold-coverage alloys saturated with acetic acid. The results are displayed in Fig. 6.3.5 collected by monitoring signals at 60 (Fig. 6.3.5A) and 43 (Fig. 6.3.5B) amu, because they are the most intense mass spectrometer fragmentation masses of acetic acid. Similar profiles are found when monitoring 29 and 44 amu with relative intensities that are in good agreement with the mass spectrometer ionizer fragmentation pattern of acetic acid. All spectra show a broad feature centered at ~450 K. In order to confirm that the adsorbed species that gives rise to the infrared peaks seen in Figs. 6.3.3 and 6.3.4 react by evolving acetic acid on heating, the variation in the integrated intensities of the infrared features are plotted versus

105

www.manaraa.com
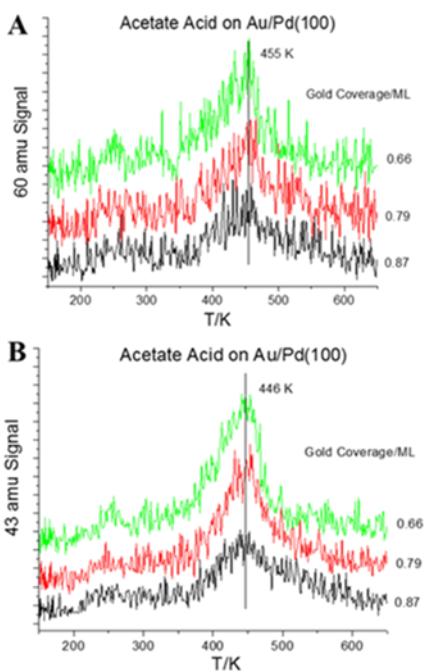
Figure 6.3.5: Temperature-programmed desorption spectra of various Au/Pd(100) alloys with high gold coverages, where the gold coverages are marked adjacent to the corresponding spectra, saturated with acetic acid, collected by monitoring (A) 60 and (B) 43 amu signals with a heating rate of 5 K/s.

annealing temperature and the results are displayed in Fig. 6.3.6, where signals decrease in intensity over the same temperature range as which acetic acid is detected in TPD (Fig. 6.3.5).
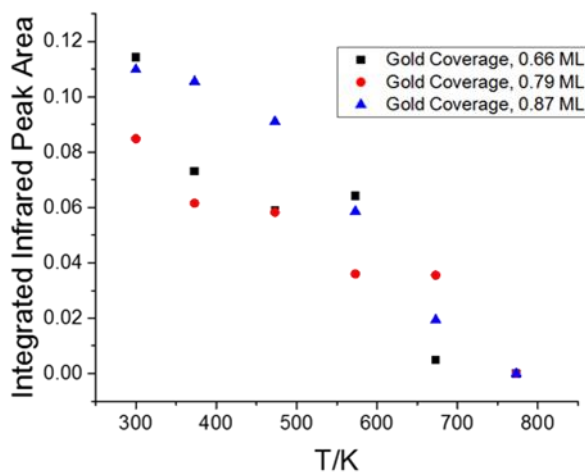
Figure 6.3.6: Plot of the integrated peak areas for the infrared spectra of a saturated overlayer of acetic acid on various Au/Pd(100) alloys with high gold coverages, plotted as a function of annealing temperature, for alloys with 0.66 (■), 0.79 (●), and 0.87 (▲) ML of gold.

106

6.4 Discussion

Because of the relatively strong interactions between gold and palladium on Au/Pd(100) alloys, the surface exhibits ordered structures that result in large variations in the nature of the available surface sites on alloy with gold coverage [33]. This is illustrated in Fig. 6.4.1, which shows the relative coverage of isolated palladium (red line) and palladium bridge sites (black line) as a function of the gold coverage in the alloy. For gold coverages below ~0.38 ML, the alloy surface is dominated by palladium bridge sites, allowing the formation of η^2 acetate species that give rise to a characteristic acetate vibrational mode at ~1414 cm^{-1} [16]. However, higher gold coverages result in a reduction in the palladium bridge site coverage and an increase in the number of isolated palladium sites, which further decrease at higher gold coverages. As a consequence, reactions with Au/Pd(100) alloys with gold coverages below ~0.4 ML are discussed first since they contain bridge sites, which form reactive bidentate acetate species on the surface and the ~1405 cm^{-1} feature, due to a $\nu_a(COO)$ mode. The decrease in intensity of this
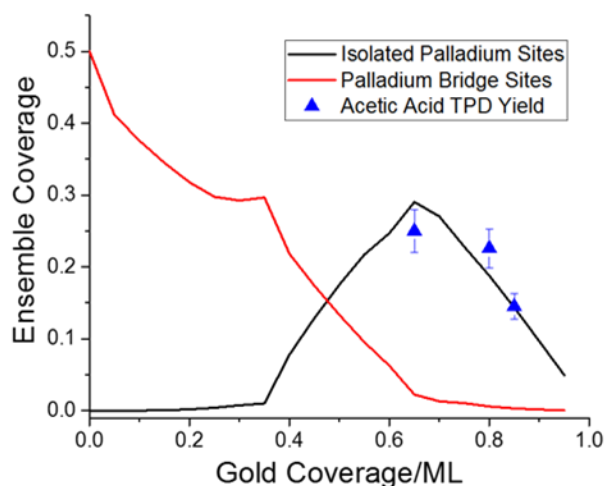
Figure 6.4.1: Plot of the coverage of isolated palladium sites (Black line) and palladium bridge sites (Red line) as a function of the gold coverage in Au/Pd(100) alloys, adapted from Reference [33]. Shown also plotted on this curve are the scaled integrated areas of the most intense 43 amu TPD desorption profiles (from Fig. 6.3.5B) are plotted versus gold coverage (▲).

107

vibrational mode as the gold coverage in the alloy increases is shown in Figs. 6.3.1 and 6.3.2 and is expected from the data in Fig. 6.4.1.

Previous work to study the surface chemistry of VAM on Au/Pd(100) alloys reveal that it binds to the surface in a distorted geometry via a rehybridized vinyl group for gold coverages below ~0.5 ML of gold, and exhibits peaks at ~1195, 1316, 1040, 1012 and 887 cm^{-1} [24]. However, no discernable features are detected corresponding to adsorbed VAM because of the relatively high spectral noise in this region due to the small collection times required by the fast reaction rates. In addition, it is found that adsorbed VAM decomposes on heating to reform acetate species and produce adsorbed CO, consistent with the detection of CO in the spectra in Figs. 6.3.1 and 6.3.2. Measurements of the integrated absorbances of the amount of CO on the various alloys relative to that formed on Pd(100) indicate that the CO produced decreases to ~0.86 of that formed on clean Pd(100) on an alloy with a gold coverage on 0.11 ML, to 0.45 ML on an alloy with 0.22 ML of gold, and to 0.13 ML when the gold coverage is 0.38 ML. This is consistent with the decreased reactivity of VAM on Au/Pd(100) alloys as a function of increasing gold coverage [24]. An acetoxyethyl intermediate in the Samanos pathway would appear at ~1720 cm^{-1} [26], is also not observed but is only detected on Pd(111) when using perdeuterated ethylene [5, 7, 9].

Thus, while this work provides no direct mechanistic information on the VAM formation pathway, it has been found that the VAM forms via the Samanos pathway on Pd(111) [7, 9], Au/Pd(111) [14] and on Pd(100) [16]. It is therefore expected that reaction will occur by a similar mechanism on the Au/Pd(100) alloy. This implies that reaction on Au/Pd(100) alloys with lower gold coverages forms VAM via the Samanos pathway, a portion of which, based on the reaction pathway found on Au/Pd(100), decomposes to reform adsorbed acetate species and

108

CO.

The reaction of ethylene with adsorbed acetate on Pd(100) proceeds via the Samanos pathway with relatively low selectivity [16], to produce significant amounts of CO. It has been suggested that CO is also produced on Pd(100) by VAM decomposition and the kinetics were modeled by assuming that adsorption sites are blocked by CO formation and yielded an analytical model for the acetate removal kinetics [16], where the time-dependent acetate coverage $\Theta_a(t)$ is given by:

$$\Theta_a(t) = \frac{\exp(-\alpha t) exp\left(\frac{\beta}{k_2}e^{-k_2 t}\right)}{k_1\alpha t + \left(\frac{\beta}{k_2}\right)(e^{-k_2 t}-1) + exp\left(\frac{\beta}{k_2}\right)} \tag{1}$$

where $\alpha = k_1(\Theta_{tot} - \Theta_{CO}^0)$ and $\beta = k_1\Theta_{CO}^0$. Here, the CO coverage was found to increase exponentially and was thus modeled by: $\Theta_{CO} = \Theta_{CO}^0(1 - \exp(-k_2 t))$, where Θ_{CO}^0 is the maximum amount of CO formed with a rate constant k_2. The rate constant for the coupling
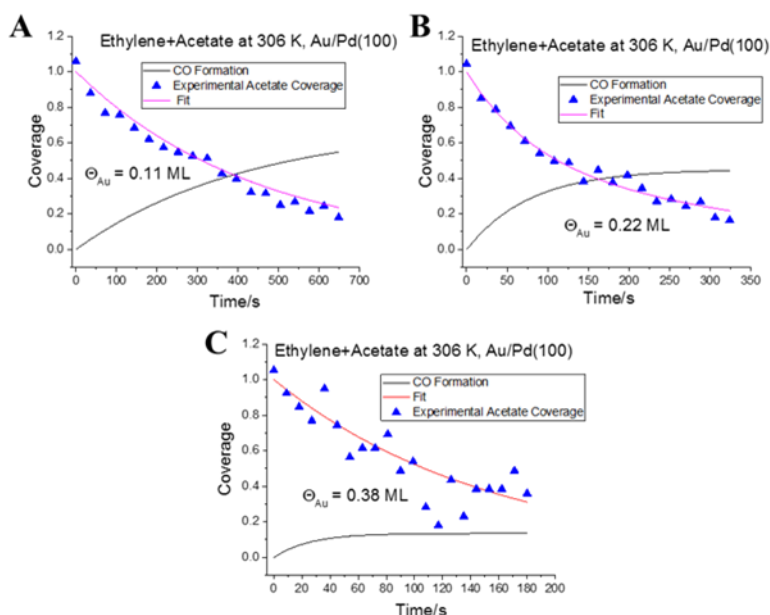
Figure 6.4.2: Plots of the time dependence of the integrated intensity of the 1407 cm^{-1} (acetate) features and the time dependence of the coverage of carbon monoxide as a function of time taken from the integrated area under the CO absorption peaks for low-gold coverage Au/Pd(100) alloys as a function of time. Data are shown for reactions carried out at 306 K for alloys with (A) 0.11, (B) 0.22, and (C) 0.38 ML of gold in the alloy.

between ethylene and acetate species is given by k_1 and $1 + \Theta_e^0 = \Theta_{tot}$, where Θ_e^0 is the initial coverage of ethylene that can adsorb onto an acetate-saturated surface, and was experimentally found to be ~0.37 ML. Eqn. 1 is normalized to yield an initial acetate coverage of unity. The CO-formation rate constant k_2 and Θ_{CO}^0 are obtained by separate measurements of CO accumulation, and the titration curves are fit to Eqn. 1 using k_1 as an independent variable. The resulting fits are shown in Fig. 6.4.2 for the three alloys, using the data in Fig. 6.3.1. This also displays the growth of CO coverage as a function of time. The agreement between the theoretical model and the experimental data is good.

Similar fits were carried out for the data collected at a reaction temperature of 260 K (Fig. 6.3.2), and provided similarly good fits. The resulting coupling rate constants k_1 for VAM formation on Au/Pd(100) alloys are plotted in Fig. 6.4.3. The VAM-formation rates increase with increasing gold coverage and are significantly higher than the reaction rate constant at ~306 K on Pd(111) of ~10^{-3} s^{-1} [8], in accord with the higher activity of model gold-palladium alloy catalysts [3]. This indicates that the gold in Au/Pd(100) alloys with gold coverages below ~0.5
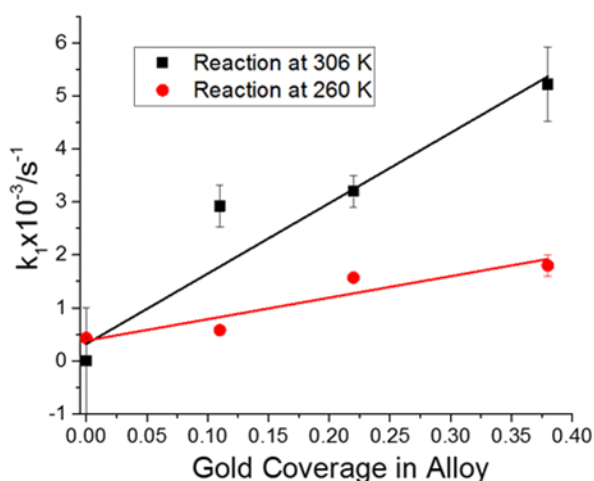
Figure 6.4.3: Plots of the reaction rate constant, k_1 for the coupling of ethylene and acetate species on low-gold coverage Au/Pd(100) alloys as a function of gold coverage for reactions carried out at 306 (■) and 260 (●) K.

ML not only increases the activity of the catalysts and shown in Fig. 6.4.3, but also increases the selectivity by inhibiting VAM decomposition to form CO (Fig. 6.4.2).

The picture for Au/Pd(100) alloys with gold coverages above ~0.5ML, when the proportion of palladium bridge sites decreases and isolated palladium site begin to dominate (Fig. 6.4.1), is completely different. Here, acetic acid no longer appears to form η^2 acetate species, but an adsorbate that has features at ~1590 and 1450 cm^{-1} (Figs. 6.3.3 and 6.3.4), where the reactivity with gas-phase decreases to essentially zero (Fig. 6.3.3), even at high ethylene background pressures (Fig. 6.3.4). The high-coverage alloys (with gold coverages of 0.66, 0.79 and 0.87 ML) contain only isolated palladium sites (Fig. 6.4.1). To confirm that the surface species derived from exposure to acetic acid on these high-gold-coverage alloys adsorb on isolated palladium sites, the scaled integrated areas of the most intense 43 amu TPD desorption profiles (Fig. 6.3.5B) are plotted versus gold coverage in Fig. 6.4.1 (▲). The variation in acetic acid yield scales with the variation in the coverage of isolated palladium sites, for which each of the nearest neighbors are gold atoms. This suggests that the strongly adsorbed acetate species, which produce acetic acid by heating to ~450 K (Fig. 6.3.5), but which are only completely removed from the alloy surface by heating to ~700 K (Fig. 6.3.6) are due to acetic acid reacting with isolated palladium sites having four gold nearest neighbors, but which is unreactive with gas-phase ethylene (Figs. 6.3.3 and 6.3.4).

The adsorption of molecular acetic acid as a candidates for this species can be excluded since it exhibits an intense C=O stretching mode between ~1650 and 1800 cm^{-1} [34, 35]. Binding of acetate species to a single metal center in inorganic compounds can be classified as unidentate, in which a O–C from the carboxylate group binds directly to the metal center (here a Pd surface atom), or chelating, and bidentate in which both carboxylate oxygens bind to the

111

metal center [36]. However, because of the extended alloy surface, direct comparison with acetate-containing organometallic compounds is not straightforward. For example, the asymmetric stretching mode for unidentate acetate species lies between ~1600 and 1710 cm^{-1}, close to the experimental frequency of 1590 cm^{-1}, but the corresponding symmetric stretching frequency is below ~1375 cm^{-1}, lower than the observed frequency of 1450 cm^{-1}. Bidentate acetate species generally have symmetric stretches between ~1500 and 1550 cm^{-1}, with a symmetric stretch from ~1375 to 1460 cm^{-1} [36], but this acetate species appears to ~1414 cm^{-1} on palladium surfaces with adjacent palladium atoms, which are not present on the high-gold-coverage Au/Pd(100) alloys. It is likely that the ~1590-cm^{-1} mode is due to an asymmetric COO stretch and the intense feature at ~1450 cm^{-1} to the corresponding symmetric stretching mode. The most likely structure is a unidentate acetate species with a strong Pd–O bond, in which the C=O group can interact with an adjacent gold atom. Such a structure would rationalize the lack of reactivity with ethylene; the η^2 acetate species can react with co-adsorbed ethylene in the Samanos pathway by inserting into one of the O–Pd bonds, while the other oxygen anchors it to the surface. This oxygen detaches once the C–O bond has formed to form the acetoxyethyl intermediate that then undergoes a β-hydride elimination reaction to form VAM. Such an insertion pathway would be inhibited on the alloy because of the stronger O–Pd bond. Also, the inability to stabilize the transition state, because of the lack of a second oxygen to bind to the surface, would also inhibit the reaction.

The lack of reactivity of acetic-acid derived species on Au/Pd(100) alloys appears to be inconsistent with the VAM activity of gold-palladium model single crystal alloy catalysts which suggest that Au/Pd(100) alloys with high gold coverages are the most active [3]. However, because adsorbates bind more strongly to palladium than gold, adsorption on gold-palladium

alloys has been found to enrich the surface in palladium, for example, in the presence of CO [37, 38] or acetate species [39]. A plausible explanation for the apparent high activity of gold-rich Au/Pd(100) alloy model catalysts with high gold coverages is that they become enriched by palladium in the presence of higher pressures of acetic acid and ethylene at catalytic reaction temperatures until the palladium coverage reaches a point at which palladium bridge sites start to appear to produce an active VAM synthesis catalyst (Fig. 6.4.3).

6.5 Conclusions

The reaction between gas-phase ethylene and acetic-acid derived species on Au/Pd(100) alloys differs substantially depending on the gold coverage in the alloy. Acetic acid forms reactive η^2 acetate species on Au/Pd(100) alloys with gold coverages below ~0.5 ML where the surface of the alloy contains palladium bridge sites. In this case, ethylene reacts rapidly with acetate species to form VAM, and this reaction is proposed to occur via the Samanos pathway via the formation of an acetoxyethyl-palladium intermediate. The rate constant for the coupling reaction is found to increase linearly with gold composition in the alloy. However, a portion of the VAM that is formed decomposes on the alloy to reform acetate species and produce carbon monoxide, where the extent to which this the non-selective reaction occurs decreases with increasing gold coverage.

The surface chemistry on Au/Pd(100) alloys with gold coverage greater than ~05 ML, which has been shown previously to have the highest activity for VAM formation, is completely different from that found for alloys with lower gold coverages. These alloys contain only isolated palladium sites that prevent the formation of η^2 acetate species as evidenced by completely different infrared spectra found on this surface after dosing with acetic acid. It is proposed that

the acetic acid reacts to form an η^1 acetate species with the second oxygen in the acetate group interacting with an adjacent gold site. This acetate species is completely unreactive with gas-phase ethylene, even for relatively high ethylene pressures of 2 Torr. This appears to be inconsistent with the catalytic reactivity of model gold-palladium alloy and it is suggested that this discrepancy can be rationalized by proposing that the alloy surface becomes enriched in palladium under reaction conditions to induce the appearance of reactive palladium bridge sites.

6.6 References

[1] P.M. Colling, L.R. Johnson, I. Nicolau, Palladium-gold catalyst for vinyl acetate production, in: U.S.P. Office (Ed.), Hoechst Celanese Corporation, United States, 1996.

[2] L. Horning, F. Wunder, T. Quadflieg, Process for Preparing Vinyl Acetates, in: F.H.A.V.M.L. Bruning (Ed.), United States, 1967.

[3] M. Chen, D. Kumar, C.-W. Yi, D.W. Goodman, The Promotional Effect of Gold in Catalysis by Palladium-Gold, Science, 310 (2005) 291-293.

[4] Y.F. Han, D. Kumar, D.W. Goodman, Particle size effects in vinyl acetate synthesis over Pd/SiO2, Journal of Catalysis, 230 (2005) 353-358.

[5] D. Stacchiola, F. Calaza, L. Burkholder, W.T. Tysoe, Vinyl acetate formation by the reaction of ethylene with acetate species on oxygen-covered Pd(111), Journal of the American Chemical Society, 126 (2004) 15384-15385.

[6] B. Samanos, P. Boutry, R. Montarnal, The mechanism of vinyl acetate formation by gas-phase catalytic ethylene acetoxidation, Journal of Catalysis, 23 (1971) 19-30.

[7] D. Stacchiola, F. Calaza, L. Burkholder, A.W. Schwabacher, M. Neurock, W.T. Tysoe, Elucidation of the Reaction Mechanism for the Palladium-Catalyzed Synthesis of Vinyl Acetate,

114

Angewandte Chemie International Edition, 44 (2005) 4572-4574.

[8] F. Calaza, D. Stacchiola, M. Neurock, W.T. Tysoe, Kinetic Parameters for the Elementary Steps in the Palladium-Catalyzed Synthesis of Vinyl Acetate, Catal Lett, 138 (2010) 135-142.

[9] F. Calaza, D. Stacchiola, M. Neurock, W.T. Tysoe, Coverage Effects on the Palladium-Catalyzed Synthesis of Vinyl Acetate: Comparison between Theory and Experiment, Journal of the American Chemical Society, 132 (2010) 2202-2207.

[10] F. Calaza, D. Stacchiola, M. Neurock, W.T. Tysoe, Structure and decomposition pathways of vinyl acetate on Pd(111), Surface Science, 598 (2005) 263-275.

[11] L.L. Kesmodel, L.H. Dubois, G.A. Somorjai, Dynamical LEED study of C2H2 and C2H4 chemisorption on Pt(111): evidence for the ethylidyne group, Chemical Physics Letters, 56 (1978) 267-271.

[12] D. Stacchiola, W.T. Tysoe, The Kinetics of Ethylidyne Formation from Ethylene on Pd(111), The Journal of Physical Chemistry C, 113 (2009) 8000-8001.

[13] L.V. Moskaleva, Z.-X. Chen, H.A. Aleksandrov, A.B. Mohammed, Q. Sun, N. Rösch, Ethylene Conversion to Ethylidyne over Pd(111): Revisiting the Mechanism with First-Principles Calculations, The Journal of Physical Chemistry C, 113 (2009) 2512-2520.

[14] F. Calaza, M. Mahapatra, M. Neurock, W.T. Tysoe, Disentangling ensemble, electronic and coverage effects on alloy catalysts: Vinyl acetate synthesis on Au/Pd(1 1 1), Journal of Catalysis, 312 (2014) 37-45.

[15] F. Calaza, Z.J. Li, W.T. Tysoe, Reaction Between Ethylene and Acetate Species on Clean and Oxygen-Covered Pd(100): Implications for the Vinyl Acetate Monomer Formation Pathway, Catal Lett, 141 (2011) 266-270.

[16] T. Thuening, W.T. Tysoe, Kinetics and Mechanism of Vinyl Acetate Monomer Synthesis on

Pd(100) Model Catalysts, Catal Lett, (2017) 1-14.

[17] J.A. Boscoboinik, C. Plaisance, M. Neurock, W.T. Tysoe, Monte Carlo and density functional theory analysis of the distribution of gold and palladium atoms on Au/Pd(111) alloys, Physical Review B, 77 (2008).

[18] B. Gleich, M. Ruff, R.J. Behm, Correlation between local substrate structure and local chemical properties: CO adsorption on well-defined bimetallic AuPd(111) surfaces, Surface Science, 386 (1997) 48-55.

[19] M. Garvey, J.A. Boscoboinik, L. Burkholder, J. Walker, C. Plaisance, M. Neurock, W.T. Tysoe, The Structure of the Au/Pd(100) Alloy Surface, Journal of Physical Chemistry C, 116 (2011) 6.

[20] Z. Li, T. Thuening, W.T. Tysoe, The adsorption of ethylene on Au/Pd(100) alloy surfaces, Surface Science.

[21] E.M. Stuve, R.J. Madix, C.R. Brundle, The adsorption and reaction of ethylene on clean and oxygen covered Pd(100), Surface Science, 152–153, Part 1 (1985) 532-542.

[22] E.M. Stuve, R.J. Madix, Bonding and dehydrogenation of ethylene on palladium metal. Vibrational spectra and temperature-programed reaction studies on palladium(100), The Journal of Physical Chemistry, 89 (1985) 105-112.

[23] Z. Li, F. Calaza, C. Plaisance, M. Neurock, W.T. Tysoe, Structure and Decomposition Pathways of Vinyl Acetate on Clean and Oxygen-Covered Pd(100), The Journal of Physical Chemistry C, 113 (2009) 971-978.

[24] Z. Li, F. Calaza, W.T. Tysoe, The adsorption and reaction of vinyl acetate on Au/Pd(100) alloy surfaces, Surface Science, 606 (2012) 1113-1119.

[25] Z. Li, W.T. Tysoe, The adsorption of acetic acid on clean and oxygen-covered Au/Pd(100)

116

alloy surfaces, Surface Science, 606 (2012) 1934-1941.

[26] D. Stacchiola, F. Calaza, L. Burkholder, A.W. Schwabacher, M. Neurock, W.T. Tysoe, Elucidation of the reaction mechanism for the palladium-catalyzed synthesis of vinyl acetate, Angew. Chem.-Int. Edit., 44 (2005) 4572-4574.

[27] D. Stacchiola, L. Burkholder, W.T. Tysoe, Ethylene adsorption on Pd(1 1 1) studied using infrared reflection–absorption spectroscopy, Surface Science, 511 (2002) 215-228.

[28] W.J. Wytenberg, R.M. Lambert, A Long-Lived Aluminium Evaporation Source for Controlled, Reproducible Deposition of Clean Ultra-Thin Films under UHV Conditions, Journal of Vacuum Science and Technology A, 10 (1992) 2.

[29] Z. Li, F. Gao, W.T. Tysoe, Carbon Monoxide Oxidation over Au/Pd(100) Model Alloy Catalysts, The Journal of Physical Chemistry C, 114 (2010) 16909-16916.

[30] N. Saliba, D.H. Parker, B.E. Koel, Adsorption of oxygen on Au(111) by exposure to ozone, Surface Science, 410 (1998) 270-282.

[31] T. Thuening, J. Walker, H. Adams, O. Furlong, W.T. Tysoe, Kinetics of low-temperature CO oxidation on Au(111), Surface Science, 648 (2016) 236-241.

[32] J. Szanyi, W.K. Kuhn, D.W. Goodman, CO adsorption on Pd(111) and Pd(100): Low and high pressure correlations, Journal of Vacuum Science & Technology A: Vacuum, Surfaces, and Films, 11 (1993) 1969-1974.

[33] M. Garvey, J.A. Boscoboinik, L. Burkholder, J. Walker, C. Plaisance, M. Neurock, W.T. Tysoe, Structure of the Au/Pd(100) Alloy Surface, The Journal of Physical Chemistry C, 116 (2012) 4692-4697.

[34] R. Haley, M. Tikhov, R. Lambert, The Surface Chemistry of Acetic Acid on Pd{111}, Catal Lett, 76 (2001) 125-130.

117

[35] J.L. Davis, M.A. Barteau, Hydrogen bonding in carboxylic acid adlayers on Pd(111): evidence for catemer formation, Langmuir, 5 (1989) 1299-1309.

[36] K. Nakamoto, Infrared and Raman spectra of inorganic and coordination compounds, John Wiley, New York, 1978.

[37] F. Gao, Y. Wang, D.W. Goodman, CO Oxidation over AuPd(100) from Ultrahigh Vacuum to Near-Atmospheric Pressures: The Critical Role of Contiguous Pd Atoms, Journal of the American Chemical Society, 131 (2009) 5734-5735.

[38] F. Gao, Y. Wang, D.W. Goodman, CO Oxidation over AuPd(100) from Ultrahigh Vacuum to Near-Atmospheric Pressures: CO Adsorption-Induced Surface Segregation and Reaction Kinetics, The Journal of Physical Chemistry C, 113 (2009) 14993-15000.

[39] T.G. Owens, T.E. Jones, T.C.Q. Noakes, P. Bailey, C.J. Baddeley, The Effects of Gold and Co-adsorbed Carbon on the Adsorption and Thermal Decomposition of Acetic Acid on Pd{111}, The Journal of Physical Chemistry B, 110 (2006) 21152-21160.

Chapter 7

Kinetics of Low-Temperature CO Oxidation on Au(111)

7.1 Introduction

The Somorjai group pioneered the idea that the flexibility and restructuring of metal surfaces was crucial to its catalytic activity and proposed the notion that adsorption on the surface caused structural changes in the metal surface that caused it to become more active [1-6]. In particular, the gold surface has been found to undergo very significant adsorbate-induced structural changes [7-10]. Consequently, while bulk gold is a noble metal and considered to be unreactive, oxide-supported gold nanoparticles have been found to have quite remarkable catalytic activity for a number of reactions [11-14]. In particular, it forms the basis for active CO oxidation catalysts [15-22]. Water has been suggested to play a role in accelerating the rate of CO oxidation [23-26] and has been studied primarily using molecular beam methods on Au(111) [27, 28]. Previous work has also been carried to explore carbon monoxide oxidation on gold surfaces in the absence of water [29, 30].

It has been suggested that oxygen is activated by dissociating either directly on low-coordination sites on the gold [31-33] or on the oxide support and the spilling over to the metal to then oxidize CO [33, 34]. In addition, it has been proposed that CO_2 can form *via* an intermediate $Au_2CO_3^-$ carbonate complex rather than by a simple addition of adsorbed atomic oxygen to adsorbed carbon monoxide [35-37].

119

Since carbon monoxide adsorbs very weakly on low-Miller-index gold surfaces [38-41], but more strongly on step sites [38], reaction on Au(111) might not be expected to occur in temperature-programmed desorption (TPD) so that experiments have been performed primarily using molecular beams of carbon monoxide incident on a gold-covered surface [27, 28, 30]. However, as shown below, the adsorption of carbon monoxide on Au(111), in particular in the presence of co-adsorbed oxygen, is sufficiently strong that both TPD and reflection-absorption infrared spectroscopy (RAIRS) can be used to explore the reaction pathway.

Controlled atomic oxygen coverages are obtained by exposing the surface to ozone [42], which also contains molecular oxygen, which does not adsorb at room temperature. TPD experiments show the direct oxidation of carbon monoxide on the gold surface, thereby allowing the desorption and reaction activation energies to be estimated [43]. This also enables the surface to be interrogated using RAIRS over the same temperature range as that at which the oxidation chemistry occurs to search for any reaction intermediates such a carbonates since their vibrational frequencies [44] are distinct from those for CO on gold [45].

7.2 Experimental Methods

The apparatus used to collect RAIRS and TPD data has been described in detail elsewhere [46]. Infrared spectra were collected using a Bruker Equinox spectrometer, typically for 1000 scans at a resolution of 4 cm^{-1}. TPD data were collected using a Dichor quadrupole mass spectrometer interfaced to a computer that allowed up to five masses to be monitored sequentially in a single experiment. The sample could be cooled to 80 K by thermal contact to a liquid-nitrogen-filled reservoir and resistively heated to ~1200 K.

A Au(111) single crystal (Princeton Scientific) was cleaned with cycles of ion bombardment using 1 keV argon ions for 30 minutes (1 μA/cm^2), annealing to 900 K for 5 minutes and then to 600 K for 30 minutes. Ozone was produced by an A2Z Ozone Inc., 5GLAB ozone generator where the output of the generator was connected *via* a Teflon tube directly to a high-precision variable leak valve through a 1 mm-diameter glass tube that was directed at the inlet of the leak valve to minimize ozone decomposition. The ozone was returned through an external concentric glass tube and led though a Teflon tube to a fume hood. The proportion of ozone in the gas mixture was maximized by monitoring the 32 (O_2^+) and 48 (O_3^+) signals in the mass spectrometer located inside the vacuum chamber and it is estimated that the ozone concentration in the gas mixture is ~4%.

7.3 Results

7.3.1 Oxygen Adsorption from Ozone on Au(111)

TPD data were collected for atomic oxygen adsorbed from ozone on Au(111) as a function of exposure Oxygen (32 amu) desorbs in a sharp peak centered at ~540 K at low coverages and shifts to higher coverages with exposure so that at the highest coverage desorbs at ~560 K (data not shown). These desorption profiles and peak temperatures are in good agreement with previous measurements on Au(111) [42]. Measuring the oxygen coverage from the integrated area under the desorption peak compared with previous results allows the oxygen coverage to be calibrated as a function of exposure to the mixture of O_2+O_3, and the results described below use oxygen coverages calibrated in this way.

7.3.2 Carbon Monoxide Oxidation on Au(111)

The oxidation of CO was explored using TPD on oxygen-covered Au(111) by adsorbing atomic oxygen using ozone [42]. A series of TPD spectra for a Au(111) sample initially containing 0.2 ML of atomic oxygen are shown in Fig. 7.3.2.1 as a function of CO exposure. CO (28 amu) is found to desorb in two distinct states from oxygen-covered Au(111) at ~132 and 174 K (Fig. 7.3.2.1A), that grow approximately equally as a function of CO exposure. This results in low-temperature CO_2 (44 amu) formation (Fig. 7.3.2.1B), initially in a single peak centered at ~168 K that grows with increasing CO exposure, followed by the growth of an additional CO_2 state at ~142 K. Clearly, the high-temperature CO_2 state must be associated with oxidation of the more stable CO that desorbs at ~174 K (Fig. 7.3.2.1A). The reaction of carbon monoxide with surface atomic oxygen is confirmed by the decrease in intensity of the remaining oxygen (32 amu) feature with increasing CO exposure (Fig. 7.3.2.1C).
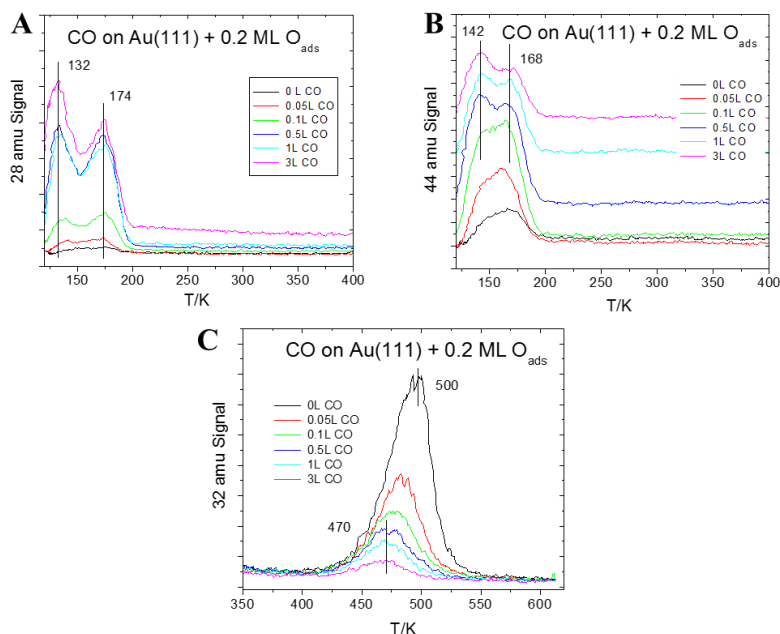
Figure 7.3.2.1: TPD profiles [(A) 28, (B) 44, and (C) 32 amu] of CO adsorbed at 80K on a surface precovered by 0.2 ML of atomic oxygen collected using a heating rate of 3.4 K/s as a function of CO exposure.

The corresponding results for a higher oxygen coverage of 0.75 ML are shown in Fig. 7.3.2.2. Now the lower-temperature CO desorption state (28 amu), centered at ~153 K, is less intense than the higher-temperature CO desorption state that shifts in temperature from ~190 to ~222 K (Fig. 7.3.2.2A). Intense CO_2 desorption states (44 amu) are measured with a peak initially appearing at ~173 K, shifting to higher temperatures up to ~212 K as the CO exposure increases (Fig. 7.3.2.2B).
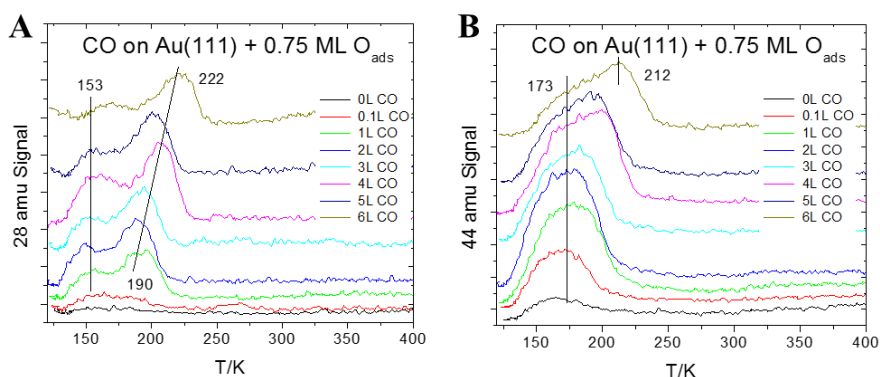
Figure 7.3.2.2: TPD profiles [(A) 28, (B) 44, and (C) 32 amu] of CO adsorbed at 80K on a surface precovered by 0.75 ML of atomic oxygen collected using a heating rate of 3.4 K/s as a function of CO exposure.

The effect of varying the oxygen coverage is shown in Fig. 7.3.2.3 for a CO exposure of 10 L, resulting in saturation of the surface with CO. Again, two CO (28 amu) desorption states are observed; a low-temperature state centered at ~141 K that initially grows in parallel with the higher-temperature state, and then decreases in intensity for oxygen coverages above ~0.9 ML, while both states decrease in intensity at higher oxygen coverages (Fig. 7.3.2.3A). Carbon dioxide (44 amu) desorbs in a broad feature between ~130 and 210 K, with an intensity that grows up to an oxygen coverage of ~0.9 ML, and then decreases (Fig. 7.3.2.3B). The corresponding oxygen desorption profiles (32 amu) are shown in Fig. 7.3.2.3C. The resulting stoichiometric reaction between adsorbed CO and oxygen is illustrated by the data in Fig. 7.3.2.4. This plots the coverage of CO_2 that is produced (●) and the adsorbed oxygen that is
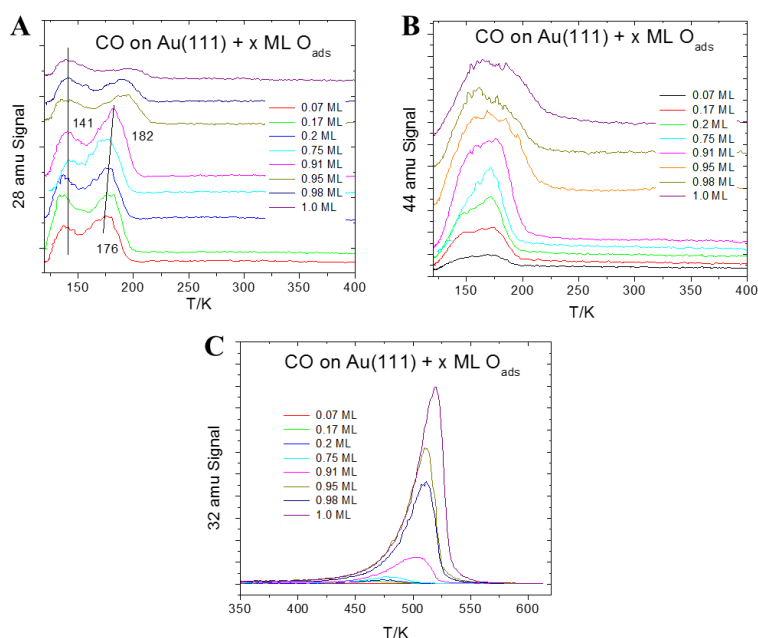
Figure 7.3.2.3: TPD profiles [(A) 28, (B) 44, and (C) 32 amu] of 10L CO adsorbed at 80K on a surface with various coverages of atomic oxygen collected using a heating rate of 3.4 K/s as a function of CO exposure.

consumed (■) as a function of oxygen coverage. Here the coverage of oxygen consumed is measured from the area of the 32 amu profile in the presence of carbon monoxide (Fig. 7.3.2.3C) compared to the area for an identical oxygen dose without CO. There is good agreement between the two sets of data indicating a quantitative reaction between adsorbed oxygen and CO (Fig. 7.3.2.4). The carbon dioxide that is initially formed is limited by the inventory of oxygen on the surface, which is completely consumed by reaction with CO. At higher oxygen coverages, some oxygen remains on the surface so that the CO_2 yield becomes limited by the amount of carbon monoxide. However, in this case, not all of the carbon monoxide is consumed and a portion desorbs when there is still oxygen on the surface. At coverages above ~0.8 ML of oxygen, the carbon dioxide yield decreases due to the blocking of CO adsorption by atomic oxygen.

124
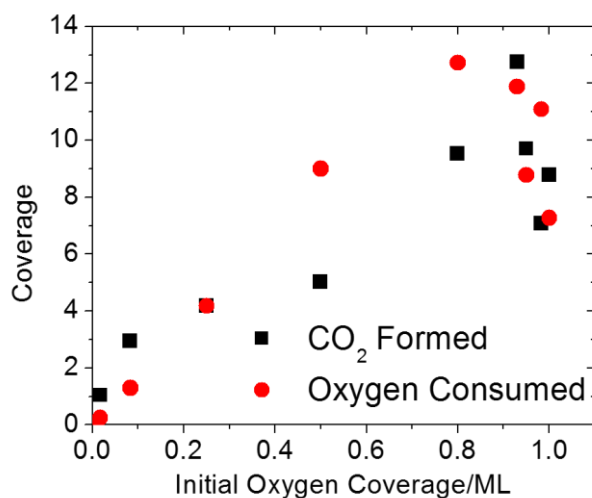
Figure 7.3.2.4: Plot of the equivalent coverage of carbon dioxide produced versus the coverage of oxygen consumed due to a reaction between atomic oxygen and CO adsorbed at 80 K on oxygen-covered Au(111) as a function of oxygen coverage.

The corresponding infrared spectra for CO on clean Au(111) following adsorption at 87 K are shown in Fig. 7.3.2.5A. The spectrum at 87 K exhibits a peak at ~2110 cm^{-1}, close to the value of 2118 cm^{-1} found previously for low-temperature CO adsorption on Au(111) [47]. Additional spectra show the effect of heating the surface to various temperatures for 10 s and then allowing the sample to cool once again to ~87 K following which the spectrum was collected. This shows a decrease in the intensity of the infrared peaks and the inset plots the integrated absorbance of the infrared features as a function of annealing temperature. An additional shift in peak position is noted as the CO coverage changes due to a combination of dipolar coupling and chemical shifts [48, 49]. The CO vibrational frequency of 2110 cm^{-1} is in good agreement with results for high pressures of CO on Au(110) [50] and for CO adsorption at low-temperatures on Au(211) [38] and Au(332) surfaces [41]. However, CO adsorption on Au(111) at high pressures (up to 100 Torr) showed a single infrared mode at 2060 cm^{-1} that did not change position with coverage [40]. In this case, considerable surface restructuring was noted at those higher CO pressures [51]. It has been shown that the CO stretching frequency,

125

while being relatively insensitive to gold coordination number, is a reasonably sensitive probe of

the gold charge state [45], where Au^0-CO has a CO stretching mode between 2130 and 2090 cm^{-1} in agreement with a frequency of ~2110 cm^{-1} found in Fig. 7.3.2.5A.

Fig. 7.3.2.5B shows the CO stretching region of CO adsorbed on a surface containing 0.2

ML of oxygen as a function of CO exposure. Two infrared peaks at 2135 and 2110 cm^{-1} grow

simultaneously with increasing CO exposure, corresponding to the growth of two desorption

states found in TPD (Fig. 7.3.2.1). Comparison with the infrared spectrum on clean Au(111)

(Fig. 7.3.2.5A) suggests that the 2135 cm^{-1} state is induced by co-adsorbed atomic oxygen while

the 2110 cm^{-1} state is due to CO on unaffected sites. The appearance of the feature at ~2135 cm^{-1} is consistent with CO adsorption on $Au^{\delta+}$ sites [45], which appear at higher frequencies than

CO on Au^0 sites, generally between 2150 and 2190 cm^{-1}.
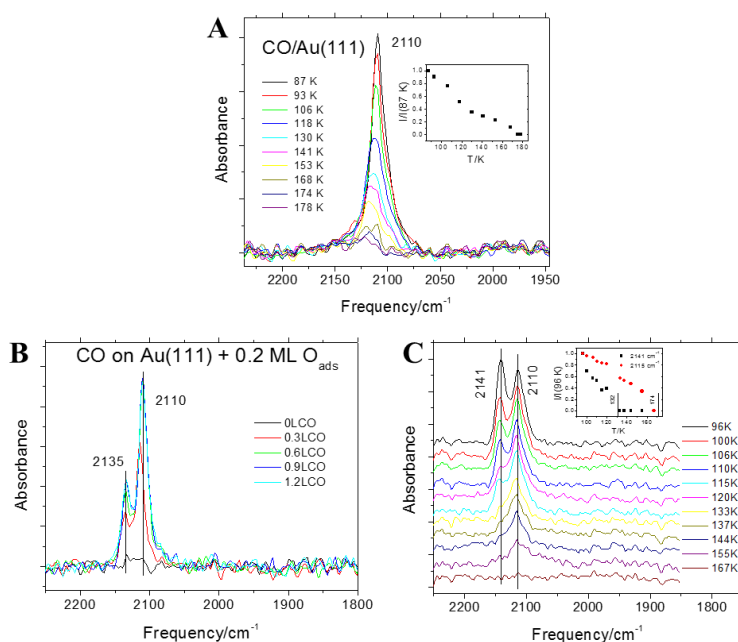
Figure 7.3.2.5: (A) RAIRS spectra of CO on Au(111) at 87 K and heated to various temperatures. Inset shows the variation in integrated absorbance with temperature. (B) CO adsorbed on Au(111) with 0.2 ML of atomic oxygen as a function of oxygen exposure. (C) RAIRS spectra of a saturated overlayer of CO (~10 L exposure) on Au(111) with 0.2 ML of atomic oxygen as a function of annealing temperature. Inset shows the variation in integrated absorbances of the 2121 and 2110 cm^{-1} peaks as a function of annealing temperature.

126

The evolution in the infrared spectra as a function of annealing temperature is shown in Fig. 7.3.2.5C for a saturation CO exposure of ~10 L. The results were obtained by heating to the indicated temperature and then allowing the sample to cool once again, following which the infrared spectra were collected. The higher CO coverages in this case result in additional spectral shifts compared to the data with lower CO coverages (Fig. 7.3.2.5B). In particular, the peak for CO on oxygen-modified sites shifts to ~2141 cm^{-1}. The variation in integrated peak area as a function of annealing temperature is shown plotted as an inset to Fig. 7.3.2.5C where the peak desorption temperatures found for the same surface (Fig. 7.3.2.1A), are indicated. This reveals that that the low-temperature (~132 K) desorption feature in Fig. 7.3.2.1 is associated with CO bound to $Au^{\delta+}$ sites, while the higher temperature, ~174 K state is due to CO adsorbed on Au^0 sites.

No other vibrational modes were detected during this experiment indicating that CO reacts directly with adsorbed atomic oxygen to form carbon dioxide without forming any stable surface intermediates.

7.4 Discussion

Addition of oxygen to the surface produced two distinct desorption states comprising a low-temperature state with a peak centered between ~130 to 150 K, and a higher-temperature state with a peak temperature that varies from ~175 to ~220 K depending on the initial oxygen and CO coverages. A Redhead analysis [43] using the experimental heating rate and assuming a pre-exponential factor of 1×10^{13} s^{-1} yield CO desorption activation energies of 32 to 37 kJ/mol for the low-temperature state and from 44 to 56 kJ/mol for the high-temperature state. The

127

infrared data suggest that the low-temperature states are associated with CO adsorbed on $Au^{\delta+}$ sites and the higher-temperature desorption features are due to adsorption on gold sites.

The CO 4σ, 1π and 5σ orbitals are located below the bottom of the gold d-band while the $2\pi^*$ orbitals located are close to the Fermi level [52] corresponding to the conventional Blyholder model for CO adsorption on transition-metal surfaces [53]. However, the low density of states of gold near the Fermi level leads to only relatively weak back donation into the $2\pi^*$ level, with CO acting as a weak π-acceptor, resulting in low binding energies. Thus removing electron density from the gold by co-adsorbing atomic oxygen increases the energy difference between the Fermi energy and the CO $2\pi^*$ orbitals, thereby weakening the bonding as found experimentally. A similar shift to higher frequencies (in this case to ~2146 cm^{-1}) has been seen for CO co-adsorbed with hydroxyl species on Au(111) [47] consistent with this bonding model.

However, creating low-coordination sites on a roughened surface can increase the binding strength of CO [54]. In fact, the desorption peak temperatures for the two CO desorption states found on oxygen-modified Au(111) are very similar to those found for gold nanoparticles on FeO [55] and on surfaces roughened by oxygen or argon ion bombardment [56] indicating that surface roughening has some influence on CO binding. It is interesting to note that the infrared spectrum of CO adsorbed on gold nanoparticles on FeO exhibits a single vibrational feature centered at ~2108 cm^{-1}, similar to the low-frequency feature found on the oxygen-covered surface (Fig. 7.3.2.5B and 7.3.2.5C). However, the CO stretching frequency on gold is notoriously insensitive to surface structure, as evidenced by the similarity between the vibrational frequency on Au(111) (Fig. 7.3.2.5A) and on oxygen-covered surfaces, which have been roughed by oxygen adsorption. Heating CO-covered gold nanoparticles on FeO resulted in a reduction in the intensity of the 2108 cm^{-1} peak over a temperature range that was coincident

128

the high-temperature (~200 K) CO desorption state, while no intensity decrease was noted when CO desorbed at lower temperatures. This was ascribed to the weakly bound CO that desorbs at ~130 K, but which lies parallel to the surface, and is thus infrared forbidden [55, 57].

In the case of oxygen-modified Au(111), the ~2141 cm^{-1} vibrational mode, assigned to CO adsorption on Au$^{\delta+}$ sites, decreases in intensity coincident with the low-temperature CO desorption peak but does not exclude the possibility of there also being some infrared-invisible CO also being present on the surface.

Adsorbed CO reacts quantitatively with adsorbed atomic oxygen to form carbon dioxide (Fig. 7.3.2.4) where the amount of carbon dioxide initially increases with oxygen coverage but decreases at higher coverages due to site blocking similar to the behavior found previously for CO oxidation on Au(111) using molecular beams of CO [30]. No intermediate surface species are detected following CO adsorption on oxygen-covered Au(111), indicating that CO_2 is formed by a direct coupling between CO and adsorbed oxygen to immediately desorb CO_2 [37]. The carbon dioxide that is formed desorbs over the same range as CO suggesting that the activation energies for CO_2 formation also lie approximately in the range of ~32 to 56 kJ/mol and is in the same range as the activation energies for CO oxidation on gold nanoparticle catalysts for reaction carried out below ~300 K [58].

7.5 Conclusions

Combined infrared and TPD experiments reveal that Au(111) single crystals exposed to ozone to form adsorbed atomic oxygen can oxidize CO to CO_2 at temperatures as low as ~140 K. CO desorbs in two states where the low-temperature state is assigned to CO adsorbed on Au$^{\delta+}$ sites and the higher-temperature desorption features are due to adsorption on gold sites. This

129

observation is consistent with the Blyholder model. However, the low-temperature state may also include contributions from infrared-invisible CO bound with its axis parallel to the surface.

Carbon dioxide forms over the same temperature range as that at which CO desorbs suggesting that the formation activation energy is between ~32 to 56 kJ/mol, in the range for CO oxidation by supported catalysts. Infrared spectroscopy reveals only features due to molecularly adsorbed carbon monoxide suggesting that the CO_2 forms directly without the intervention of any other intermediate species such as carbonates.

7.6 References

[1] R.J. Koestner, M.A. Van Hove, G.A. Somorjai, Molecular structure of hydrocarbon monolayers on metal surfaces, The Journal of Physical Chemistry, 87 (1983) 203-213.

[2] G.A. Somorjai, The flexible surface. Correlation between reactivity and restructuring ability, Langmuir, 7 (1991) 3176-3182.

[3] G.A. Somorjai, The experimental evidence of the role of surface restructuring during catalytic reactions, Catal Lett, 12 (1992) 17-34.

[4] G.A. Somorjai, Molecular concepts of heterogeneous catalysis, Journal of Molecular Structure: THEOCHEM, 424 (1998) 101-117.

[5] G.A. Somorjai, The Development of Molecular Surface Science and the Surface Science of Catalysis: The Berkeley Contribution†, The Journal of Physical Chemistry B, 104 (2000) 2969-2979.

[6] G.A. Somorjai, The Evolution of Surface Chemistry. A Personal View of Building the Future on Past and Present Accomplishments, The Journal of Physical Chemistry B, 106 (2002) 9201-9213.

[7] J. Gong, Structure and Surface Chemistry of Gold-Based Model Catalysts, Chemical Reviews, 112 (2012) 2987-3054.

[8] P. Maksymovych, J.T. Yates, Au Adatoms in Self-Assembly of Benzenethiol on the Au(111) Surface, Journal of the American Chemical Society, 130 (2008) 7518-7519.

[9] J. Boscoboinik, J. Kestell, M. Garvey, M. Weinert, W. Tysoe, Creation of Low-Coordination Gold Sites on Au(111) Surface by 1,4-phenylene Diisocyanide Adsorption, Topics in Catalysis, 54 (2011) 20-25.

[10] J.A. Boscoboinik, F.C. Calaza, Z. Habeeb, D.W. Bennett, D.J. Stacchiola, M.A. Purino, W.T. Tysoe, One-dimensional supramolecular surface structures: 1,4-diisocyanobenzene on Au(111) surfaces, Phys. Chem. Chem. Phys., 12 (2010) 11624-11629.

[11] M. Haruta, N. Yamada, T. Kobayashi, S. Iijima, Gold catalysts prepared by coprecipitation for low-temperature oxidation of hydrogen and of carbon monoxide, Journal of Catalysis, 115 (1989) 301-309.

[12] M. Haruta, Size- and support-dependency in the catalysis of gold, Catalysis Today, 36 (1997) 153-166.

[13] G. Hutchings, Catalysis: A golden future, Gold Bulletin, 29 (1996) 123-130.

[14] J. Edwards, P. Landon, A.F. Carley, A.A. Herzing, M. Watanabe, C.J. Kiely, G.J. Hutchings, Nanocrystalline gold and gold–palladium as effective catalysts for selective oxidation, Journal of Materials Research, 22 (2007) 831-837.

[15] A.A. Herzing, C.J. Kiely, A.F. Carley, P. Landon, G.J. Hutchings, Identification of Active Gold Nanoclusters on Iron Oxide Supports for CO Oxidation, Science, 321 (2008) 1331-1335.

[16] A.M. Venezia, L.F. Liotta, G. Pantaleo, V. La Parola, G. Deganello, A. Beck, Z. Koppány, K. Frey, D. Horváth, L. Guczi, Activity of SiO2 supported gold-palladium catalysts in CO oxidation, Applied Catalysis A: General, 251 (2003) 359-368.

[17] L. Guczi, G. Petö, A. Beck, K. Frey, O. Geszti, G. Molnár, C. Daróczi, Gold Nanoparticles Deposited on SiO2/Si(100): Correlation between Size, Electron Structure, and Activity in CO Oxidation, Journal of the American Chemical Society, 125 (2003) 4332-4337.

[18] C. Xu, J. Su, X. Xu, P. Liu, H. Zhao, F. Tian, Y. Ding, Low Temperature CO Oxidation over Unsupported Nanoporous Gold, Journal of the American Chemical Society, 129 (2007) 42-43.

[19] J.-D. Grunwaldt, C. Kiener, C. Wögerbauer, A. Baiker, Preparation of Supported Gold Catalysts for Low-Temperature CO Oxidation via "Size-Controlled" Gold Colloids, Journal of Catalysis, 181 (1999) 223-232.

[20] Y. Liu, C.-J. Jia, J. Yamasaki, O. Terasaki, F. Schüth, Highly Active Iron Oxide Supported Gold Catalysts for CO Oxidation: How Small Must the Gold Nanoparticles Be?, Angewandte Chemie International Edition, 49 (2010) 5771-5775.

[21] M. Comotti, W.-C. Li, B. Spliethoff, F. Schüth, Support Effect in High Activity Gold Catalysts for CO Oxidation, Journal of the American Chemical Society, 128 (2006) 917-924.

[22] M. Valden, S. Pak, X. Lai, D.W. Goodman, Structure sensitivity of CO oxidation over model Au/TiO$_2$$_2$ catalysts, Catal Lett, 56 (1998) 7-10.

[23] J. Saavedra, H.A. Doan, C.J. Pursell, L.C. Grabow, B.D. Chandler, The critical role of water at the gold-titania interface in catalytic CO oxidation, Science, 345 (2014) 1599-1602.

[24] T. Fujitani, I. Nakamura, M. Haruta, Role of Water in CO Oxidation on Gold Catalysts, Catal Lett, 144 (2014) 1475-1486.

[25] M. Date, M. Haruta, Moisture effect on CO oxidation over Au/TiO2 catalyst, Journal of Catalysis, 201 (2001) 221-224.

[26] M. Date, M. Okumura, S. Tsubota, M. Haruta, Vital role of moisture in the catalytic activity of supported gold nanoparticles, Angewandte Chemie-International Edition, 43 (2004) 2129-2132.

[27] R.A. Ojifinni, N.S. Froemming, J. Gong, M. Pan, T.S. Kim, J.M. White, G. Henkelman, C.B. Mullins, Water-Enhanced Low-Temperature CO Oxidation and Isotope Effects on Atomic Oxygen-Covered Au(111), Journal of the American Chemical Society, 130 (2008) 6801-6812.

[28] T.S. Kim, J. Gong, R.A. Ojifinni, J.M. White, C.B. Mullins, Water activated by atomic oxygen on Au(111) to oxidize CO at low temperatures, Journal of the American Chemical Society, 128 (2006) 6282-6283.

[29] J. Michael Gottfried, K. Christmann, Oxidation of carbon monoxide over Au(1 1 0)-(1 × 2), Surface Science, 566–568, Part 2 (2004) 1112-1117.

[30] B.K. Min, A.R. Alemozafar, D. Pinnaduwage, X. Deng, C.M. Friend, Efficient CO Oxidation at Low Temperature on Au(111)†, The Journal of Physical Chemistry B, 110 (2006) 19833-19838.

[31] X.Y. Deng, B.K. Min, A. Guloy, C.M. Friend, Enhancement of O-2 dissociation on Au(111) by adsorbed oxygen: Implications for oxidation catalysis, Journal of the American Chemical Society, 127 (2005) 9267-9270.

[32] V.A. Bondzie, S.C. Parker, C.T. Campbell, Oxygen adsorption on well-defined gold particles on TiO2(110), Journal of Vacuum Science & Technology a-Vacuum Surfaces and Films, 17 (1999) 1717-1720.

[33] M.M. Schubert, S. Hackenberg, A.C. van Veen, M. Muhler, V. Plzak, R.J. Behm, CO oxidation over supported gold catalysts-"inert" and "active" support materials and their role for the oxygen supply during reaction, Journal of Catalysis, 197 (2001) 113-122.

[34] J.D. Grunwaldt, A. Baiker, Gold/titania interfaces and their role in carbon monoxide oxidation, Journal of Physical Chemistry B, 103 (1999) 1002-1012.

[35] H. Hakkinen, U. Landman, Gas-phase catalytic oxidation of CO by Au-2(-), Journal of the American Chemical Society, 123 (2001) 9704-9705.

[36] P. Konova, A. Naydenov, C. Venkov, D. Mehandjiev, D. Andreeva, T. Tabakova, Activity and deactivation of Au/TiO2 catalyst in CO oxidation, Journal of Molecular Catalysis a-Chemical, 213 (2004) 235-240.

[37] R.A. Ojifinni, J. Gong, N.S. Froemming, D.W. Flaherty, M. Pan, G. Henkelman, C.B. Mullins, Carbonate formation and decomposition on atomic oxygen precovered Au(111), Journal of the American Chemical Society, 130 (2008) 11250-+.

[38] J. Kim, E. Samano, B.E. Koel, CO adsorption and reaction on clean and oxygen-covered Au(211) surfaces, Journal of Physical Chemistry B, 110 (2006) 17512-17517.

[39] M.L. Kottke, R.G. Greenler, H.G. Tompkins, An infrared spectroscopic study of carbon monoxide adsorbed on polycrystalline gold using the reflection-absorption technique, Surface Science, 32 (1972) 231-243.

134

[40] L. Piccolo, D. Loffreda, F. Aires, C. Deranlot, Y. Jugnet, P. Sautet, J.C. Bertolini, The adsorption of CO on Au(111) at elevated pressures studied by STM, RAIRS and DFT calculations, Surface Science, 566 (2004) 995-1000.

[41] C. Ruggiero, P. Hollins, Adsorption of carbon monoxide on the gold(332) surface, Journal of the Chemical Society, Faraday Transactions, 92 (1996) 4829-4834.

[42] N. Saliba, D.H. Parker, B.E. Koel, Adsorption of oxygen on Au(111) by exposure to ozone, Surface Science, 410 (1998) 270-282.

[43] P.A. Redhead, Thermal desorption of gases, Vacuum, 12 (1962) 9.

[44] K. Nakamoto, Infrared and Raman spectra of inorganic and coordination compounds, Wiley, New York, 1997.

[45] M. Mihaylov, H. Knozinger, K. Hadjiivanov, B.C. Gates, Characterization of the oxidation states of supported gold species by IR spectroscopy of adsorbed CO, Chemie Ingenieur Technik, 79 (2007) 795-806.

[46] M. Kaltchev, A.W. Thompson, W.T. Tysoe, Reflection-absorption infrared spectroscopy of ethylene on palladium (111) at high pressure, Surface Science, 391 (1997) 145-149.

[47] S.D. Senanayake, D. Stacchiola, P. Liu, C.B. Mullins, J. Hrbek, J.A. Rodriguez, Interaction of CO with OH on Au(111): HCOO, CO3, and HOCO as Key Intermediates in the Water-Gas Shift Reaction, The Journal of Physical Chemistry C, 113 (2009) 19536-19544.

[48] P. Dumas, R.G. Tobin, P.L. Richards, Study of adsorption states and interactions of CO on evaporated noble metal surfaces by infrared absorption spectroscopy: I. Silver, Surface Science, 171 (1986) 555-578.

[49] P. Dumas, R.G. Tobin, P.L. Richards, Interaction of co molecules with evaporated silver, gold, and copper films: an infrared spectroscopic investigation using a thermal detection technique, Journal of Electron Spectroscopy and Related Phenomena, 39 (1986) 183-189.

[50] Y. Jugnet, F. Aires, C. Deranlot, L. Piccolo, J.C. Bertolini, CO chemisorption on Au(110) investigated under elevated pressures by polarized reflection absorption infrared spectroscopy and scanning tunneling microscopy, Surface Science, 521 (2002) L639-L644.

[51] K.F. Peters, P. Steadman, H. Isern, J. Alvarez, S. Ferrer, Elevated-pressure chemical reactivity of carbon monoxide over Au(111), Surface Science, 467 (2000) 10-22.

[52] B. Hammer, Y. Morikawa, J.K. Nørskov, CO Chemisorption at Metal Surfaces and Overlayers, Physical Review Letters, 76 (1996) 2141-2144.

[53] G. Blyholder, Molecular Orbital View of Chemisorbed Carbon Monoxide, The Journal of Physical Chemistry, 68 (1964) 2772-2777.

[54] T.V.W. Janssens, B.S. Clausen, B. Hvolbaek, H. Falsig, C.H. Christensen, T. Bligaard, J.K. Norskov, Insights into the reactivity of supported Au nanoparticles: combining theory and experiments, Topics in Catalysis, 44 (2007) 15-26.

[55] C. Lemire, R. Meyer, S. Shaikhutdinov, H.-J. Freund, Do Quantum Size Effects Control CO Adsorption on Gold Nanoparticles?, Angewandte Chemie International Edition, 43 (2004) 118-121.

[56] J. Biener, M.M. Biener, T. Nowitzki, A.V. Hamza, C.M. Friend, V. Zielasek, M. Bäumer, On the Role of Oxygen in Stabilizing Low-Coordinated Au Atoms, Chemphyschem, 7 (2006) 1906-1908.

[57] R.G. Greenler, Infrared Study of Adsorbed Molecules on Metal Surfaces by Reflection Techniques, The Journal of Chemical Physics, 44 (1966) 310-315.

[58] M. Haruta, Nanoparticulate gold catalysts for low-temperature CO oxidation, Journal of New Materials for Electrochemical Systems, 7 (2004) 163-172.

137

Chapter 8

Interaction of Hydrogen and Carbon Monoxide on Au/Pd(100) Alloys: Controlling Subsurface Hydrogen

8.1 Introduction

The catalytic hydrogenations of unsaturated hydrocarbons over transition metal surfaces has been investigated for much of the last century with palladium distinguishing itself as a premier catalyst for the hydrogenation of ethylene and acetylene due to its high activity and selectivity. Work by Beeck [1] was initially done in the 1940s and 1950s to correlate the electronic configuration and crystal parameters of transition metals to their hydrogenation reactivity for typical catalytic metals, including palladium. Intrinsic to understanding reaction pathways on surfaces is to understand the reactant adsorption and the nature of the binding sites. Accordingly, the Ertl group intensively studied the adsorption of hydrogen onto Pd(110) and Pd(111) single-crystal surfaces [2, 3], where complex adsorption behavior was observed, and four distinct hydrogen desorption states were found. Through the use of work function, LEED and TPD measurements, along with comparisons to prior work on nickel surfaces, the desorption states were identified as two subsurface species and two chemisorbed, surface species. Low doses of hydrogen at low temperatures were found to chemisorb on palladium and desorb in a broad peak in TPD from 250-400 K. As the exposure of hydrogen increased, a (2×1) and, after further increasing the exposure, a (1×2) surface reconstruction was formed, allowing for

138

hydrogen adsorption into two distinct subsurface states that fill simultaneously, and desorb in two low-temperature TPD peaks centered at ~150 K and ~230 K respectively, and have been designated "α_1" and "α_2" species. This behavior was also shown to occur on Pd(100) single crystal surfaces [4]. It is important to note that hydrogen dosed at room temperature displays different binding to palladium surfaces. Specifically, a surface hydrogen species is present in the same temperature range (~250-400 K), but a bulk hydrogen species is observed that desorbs in a very broad feature from ~400 K to greater than 800 K [5]. Clearly, bulk hydrogen when dosed at room temperature is distinct from the subsurface species seen when hydrogen is dosed at low temperatures, and is believed to be due to hydrogen adsorbed deeper into the bulk of the palladium crystal.

Palladium catalysts have been found to benefit, primarily in selectivity, from alloying with gold for a number of reactions [6-10], and as such, the adsorption of hydrogen on Au/Pd alloys has been studied, where two seemingly contradictory hydrogen adsorption behaviors having recently been reported. The Sykes group, working with so-called "single-atom" alloys (SAAs), incorporate small coverages of palladium on a Au(111) substrate to create isolated palladium atoms, and observe that hydrogen adsorbs and dissociates even on these isolated palladium sites. When dosing a hydrogen-covered surface with CO, the hydrogen is displaced from palladium atoms onto the gold surface, subsequently desorbing at very low temperatures from the recombination of hydrogen atoms on gold sites[11]. This CO induced displacement is referred to as a "spillover effect". Conversely, the Fukutani group studied Au/Pd(110) alloy single crystals to investigate hydrogen adsorption on Au/Pd alloys[12, 13]. This surface, likely due to the higher concentration of palladium, and specifically the presence of more subsurface palladium, displays different behavior for hydrogen and the effect of CO adsorption. Hydrogen

139

is found to adsorb on the surface, and be transported into the subsurface region, similar to the behavior observed by the Ertl group. Upon exposing the hydrogen-covered surface to CO, hydrogen is contained to remain in the subsurface of the crystal to elevated temperatures (~400-500 K), where it is proposed that CO has capped the available surface palladium atoms that act as a desorption sites for subsurface hydrogen. Once CO has desorbed, hydrogen is released from the subsurface and desorbs at the same temperature as CO. This effect has been dubbed the "cork effect" as the CO acts as a "cork" to keep hydrogen in the subsurface, preventing it from desorbing.

These two distinct effects provide exciting opportunities for tuning hydrogenation activity as well as having potential hydrogen storage applications; but better understanding is needed on the effects that control the two processes. The alloy preparation method employed in this work allows the coverages of the gold in the alloy to be varied between 0 to 1.0 ML, with controlled formation of any Au/Pd alloy composition within this range. This potentially allows for the unification of the Ertl group's work on bare palladium (θAu = 0 ML) with the Fukutani group's work using alloys with intermediate coverages (θAu = 0.3-0.5 ML) to the Sykes group's work at very low Pd coverages (θAu $\geq$ 0.95 ML). For the present work, the relatively high (0.56-0.87 ML) gold-coverage alloys are investigated for hydrogen adsorption in an attempt rationalize the differences between the results for alloys with different compositions.

8.2 Experimental Methods

All experiments were carried out in a UHV chamber with a base pressure of 2.0×10^{-10} Torr. The palladium single crystal was cleaned between experiments by cycles of Argon bombardment (2.0 keV, 2-3 μA) for 10 minutes, followed by annealing to 1100 K in vacuo to

140

reform the (100) surface. Bombardment was followed by cleaning in oxygen, where the palladium crystal was successively heated and cooled in a constant pressure (5.0×10^{-8} Torr) of oxygen. The sample cleanliness was measured by AES and oxygen TPD. The Au/Pd alloys were prepared using an in-situ gold evaporation source described elsewhere [14]. Briefly, a Pd(100) single crystal was dosed with 5 ML of gold and annealed to various temperatures to segregate gold into the bulk of the Pd crystal, thereby forming well-defined, reproducible alloy surfaces where the composition and distribution of gold and palladium at the surfaces has been characterized previously [15, 16]. The Au/Pd samples could be cooled via liquid nitrogen to ~100 K and resistively heated to 1100 K.

TPD measurements were carried out with a heating rate of 5 K/s while monitoring up to five masses with a Dichor quadrupole mass spectrometer. High-purity Hydrogen (99.9999%) and CO (99.9%) were introduced into the UHV chamber via variable leak valves, and monitored for cleanliness using the mass spectrometer.

8.3 Results

8.3.1 Hydrogen Adsorption as a Function of Dosing Temperature

To explore adsorption behavior, different alloys with different gold surface coverages were dosed with various coverages of hydrogen. While the Ertl group found that two subsurface sites fill simultaneously (α_1 and α_2) [3], it has been found previously that the adsorption of hydrogen into the higher temperature, subsurface state (α_2) (where hydrogen desorbs from 230-240 K) is facilitated by holding the crystal at ~180 K while dosing hydrogen to allow for sufficient time for the hydrogen to diffuse and accumulate in, the subsurface region [13]. As a

141

consequence, hydrogen uptake on various alloys dosed at 120 and 180 K were studied, where the results are displayed in Figs. 8.3.1.1 and 8.3.1.2.

While dosing hydrogen at both temperatures clearly produces a broad hydrogen (2amu) desorption feature (~290-320 K) that has previously been identified as a chemisorbed, surface species [2], distinct low-temperature features are also observed that depend on the dosing temperature. In Fig. 8.3.1.1, for all alloys studied, a desorption state due to surface hydrogen is present at low doses centered at ~290 K. Even at low exposures, and increasingly evident with higher exposures, a desorption peak centered at ~230-240 K grows, and ultimately dominates the TPD spectra. This low temperature-peak does not appear to be dependent on alloy coverage as the integrated areas of the desorption peaks for various alloys dosed with 20 L hydrogen do not vary with gold coverage (graph not shown).
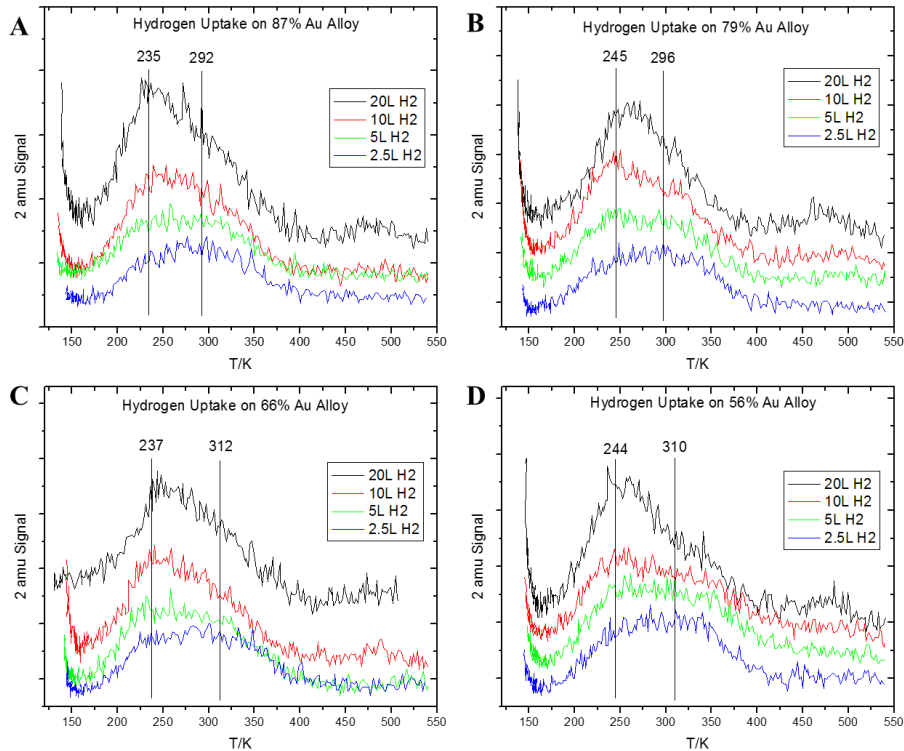
Figure 8.3.1.1: TPD spectra after various hydrogen doses with the sample held at 180 K on Au/Pd alloys with surface gold coverages of 87% (A), 79% (B), 66% (C), and 56% (D).

142

For the alloys exposed to hydrogen at ~120 K (Fig. 8.3.1.2), a sharp, low-temperature desorption peak centered at ~165 K is observed for all alloy compositions investigated. The temperature of this desorption state does not vary with increasing hydrogen exposure. Unlike the ~240 K subsurface hydrogen state, the ~165 K state depends on alloy coverage with the amount of hydrogen desorbing increasing with increasing palladium coverage. As mentioned above, at a lower dosing temperature hydrogen diffusion into the high-temperature subsurface state is slowed, but as evident in each of the desorption profiles as a function of hydrogen exposure in Fig. 8.3.1.2, some adsorption in this state does occur.
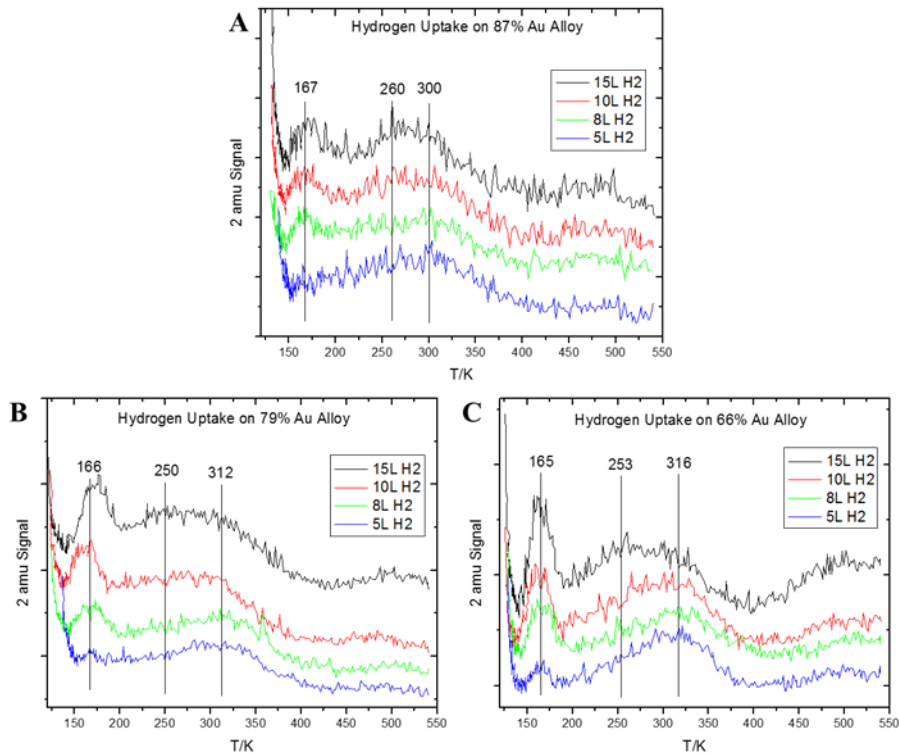
Figure 8.3.1.2: TPD spectra after various hydrogen doses with the sample held at 120 K on Au/Pd alloys with surface gold coverages of 87% (A), 79% (B), 66% (C), and 56% (D).

8.3.2 Hydrogen and Carbon Monoxide Coadsorption

143

To identify the influence of CO on various gold-palladium surfaces (either spillover or the "cork" effect), a range of alloy surfaces were exposed to 10 L of hydrogen both at 120 K and 180 K and subsequently exposed to 1 L of carbon monoxide. The TPD spectra collected at 2 and 28 amu from the same are shown in Figs. 8.3.2.1B,C and 8.3.2.2B,C respectively. For comparison, each alloy was dosed with 10 L of hydrogen and a TPD spectrum collected immediately prior to the hydrogen and CO coadsorption experiments. The resulting TPD spectra are displayed in Figs. 8.3.2.1A and 8.3.2.2A.
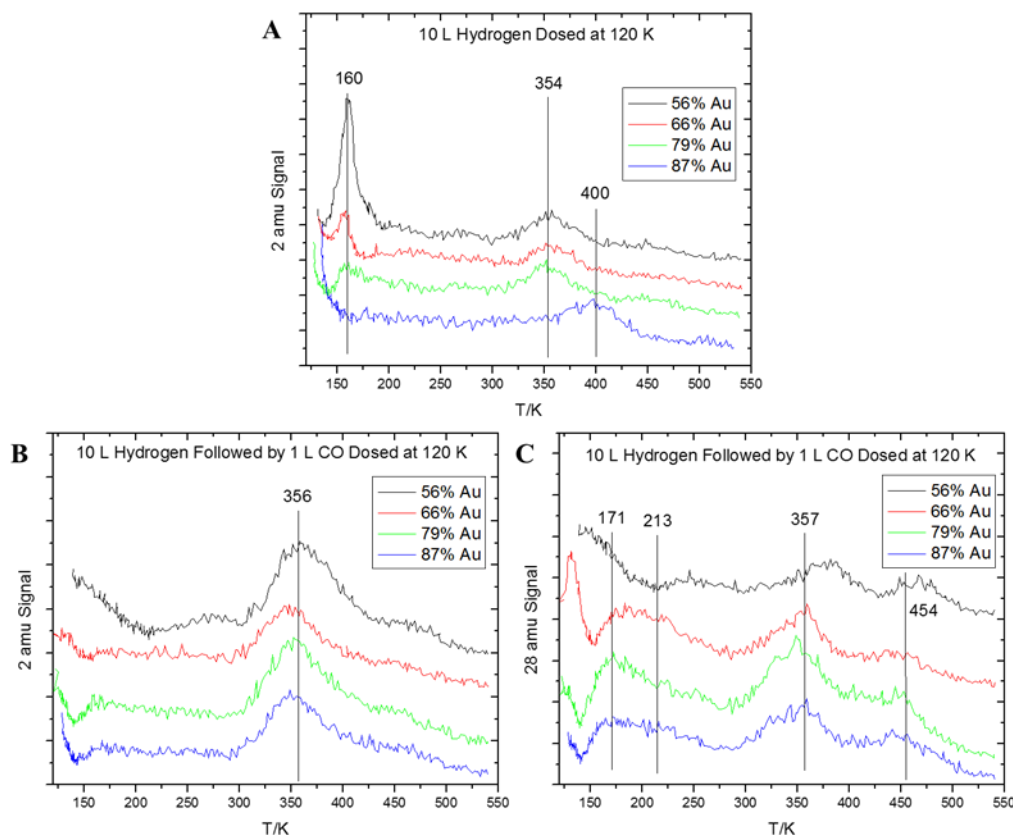
Figure 8.3.2.1: TPD spectra for alloy surfaces held at 120 K and dosed with 10 L hydrogen (2amu) (A), and 10 L hydrogen and 1 L CO (2 amu) (B) (28 amu) (C).

From the comparison of Figs. 8.3.2.1A and 8.3.2.1B it is immediately evident that the hydrogen desorption profiles have changed dramatically after the adsorption of additional CO. Only a single hydrogen desorption feature, centered at ~356 K is observed for all alloy

144

compositions after CO exposure with no observation of the ~160 K hydrogen desorption state. Coincident with the ~356 K hydrogen desorption peak is the presence of a carbon monoxide desorption peak in the same region (~357 K) (Fig. 8.3.2.1C). Even more important than the peak temperatures, the leading edge of both the CO desorption, and hydrogen desorption profiles coincide, even when peak desorption temperature differs.

When 1 L CO is dosed to alloy surfaces pre-covered by hydrogen at an elevated temperature (180 K), remarkably, nearly identical hydrogen-desorption spectra are collected (Fig. 8.3.2.2B). Again this high-temperature hydrogen desorption state coincides with CO desorption over a similar temperature range (Fig. 8.3.2.2C).
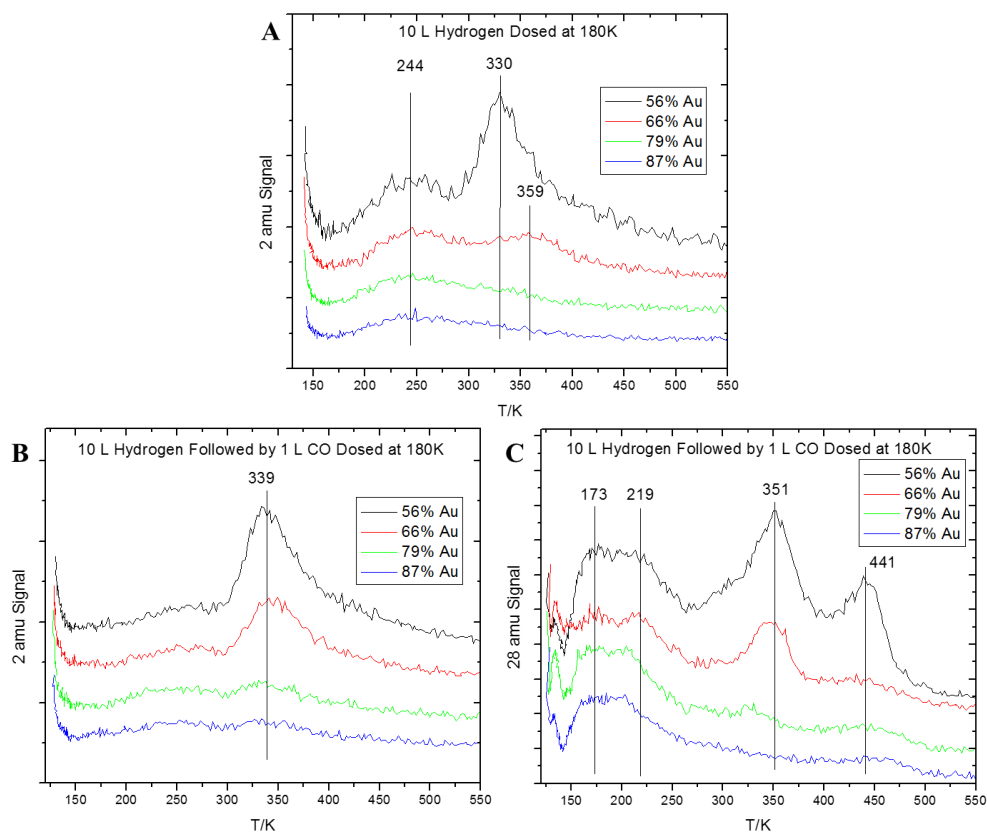
Figure 8.3.2.2: TPD spectra for alloy surfaces held at 180 K and dosed with 10 L hydrogen (2amu) (A), and 10 L hydrogen and 1 L CO (2 amu) (B) (28 amu) (C).

8.3.3 Carbon Monoxide Uptake on Au/Pd Alloys with Pre-adsorbed Hydrogen

To further explore hydrogen and carbon monoxide co-adsorption behavior, alloy surfaces pre-covered by hydrogen at higher temperature (~180 K) were exposed to varying amounts of carbon monoxide, and the corresponding TPD spectra are displayed in Fig. 8.3.3.1. The same increase of the hydrogen desorption peak to higher temperatures is observed, but interestingly, intermediate doses of CO (0.1 L) leads to desorption from both the low-temperature (~245 K) state and the CO-perturbed, high-temperature state (~340 K). This effect is most pronounced for the 79% and 66% gold alloy surfaces (Figs. 8.3.3.1B and 8.3.3.1C). Dual desorption states
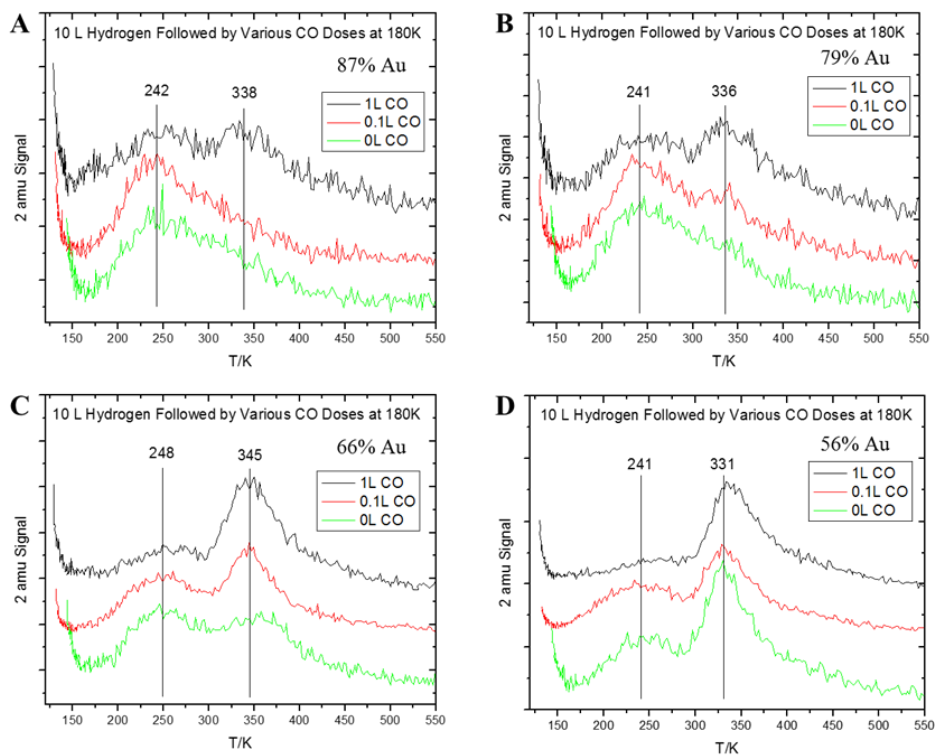
Figure8.3.3.1: TPD spectra of 10 L hydrogen and various CO doses on alloy surfaces dosed with gold coverages of 87% (A), 79% (B), 66% (C), and 56% (D).

suggests that this hydrogen species is not sufficiently mobile within the subsurface to diffuse to vacant Pd sites to allow it to desorb, resulting in both a subsurface, "capped" hydrogen desorption state and a subsurface hydrogen species that is still able to desorb at low temperatures.

8.4 Discussion

From previous work for hydrogen adsorbed on palladium surfaces, the hydrogen desorption profiles displayed in Fig. 8.3.1.1, where the sample was dosed with hydrogen at ~180 K to facilitate diffusion to a high-temperature, subsurface state (previously defined as an α_2) can be described and the adsorption sites can be identified. By comparison with work on bare Pd single crystal surfaces [2, 3], the high-temperature desorption state (with a peak temperature at ~300 K) is assigned to surface, chemisorbed hydrogen species. This is confirmed by the observation that it is the first adsorption state to be filled at low hydrogen exposures on all alloys studied. The low-temperature shoulder that begins to dominate the desorption spectrums at higher exposures is consistent with a high-temperature, subsurface hydrogen species also observed previously [2, 3], where the subsurface species was only present on the surface structured to have a (1×2) unit cell. It is noteworthy that, even at low hydrogen exposures (with a 2.5 L dose) surface restructuring and occupation of subsurface sites has already begun. Similar to the work by the Fukutani group [13], where the hydrogen desorption spectra seen on Au/Pd single crystal surfaces contained both surface and subsurface hydrogen desorption states. In the work presented here, the occupancy of the α_2 species does not appear to depend strongly on gold surface coverage in the Pd(100) alloy. This implies that this subsurface state, which is believed to be due to hydrogen deeper in the bulk of the sample than the low-temperature (α_1) peak [3], is

147

deep enough into the palladium sample to not be influenced by the gold accumulated near the surface.

By comparing the desorption spectra displayed in Fig. 8.3.1.2, where the hydrogen is dosed when the surface is held at ~120 K, to experimental work palladium single crystals [2, 3], the desorption sites to be identified. The sharp, low-temperature hydrogen desorption peak (~165 K) is occupied after the surface state (desorbing in a peak at ~310 K) is filled, and the surface (1×2) reconstruction is complete for all alloy surfaces studied, indicative of the low-temperature, so-called "near-subsurface" (α_1) species previously observed on clean Pd single crystals [2, 3]. With low-temperature (~120 K) hydrogen dosing the α_2 peak is still evident, but with a lower coverage of hydrogen evidenced by the smaller area under the desorption peak, in this state proposed to be due to reduced hydrogen diffusion. Interestingly, hydrogen adsorption on a Au/Pd single crystal showed no evidence of low-temperature peaks that would correspond to the α_1 species ([12] Figure 2).This may indicate that the composition of the subsurface alloy strongly influences the available hydrogen adsorption sites. In the case of the single crystal alloy, the subsurface gold concentrations are likely to be greater than the thin-film alloys used in this work, where 5 ML of gold are dosed to the surface and annealed to create different alloy surfaces by diffusion of gold into the bulk, inherently creating a gradient where gold concentration is largest near the surface and decreases as the distance into the subsurface increases. In contrast to the α_2 species, the α_1 species on this alloy surface is dependent on gold surface coverage, with more hydrogen adsorption occurring into this state with increasing palladium coverage.

When alloys dosed with hydrogen at both high- and low-temperature (Figs. 8.3.2.1 and 8.3.2.2) with 1 L CO, near identical hydrogen desorption spectra are observed (Figs. 8.3.2.1B

and 8.3.2.2B), where a single hydrogen-desorption profile is observed at ~340 K, slightly above the desorption of surface, chemisorbed hydrogen (~310 K) for all alloy compositions. This hydrogen desorption state is present at the same temperature, with no low-temperature peaks observed indicative of unobstructed hydrogen desorption from subsurface states (α_1 and α_2). It is important to note that the high-temperature (~356 K) peak does not appear to show any low-temperature shoulder, but appears to be symmetric with a slight high-temperature shoulder. This may indicate that the surface-bound hydrogen is also displaced to a less stable adsorption site by the CO.

An understanding of what happens to surface-bound hydrogen is important to understanding what will happen when hydrocarbons are exposed to the surface in hydrogenation reactions. The work by Sykes would suggest that hydrogen is displaced onto the gold surface, and would recombinitively desorb at very low temperatures (~110 K) from the gold surface [11]. No such peaks were observed, and measurements of the 2 amu desorption peak areas from both Figs. 8.3.2.1A, B and 8.3.2.2A, B are displayed in Fig. 8.4.1, and indicate that the displaced hydrogen must be included in the single, high-temperature, CO perturbed peak. The profile areas of the subsurface and surface hydrogen desorption profiles (Figs. 8.3.2.1 A and 8.3.2.2 A) correlate well with the areas of the hydrogen desorption profile consisting of a single CO-perturbed peak (8.3.2.1 B and 8.3.2.2 B) as evidenced by Fig. 8.4.1. Thus the high-temperature (CO perturbed) desorption state is comprised of hydrogen from both the subsurface and surface states. It appears that rather than spillover from palladium to gold sites as seen in the Sykes group's work, palladium bound hydrogen on these alloys is contained in some similar fashion to the subsurface species indicated by the apparent accounting for all hydrogen species in the high-

149
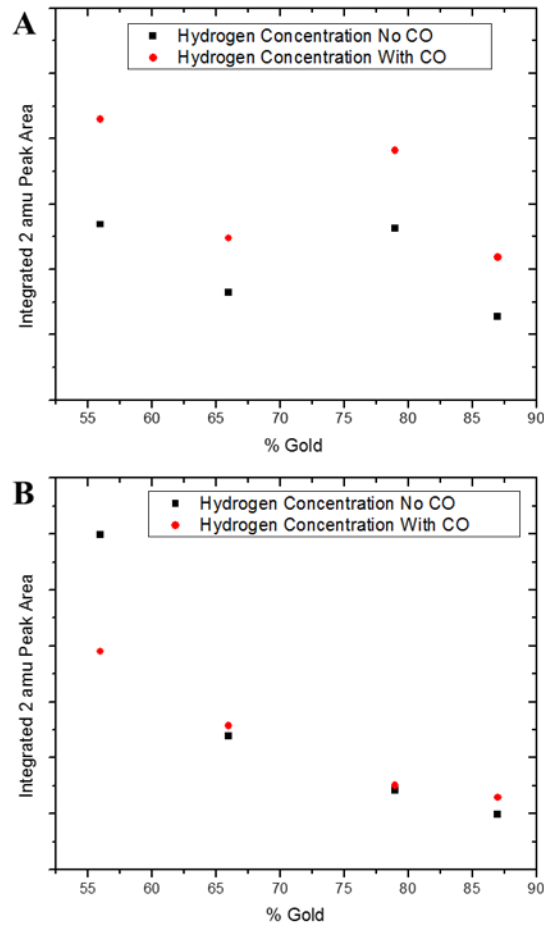
Figure 8.4.1: Integrated 2 amu peak areas from Figs. 8.3.2.1A, B
(A) and Figs. 8.3.2.2A, and B (B) as a function of gold coverage.

temperature, CO capped desorption state possibly due to very low concentrations of subsurface

palladium sites in their alloys.

The high-temperature hydrogen peak that is "capped" or "corked" by CO adsorption is

identical to that seen on the Au/Pd 30:70 single crystal, and that regime appears to translate to

higher gold coverages as well. As observed in Fig. 8.3.3.1, the capping of some fraction of the

palladium sites by low CO coverages gives rise to desorption profiles with two desorption states:

one typical of hydrogen desorption at low temperatures corresponding to the the α_2, subsurface

state, and the other, hydrogen desorption at higher temperatures coinciding with CO capped

adsorption sites. This indicates that this subsurface species is not sufficiently mobile to diffuse

from sites blocked by CO to vacant surface palladium sites to then desorb. The origin of this effect is unclear, but subsurface diffusion may be inhibited by the presence of significant amounts of gold in the near-subsurface region of the alloy.

8.5 Conclusion

The present work when viewed with both the work on gold single-crystal dosed with small Pd coverages and with the work on Au/Pd alloy single-crystals forms a nearly complete set of bulk and surface gold concentration conditions that have a large effect on hydrogen adsorption behavior. The Sykes group's work on a gold single crystal inherently will not have an appreciable Pd concentration in the subsurface conducive to hydrogen diffusion into the subsurface, and as such, CO displaces the hydrogen onto gold surface sites, and no subsurface hydrogen species were reported. The Au/Pd alloy single crystal used by the Fukutani group has a relatively consistent bulk Au/Pd concentration that appears enriched enough with Pd (~70%) to allow for subsurface absorption of the α_2 subsurface hydrogen state, but the subsurface concentration of Au (~30%) appears to inhibit the absorption of the low-temperature, α_1, subsurface species. The work described here allows for a wide range of controllable alloy coverages, but the deposition and formation of the alloys by this method dictate that the bulk of the crystal is Pd(100) with a gradient of gold concentration near the surface. The observation of all hydrogen peaks seen on the bare palladium surface with these alloys reinforces this argument. The alloys presented here allow for the bulk hydrogen properties of palladium with surface Au/Pd alloys conducive to selective hydrogenation reactions in which distinct hydrogen species can be investigated for their role and reactivity.

151

8.6 References

[1] O. Beeck, Hydrogenation Catalysts, Disc. of the Frad. Soc., (1950) 118-128.

[2] M.G. Cattania, V. Penka, R.J. Behm, K. Christmann, G. Ertl, Interaction of Hydrogen with a Palladium (110) Surface, Surface Science, 126 (1982) 382-391.

[3] R.J. Behm, V. Penka, M.G. Cattania, K. Christmann, G. Ertl, Evidence for "subsurface" hydrogen on Pd(110): An intermediate between chemisorbed and dissolved species, J. Chem. Phys., 78 (1983) 7486-7490.

[4] M. Wilde, M. Matsumoto, K. Fukutani, T. Aruga, Depth-resolved analysis of subsurface hydrogen absorbed by Pd(100), Surface Science, 482-485 (2001) 346-352.

[5] H. Conrad, G. Ertl, E.E. Latta, Adsorption of Hydrogen on Palladiu Single Crystal Surfaces, Surface Science, 41 (1973) 435-446.

[6] D.P. woodruff, Alloy Surfaces and Surface Alloys., Elsevier, Amsterdam, 2002.

[7] R.I. Masel, Principles of Adsorption and Reaction on Solid Surfaces, WIley, New York, 1996.

[8] F. Gao, Y. Wang, D.W. Goodman, CO Oxidation over AuPd(100) from Ultrahigh Vacuum to Near-Atmospheric Pressures: The Critical Role of Contiguous Pd Atoms, Journal of the American Chemical Society, 131 (2009) 5734-5735.

[9] C.J. Baddeley, M. Tikhov, C. Hardacre, J.R. Lomas, R.M. Lambert, Ensemble Effects in the Coupling of Acetylene to Benzene on a Bimetallic Surface: A Study with Pd{111}/Au, J. Phys. Chem., 100 (1996) 2189-2194.

[10] B. Samanos, P. Boutry, R. Montarnal, The mechanism of vinyl acetate formation by gas-phase catalytic ethylene acetoxidation, Journal of Catalysis, 23 (1971) 19-30.

[11] F.R. Lucci, M.T. Darby, M.F.G. Mattera, C.J. Ivimey, A.J. Therrien, A. Michaelides, M. Stamatakis, E.C.H. Sykes, Controlling Hydrogen Activation, Spillover, and Desorption with Pd-Au Single-Atom Alloys, J. phys. Chem. Lett., 7 (2016) 480-485.

[12] S. Ogura, M. Okada, K. Fukutani, Near-Surface Accumulation of Hydrogen and CO Blocking Effects on a Pd-Au Alloy, J. Phys. Chem. C, 117 (2013) 9366-9371.

[13] S. Ohno, M. Wilde, K. Fukutani, Desorption Temperature Control of Palladium-Dissolved Hydrogen through Surface Structural Manipulaiton, J. Phys. Chem. C, 119 (2015) 11732-11738.

[14] W.J. Whytenberg, R.M. Lambert, A Long-Lived Aluminium Evaporation Source for Controlled, Reproducible Deposition of Clean Ultra-Thin Films under UHV Conditions, J. Vac. Sci. Technol. A, 10 (1992).

[15] M. Garvey, J.A. Boscoboinik, L. Burkholder, J. Walker, C. Plaisance, M. Neurock, W.T. Tysoe, The Structure of the Au/Pd(100) Alloy Surface, Journal of Physical Chemistry C, 116 (2011) 6.

[16] Z. Li, F. Gao, O. Furlong, W.T. Tysoe, Adsorption of carbon monoxide on Au/Pd(100) alloys in ultrahigh vacuum: Identification of adsorption sites, Surface Science, 604 (2010) 136-143.

Chapter 9

Conclusions

9.1 VAM Reaction Characterization

The bulk of the work presented in this dissertation is focused on the elucidation of the VAM reaction pathway and kinetics on Pd(100) and Au/Pd(100) alloy surfaces. This reaction, and the adsorption behavior of the reactants, was primarily studied with TPD and RAIRS measurements.

It was necessary to study ozone adsorption on high-gold-coverage alloys because molecular oxygen dissociation is prohibited by the lack of necessary contiguous palladium sites required for oxygen dissociation [1]. Complex desorption spectra were collected via TPD consisting of broad 32 amu desorption peaks consisting of oxygen desorption from numerous sites for alloys with gold coverages less than 1.0 ML. To understand the contributions from each possible oxygen desorption state, DFT calculations were performed that provide an estimate of the desorption activation energy of oxygen atoms adsorbed in each unique four-fold binding site on the Au/Pd(100) alloy surface. Using previous Monte Carlo simulations [2] that provide the distribution of distinct four-fold hollow sites on the alloy surface with each individual desorption activation energy calculated from DFT, Monte Carlo TPD simulations were performed that give a reasonable fit to the TPD data observed with the exception of the 0.87 ML gold coverage alloy where the model TPD simulations fail to accurately predict the desorption spectra. It is

154

suggested that the discrepancy at this gold coverage, especially with high ozone exposures, could be attributed to the behavior of ozone dosed to gold seen previously, where, at high exposures, gold clusters were extracted from the surface [3]. It is tentatively proposed that ozone exposure on the 0.87 ML alloys (and the 0.79 ML alloys at high exposures) enriches the surface with gold such that more desorption from *f0*, four-fold hollow sites with exclusively gold atoms, occurs than predicted by the alloy site distribution alone, as seen in the TPD spectra.

Subsequently, ethylene adsorption on Au/Pd(100) alloys was studied to investigate di-σ and vinyl species formed on the surface. The ethylene adsorption energy increases sharply on surfaces with low palladium coverages (from 0 to 0.35 ML), and the heat of adsorption changes more slowly at higher palladium coverages. Corresponding to the increase in heat of adsorption is an increase in the σ-π parameter where, at low palladium coverages more π-like ethylene bonding occurs on the predominant isolated palladium sites available. At higher gold coverages the bonding becomes more di-σ-like as palladium dimer sites appear leading to more strongly bound ethylene species. Vinyl species were observed on alloys with gold coverages below 0.2 ML, potentially allowing for direct coupling to acetate species via the Moiseev pathway, but the disappearance of this species at low temperatures suggests that the vinyl species is not stable enough to react to form VAM. This work indicates that the VAM reaction likely proceeds via the Samanos pathway through the coupling of a di-σ ethylene species with an acetate species with a subsequent dehydrogenation to form VAM.

After investigating ethylene and oxygen adsorption on the Au/Pd(100) alloys, along with previous work characterizing acetic acid adsorption on Au/Pd(100) surfaces [4], the controlled study of the VAM formation reaction on Pd(100) and Au/Pd(100) was investigated.

155

On oxygen-covered Pd(100), the acetate removal kinetics were described and only decomposition products were observed for the reaction of ethylene with acetate species at all temperature ranges studied. Using fully deuterated ethylene, the acetoxyethyl intermediate (VAMH) was observed at low temperatures, confirming that the Samanos pathway was also the dominant pathway for the VAM reaction on Pd(100). Surface coverage effects were found to have pronounced influence on the reaction compared to the VAM formation pathway found on Pd(111). First, the saturation coverage of acetate is about half of that seen on Pd(111), leading to a more open surface that can accommodate more ethylene adsorption in the initial stages of the reaction. Second, the lack of ethylidyne accumulation on the Pd(100) surface results in a much more open surface leading to decomposition of VAM or VAMH, in contrast to the behavior on Pd(111) where ethylidyne blocking on Pd(111) stabilized VAM and prevented its decomposition. Finally, as decomposition products accumulated on the surface, carbon monoxide began to form. Accumulation of CO was found to block ethylene adsorption, and the kinetic data could not be fit well without including this CO blocking effect. As a result of these blocking effects, the selectivity on the Pd(100) surface was poor. Investigation of the nature of the decomposition intermediate suggests the possibility of a vinyloxy species resulting from VAMH decomposition.

Using the kinetic model developed on the Pd(100) surface, the VAM formation on Au/Pd(100) alloys were similarly investigated. Further proof of the CO blocking effect was evident for the VAM formation reaction with increasing gold coverages on the alloys chosen. As the gold coverage on the alloy surfaces increased, the amount of CO that was formed decreased, and correspondingly, the VAM formation rate increased until the gold coverage reached ~0.5 ML. Beyond coverages of 0.5 ML of gold in the alloy, the reaction was completely inhibited even under extreme conditions (~2 Torr ethylene exposure). An unreactive, unidentate acetate

156

species was identified on these surfaces, and it is proposed that with a single oxygen bonding to a single palladium atom precludes ethylene insertion and subsequent β-hydride elimination. Increased selectivity and activity were observed on Au/Pd(100) alloys with gold coverages below 0.5 ML.

9.2 Other Work

Beyond the VAM work, CO oxidation on a Au(111) surface was studied using ozone as the atomic oxygen source. CO oxidation occurred at temperatures as low as ~140 K, and two CO adsorption states were observed. On the clean Au(111), CO adsorption was identified on Au^0 sites via RAIRS measurements, but after ozone exposure, another distinct desorption state was observed corresponding to adsorption on $Au^{\delta+}$ sites indicating, as described previously, that gold-oxide-like domains can be formed from ozone exposure [3, 5]. No intermediates were observed in the oxidation reaction such as carbonate species.

Preliminary work on the adsorption of hydrogen on high gold coverage (>0.5 ML) Au/Pd(100) alloys was explored in an attempt to reconcile previous work [6, 7] on different Au/Pd alloy samples. The hydrogen adsorption behavior in this work was similar to that reported for bare palladium single crystals [8, 9], where two subsurface states were observed along with chemisorbed hydrogen species. The concentration of gold in the subsurface and bulk regions appears to be the origin of differing adsorption behavior between Au/Pd alloy surfaces previously studied. The alloys described in this work have a comparatively low subsurface and bulk gold concentrations than other alloy work (100% gold bulk concentration [6] and 30% [7] gold bulk concentration), thus explaining why the desorption behavior on the alloys presented in this work compares well with bare palladium single crystals. When hydrogen-saturated surfaces

157

were exposed to CO, a "cork" effect was observed where the isolated palladium sites were capped, and hydrogen was found to be unable to desorb until CO had desorbed, and unblocking of palladium sites, occurred. Interestingly, both subsurface hydrogen species and surface chemisorbed hydrogen species appear to all desorb at the same, CO-perturbed, desorption temperature following carbon monoxide capping. This work potentially allows for the study of hydrogenation reactions using chemically distinct hydrogens, as well as hydrogen storage applications.

9.3 References

[1] N. Saliba, D.H. Parker, B.E. Koel, Adsorption of oxygen on Au(111) by exposure to ozone, Surface Science, 410 (1998) 270-282.

[2] M. Garvey, J.A. Boscoboinik, L. Burkholder, J. Walker, C. Plaisance, M. Neurock, W.T. Tysoe, The Structure of the Au/Pd(100) Alloy Surface, Journal of Physical Chemistry C, 116 (2011) 6.

[3] B.K. Min, X. Deng, D. Pinnaduwage, R. Schalck, C.M. Friend, Oxygen-induced restructuring with release of gold atoms from Au(111), Phys. Rev. B, 72 (2005) 121410-121411-121410-121414.

[4] Z. Li, W.T. Tysoe, The adsorption of acetic acid on clean and oxygen-covered Au/Pd(100) alloy surfaces, Surface Science, 606 (2012) 1934-1941.

[5] T.A. Baker, B. Xu, X. Liu, E. Kaxiras, C.M. Friend, Nature of Oxidation of the Au(111) Surface: Experimental and Theoretical Investigation, J. Phys. Chem. C Lett., 113 (2009) 16561-16564.

[6] F.R. Lucci, M.T. Darby, M.F.G. Mattera, C.J. Ivimey, A.J. Therrien, A. Michaelides, M. Stamatakis, E.C.H. Sykes, Controlling Hydrogen Activation, Spillover, and Desorption with Pd-Au Single-Atom Alloys, J. phys. Chem. Lett., 7 (2016) 480-485.

[7] S. Ogura, M. Okada, K. Fukutani, Near-Surface Accumulation of Hydrogen and CO Blocking Effects on a Pd-Au Alloy, J. Phys. Chem. C, 117 (2013) 9366-9371.

[8] M.G. Cattania, V. Penka, R.J. Behm, K. Christmann, G. Ertl, Interaction of Hydrogen with a Palladium (110) Surface, Surface Science, 126 (1982) 382-391.

[9] R.J. Behm, V. Penka, M.G. Cattania, K. Christmann, G. Ertl, Evidence for "subsurface" hydrogen on Pd(110): An intermediate between chemisorbed and dissolved species, J. Chem. Phys., 78 (1983) 7486-7490.

CURRICULUM VITAE

Dissertation Title:

Investigation of Catalytic Oxidation and Coupling Reactions on Gold, Palladium, and

Gold-Palladium Alloys.

Full Name:

Theodore Douglas Thuening

Date and Place of Birth:

June 16th, 1990

Waconia, Minnesota U.S.A.

Education:

Ph.D., University of Wisconsin-Milwaukee, August 2017.

Major: Chemistry.

B.S., Concordia University, St. Paul, May 2012.

Major: Chemistry Minor: Mathematics.

Teaching Experience:

Chemical Science, University of Wisconsin-Milwaukee, 2012.

General Chemistry II, University of Wisconsin-Milwaukee, 2013, 2017.

Awards:

Paul W. Stor Chemistry Award, Concordia University, St. Paul, 2011.

MacFarland Graduate Research Award, University of Wisconsin-Milwaukee, 2015.

Presentations:

Oral Presenter, 63rd International AVS Symposium and Exhibition, Nashville, TN, 2016.
"Vinyl Acetate Formation Pathways and Selectivity on Model Metal Catalyst Surfaces."
Poster Presenter, AVS Prairie Chapter Regional Meeting, Chicago, IL, 2016. "Vinyl
Acetate Synthesis Over Pd(111) and Pd(100): Role of Ethylene and Ethylidyne
Formation."
Poster Presenter, AVS Prairie Chapter Regional Meeting, Notre Dame, IN, 2015. "Vinyl
Acetate Synthesis Over Pd(100) and Au/Pd(100) Alloy Catalysts."

Publications:

Thuening, T.; Walker, J.; Adams, H.; Furlong, O., Tysoe, W. Kinetics of low-temperature CO
oxidation on Au(111). *Surface Science*. **2016**, *648*, 236-241.

Li, Z.; Thuening, T.; Tysoe, W. The adsorption of ethylene on Au/Pd(100) alloy surfaces.
Surface Science. **2016**, *646*, 65-71.

Thuening, T.; Tysoe, W. Kinetics and Mechanism of Vinyl Acetate Monomer Synthesis on
Pd(100) Model Catalysts. *Catalysis Letters.* **2017**.

Thuening, T.; Tysoe, W.T. Vinyl Acetate Formation on Au/Pd(100) Alloy Surfaces. *Submitted
for publication: Catalysis Letters.*

المنارة للاستشارات

www.manaraa.com

Thuening, T.; Garvey, M.; Boscoboinik, A.; Tysoe, W.T. Adsorption Sites and Binding of

Oxygen on Au/Pd(100) Alloys with High Gold Coverages. *In preparation*.